Arabian Journal of Chemistry (2022) 15, 104070

King Saud University

Arabian Journal of Chemistry

www.ksu.edu.sa
www.sciencedirect.com

REVIEW ARTICLE

Nanostructured materials based on g-C_3N_4 for enhanced photocatalytic activity and potentials application: A review

Muhammad Sohail [a], Usama Anwar [b], T.A. Taha [c,d], H.I.A. Qazi [e], Abdullah G. Al-Sehemi [f,g], Sami Ullah [f,g], Hamed Algarni [f,h], I.M. Ahmed [i], Mohammed A. Amin [j], Arkom Palamanit [k], Waseem Iqbal [l], Sarah Alharthi [j], W.I. Nawawi [m], Zeeshan Ajmal [n], Hamid Ali [o], Asif Hayat [p,*]

[a] *Yangtze Delta Region Institute (Huzhou), University of Electronic Science and Technology of China, Huzhou 313001, China*
[b] *Soochow Institute for Energy and Materials Innovations, College of Energy, Soochow University, Suzhou 215006, China*
[c] *Physics Department, College of Science, Jouf University, P.O. Box 2014, Sakaka, Saudi Arabia*
[d] *Physics and Engineering Mathematics Department, Faculty of Electronic Engineering, Menoufia University, Menouf 32952, Egypt*
[e] *College of Optoelectronic Engineering, Chongqing University of Posts and Telecommunications, Chongqing 400065, China*
[f] *Research Center for Advanced Materials Science (RCAMS), King Khalid University, P.O. Box 9004, Abha 61413, Saudi Arabia*
[g] *Department of Chemistry, College of Science, King Khalid University, P.O. Box 9004, Abha 61413, Saudi Arabia*
[h] *Department of Physics, Faculty of Science, King Khalid University, P.O. Box 9004, Abha, Saudi Arabia*
[i] *Chemistry Department, College of Science, Jouf University, P.O. Box 2014, Sakaka, Saudi Arabia*
[j] *Department of Chemistry, College of Science, Taif University, P.O. Box 11099, Taif 21944, Saudi Arabia*
[k] *Energy Technology Program, Department of Specialized Engineering, Faculty of Engineering, Prince of Songkla University, 15 Karnjanavanich Rd., Hat Yai, Songkhla 90110, Thailand*
[l] *Dipartimento di Chimica e Tecnologie Chimiche, Università della Calabria, 87036 Cosenza, Italy*
[m] *Faculty of Applied Sciences, Universiti Teknologi MARA, Cawangan Perlis, 02600 Arau Perlis, Malaysia*
[n] *School of Chemistry and Chemical Engineering, Northwestern Polytechnical University, Xian 710072, China*
[o] *Multiscale Computational Materials Facility, Key Laboratory of Eco-Materials Advanced Technology, College of Materials Science and Engineering, Fuzhou University, Fuzhou 350100, China*
[p] *State Key Laboratory of Photocatalysis on Energy and Environment, College of Chemistry, Fuzhou University, Fuzhou 350116, China*

Received 16 January 2022; accepted 21 June 2022
Available online 2 July 2022

* Corresponding author.
E-mail address: asifncp11@yahoo.com (A. Hayat).
Peer review under responsibility of King Saud University.

Production and hosting by Elsevier

https://doi.org/10.1016/j.arabjc.2022.104070

KEYWORDS

g-C_3N_4;
Photocatalytic water splitting;
Photocatalytic CO_2 reduction;
Various dimensions;
Physiochemical properties

Abstract Semiconductor-based photocatalytic technology is regarded as an efficient pathway for resolving the energy scarcity across the globe. In this regard, graphitic carbon nitride (g-C_3N_4)-based materials could be alternatively employed in photochemical applications such as photovoltaic energy generation via CO_2 photoreduction and water splitting, along with natural resource purification via organic/inorganic pollutant degradation. Indeed, this kind of assertion has been made by considering the intrinsic physicochemical properties of g-C_3N_4 nanomaterials, owing to their increased surface area, quantum yield, surface charge isolation, distribution, and ease of modification through material configuration or incorporation of preferred interfacial capabilities. This review article has been designed to provide the most up-to-date information regarding the further assessment of the important advancements in fabrication along with photochemical applications of various g-C_3N_4 nanomaterials, while specifically focusing on the scientific reason behind its success in each assessment. The discovery of interventions to alleviate such restrictions and boost photocatalytic performance has gained substantial interest. Following photo-excitation fundamentals, this work explains two distinct photoexcitation mechanisms, the carrier and charge transfer techniques, wherein the significant exciting state impact of g-C_3N_4 has still not been widely focused on in past studies. In this regards, we cautiously introduce the updated advances and associated functions of the alteration techniques, including morphological features, elemental dopants, deficiency engineering, and heterojunction implemented in photocatalytic performance, which are equated from the carrier and charge transport perceptions. The future perspectives in designing and properly tuning the highly active hierarchical or copolymer g-C_3N_4 nanoparticles in a photocatalytic system, which may improve the renewable energy cultivation and reduction efficiency are critically deciphered in detail and outlined thoroughly.

1. Introduction

1.1. Background

The utilization of clean and renewable energy is critical for fulfilling the growing global energy demands and resolving the fiscal energy problems caused by excessive consumption of fossil fuels (Child, 2018; Wang, 2018; Wei, 2018; Sohail, 2017; Sohail, 2018; Qadeer, 2020; Wageh, 2021; Wageh, 2021). With the development of science and technology, solar energy is an inexhaustible source of renewable energy on the earth, and has the extensive potential to overcome all of these limitations precincts (Faunce, et al., 2013; Mills et al., 1993; Qadeer, 2022; Hao, 2018; Wageh and Zhao, 2019; Swelm, 2018; Wageh, 2018; Wageh et al., 2016; Wageh, 2016) and its further use for the attended scientific consensus, since Honda and Fujishima used semiconductor based materials for water splitting in 1972 (Fujishima and Honda, 1972; Inoue, 1979). One such discovery, sparked an extensive research interest into the titanium dioxide (TiO_2) based photocatalysts, which are being widely used for the efficient photocatalytic CO_2 reduction, water splitting, pollutants degradation, sensors, photoelectronics, photobacterial agents, etc. under solar light irridiation (Yi, 2014; Gaya and Abdullah, 2008; Naciri, 2022; Naciri, 2020; Naciri, 2021; Huang, 2021; Zhang, 2016; Wageh, 2015; Wageh, 2014). Nonetheless, the efficient photocatalytic utilization of visible light (key constituent of photovoltaic irradiance as it produces the Earth texture) in order to accelerate the oxidation process, which is still a challenging task for scientists (Asahi, 2001; Kumar and Devi, 2011; Naciri, 2020; Qadeer, 2019), due to huge difficulty of identifying the compounds with narrow band gaps, an enhanced electronic structure, sufficient electron transfer mobility, and low level of replication, along with excellent consistency. Various materials have been used in multiple research fields (Ajmal, 2020; Ahmed, 2021; Hsini, 2021; Hsini, 2020; Hou, 2014; Hou, 2013; Wageh et al., 2013; Wageh et al., 2013; Wageh, 2013). Indeed, numerous outstanding studies on fabrication and modification of graphitic carbon nitride (g-C_3N_4)-based photocatalysts, as well as their uses in energy and ecological challenges, are already accessible. Only a few papers, however, have discussed on the varied features of g-C_3N_4-based photocatalyst rational design and its impact on the activity of the catalyst. As a result, it is relevant to provide a complete review of the current advancements in g-C_3N_4-based catalysts for photocatalysis and environmental remediation. We focus on the basics, diverse characteristics, design, and possible uses of g-C_3N_4 based photocatalysts in this review. We assume that this review will encourage the synthesis of state-of-the-art g-C_3N_4 based photocatalysts and designs that improve light utilization and photocatalytic performance, but will also assist with confronting the difficulties that g-C_3N_4-based photocatalysts face in manufacturing and storage of renewable and sustainable energy. The development of such unique photocatalysts will pave the way for their extensive use to complement the sustainable energy and the contaminant monitoring methods. The main postulates of our review are manifested in the fellowing graphical abstract as shown in Fig. 1.

1.2. Semiconductor photocatalysis

Heterogeneous photocatalysis accelerates the chemical reactions (oxidations and reductions) caused by the stimulation of a photocatalyst, that combines with metals, non-metals, and metal oxides to facilitate the optical absorptions with consecutive energy-conversion cultivator sources. Notably, the photocatalysis process is concerned with the considerable stimulation of reagents and derivatives by optical absorption and assessing the photocatalytic conversion. Additionally, the reaction process shows, that the photocatalyst assimilates the electrons rather than the sorbent (Rochkind, 2014; Pallavi, 2010; Ullah, 2016; Sohail, 2020; Wageh, 2007). The photoinduced charged particles basically stimulate the photoconversion of water and CO_2 into associated renewable compounds in a photocatalytic production known as "fossil energy" (Styring, 2012; Chen et al., 2015). Such chemical reactions are comparable to natural photosynthesis (in which chloroplasts assimilate natural light in plants to encourage carbohydrate and oxygen fabrica-

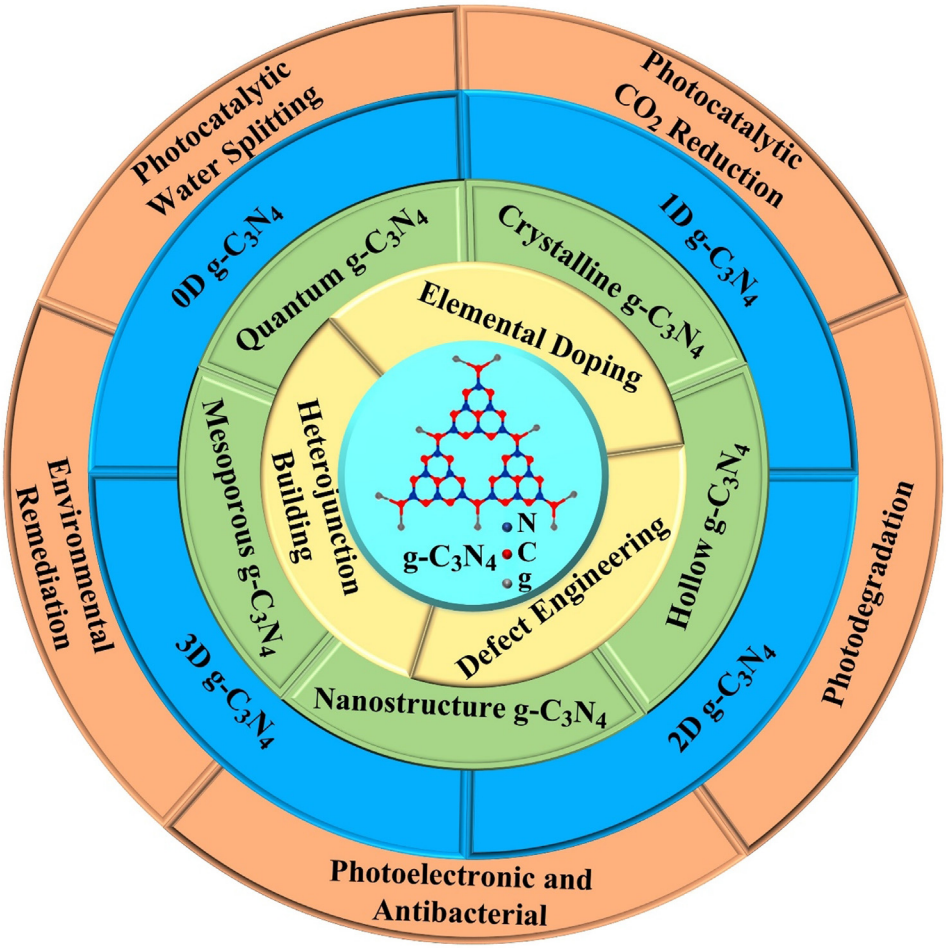

Fig. 1 Scheme exhibiting the applicability of g-C_3N_4-based nanomaterials in photocatalysis research and the accompanying methodologies for photocatalytic efficiency improvement.

tion from carbon dioxide and water) and are thus referred as artificial photosynthesis (Fig. 2). Moreover, the photoinduced electrons could also promote the total combustion (calcification) of environmental pollutants in marine ecosystems, either via a direct or indirect pathway, thereby, resulting into the formation of potential oxidizing agents such as a hydroxyl source (Nosaka and Nosaka, 2017; Wang and Domen, 2019).

1.3. Methodologies of photocatalysis

The photocatalysis process is initiated with the absorption of light from the ground state (valance band) toward the excited state (conduction band) (Step I) (Wageh, 2016). The subsequent clusters of electrons and holes could be thoroughly combined within or at the photocatalyst surface, with associated fuel released by luminescence or radiative activation of the crystalline structure (Step II). The charge recombination is critical, as it limits the photocatalytic performance for photoelectron absorption. Similarly, the photoinduced electrons/holes are deflected away from the material interface without charge recombination. Various photooxidation/reduction reactions with adsorbed species, including water, oxygen, and other organic or inorganic species (Steps III and IV) (Karamian and Sharifnia, 2016; White, 2015; Aleksandra, 2014), are presented in Fig. 3. These processes, which are essential for photocatalytic environmental remediation and solar fuel production, are ultimately limited by the reduction potential of photoexcited electrons in the conduction band (CB) and the oxidation potential of photogenerated holes in the valence band (VB). Therefore, the redox potential, band energies, and band gap of semiconductors (SC) play a significant role in determining the possibility and rate of charge transfer, which are considered to be the critical design parameters for selecting suitable photocatalysts (Sakata and Kawai, 1983; Zou, 2001; Qadeer, 2022). The semiconductor photocatalysis, whose fundamental configuration and surface-electronic structure differ between materials and applications, is an interfacial interaction between electrons and holes caused by band gap stimulation.

1.4. Photocatalytic materials

The use of titanium-based electrodes under UV irradiation for the overall water splitting (OWS) process has led to an extensive investigation for the evolution of H_2 energy (Park et al., 2006). TiO_2 powder was proven to be an effective catalyst for the photocatalytic decomposition of cyanide ions in water (Frank and Bard, 1977), and in the field of environmental purification. However, due to the wide band gap, recent research has focused on finding alternative semiconductors, which should provide better photocatalytic performance under solar (rather than UV) irradiation (Kubacka et al., 2016). According to the band gap of a semiconductor, a photocatalyst can be used in a variety of ways, including ZnO (Lee, 2016), Fe_2O_4 (Li, 2007), WO_3 (Wang, 2012), SrTiO3 (Kato and Kudo, 2001), $NaTaO_3$ (Yu et al., 2004), CdS (Jing and Guo, 2006), Ag_3PO4 (Wang, 2012), BiPO4 (Pan and Zhu, 2010), and g-C_3N_4 (Venkatathri and Kumar, 2017) (Fig. 4). Despite

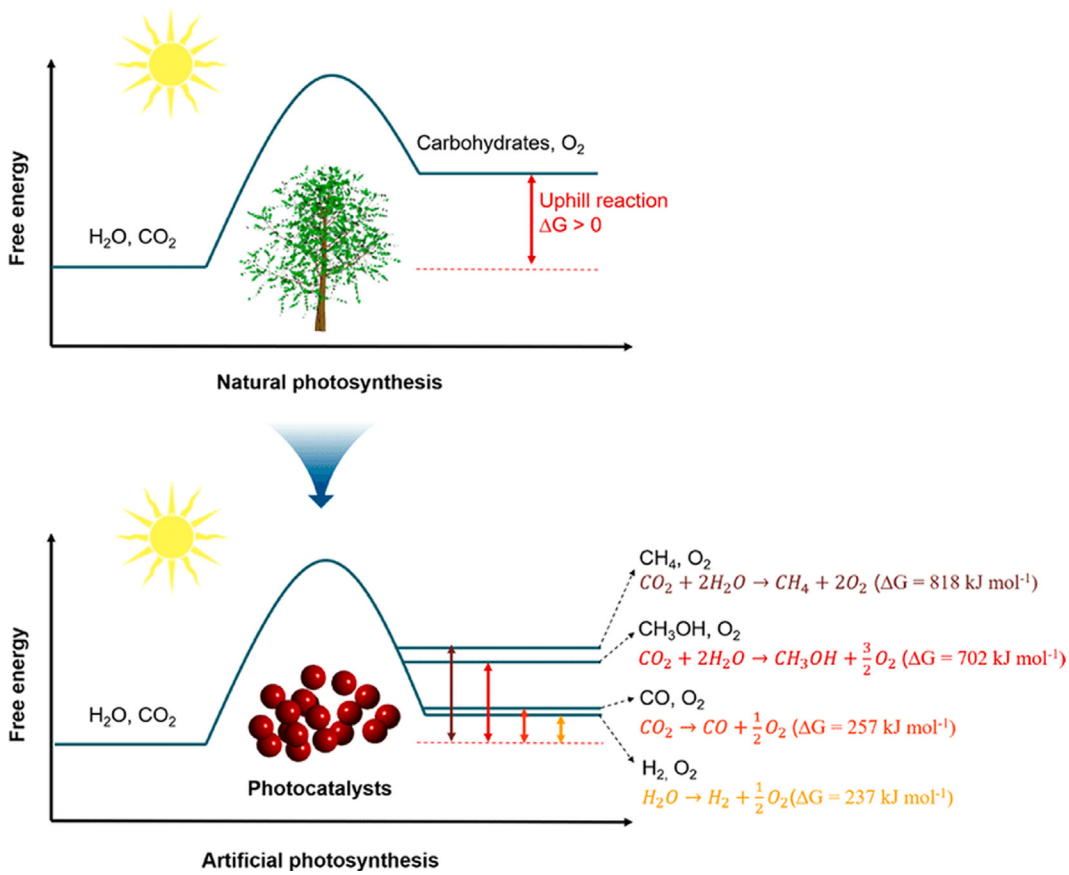

Fig. 2 (a) Natural and (b) artificial photosynthesis processes. Reprinted with permission from Wang and Domen (2019). Copyright © 2020, American Chemical Society.

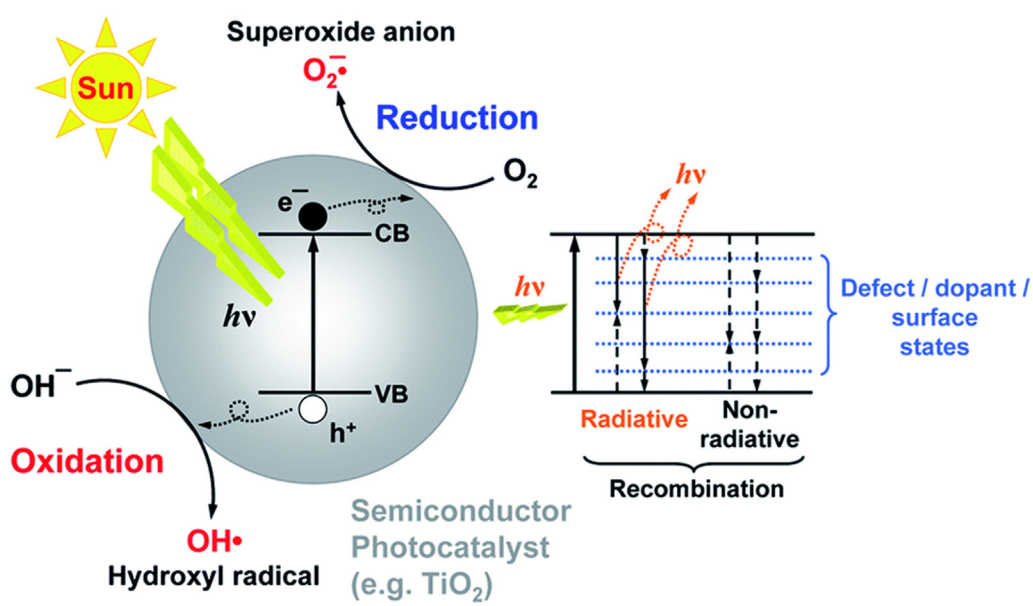

Fig. 3 Principal photophysical processes for semiconductors (SC) under light irradiation. Reprinted with permission from Aleksandra (2014). Copyright © 2014, Royal Society of Chemistry.

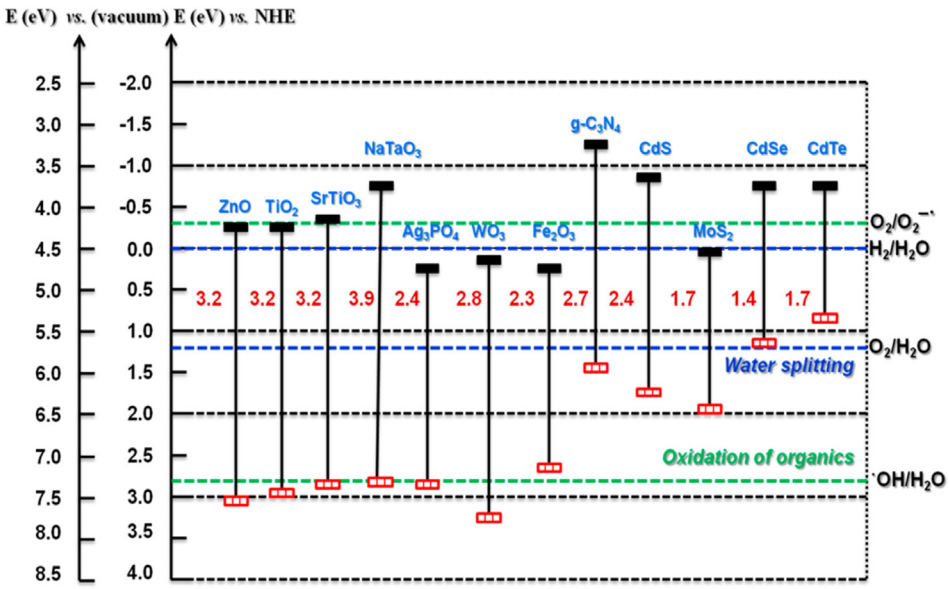

Fig. 4 Band gap energy and band edge energies of different semiconductors. Reprinted with permission from Venkatathri and Kumar (2017).

substantial literature on the subject, it is still difficult to use of photocatalysts in order to generate solar fuel or the decomposition of organic pollutants owing to poor light-harvesting or ineffective light energy conversion.

1.5. Graphitic carbon nitride (g-C_3N_4)

The use of visible light photocatalysis provides the best possible way to capture the maximal solar energy owing to the dominance of three sections of the electromagnetic spectrum, UV (5 %), visible light (45 %), and IR (50 %), as manifested in (Fig. 5) respectively, (Wu, 2011). Several photocatalysts, such as TiO_2 (3.0–3.2 eV), have broad band gaps and are, therefore, only active under UV irradiation (385 nm) (Yi, 2014).

There has been a rapid advancement in the number of scientific papers and patents (Kumar and Devi, 2011) dealing with photocatalytic OWS process, CO_2 reduction, and pollutants degradations

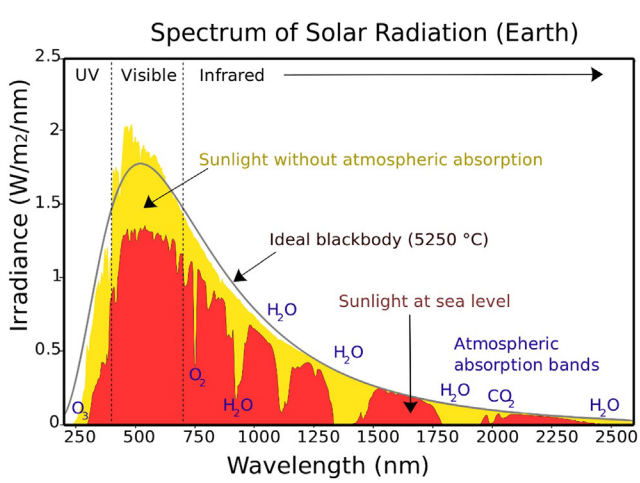

Fig. 5 Spectral irradiance of solar light. Reprinted with permission from Wu (2011). . Copyright © 2011, Elsevier

(Hernández-Alonso, 2009; Sohail, 2021; Hayat, 2022). Fig. 6a shows that g-C_3N_4 is a promising metal-free polymeric semiconductor with a low band gap (Fig. 6b) (Wang et al., 2009), which is ideal for visible light absorption and is versatile for large-scale application. Unlike many other organic semiconductors, the g-C_3N_4 has a high thermal and chemical resistance to oxidation, even at temperatures of 500 °C, which makes it an ideal material for photovoltaic applications. The synthesis of g-C_3N_4 and its derivatives for diverse applications has been extensively documented (Vhna, 2021; Santosh, 2013; Qadeer, 2022). The photocatalytic applications in environmental remediation and solar fuel generation, which emphasize emerging synthetic strategies in order to improve the photoactivity of g-C_3N_4 nanostructures by controlling their size, morphology, light absorption, charge separation, and ultimately their surface reactions are covered in this review. In addition, future research directions are also highlighted in this review.

1.5.1. g-C_3N_4 nanostructures: size and shape

There has been an increased interest in the application of nanoparticles, including electronics (Lewis and Nocera, 2006), catalysis (Rhind, 2009), biomedical (Faunce, 2013), sensing (Mills et al., 1993), and smart materials (Fujishima and Honda, 1972) throughout the science and engineering fields. The nanomaterials are distinct from their bulk precursors in some essential ways. It is due to their high surface-to-bulk atom ratio, as nanomaterials have a lower melting point and a higher solid–solid phase transition temperature. The electrical and optical properties of nanomaterials are greatly influenced by quantum confinement effects, which originate from the evolution of their band structure and the formation of atomistic-like behavior and several heterogeneous catalysts with strong size-dependencies due to quantum confinement (Inoue, 1979). For example, Gold (Fujishima et al., 2008; Ma, 2014) has a large surface area characterized by low coordination, and high energy sites exposed. Charge separation transfer from the photocatalyst surface to an adsorbed species may be accelerated, if these variables act synergistically (Gaya and Abdullah, 2008; Schneider, 2014; Habisreutinger et al., 2013; Qadeer, 2021). Mo et. al. investigated the effect of calcination factor onto the melamine-derived g-C_3N_4 crystalline lattice, morphological progression, and energy band construction (Mo et al., 2015). The XRD diffraction patterns revealed that g-C_3N_4 could be completely justified as the temperature was increased > 500 °C (Fig. 7a). Significantly, the

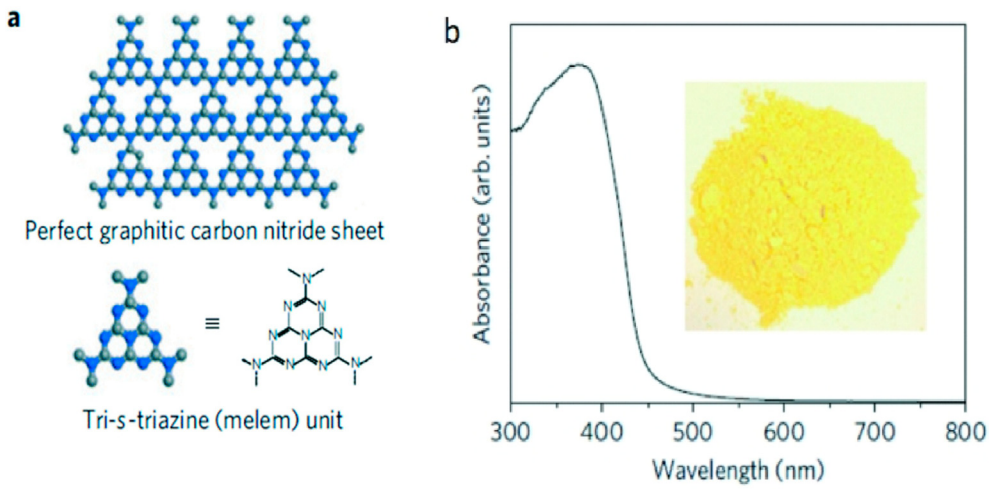

Fig. 6 (a) g-C_3N_4 structure comprising melem units, and (b) UV–vis diffuse reflectance (DRS) spectrum and image (inset) of g-C_3N4 (Wang et al., 2009).

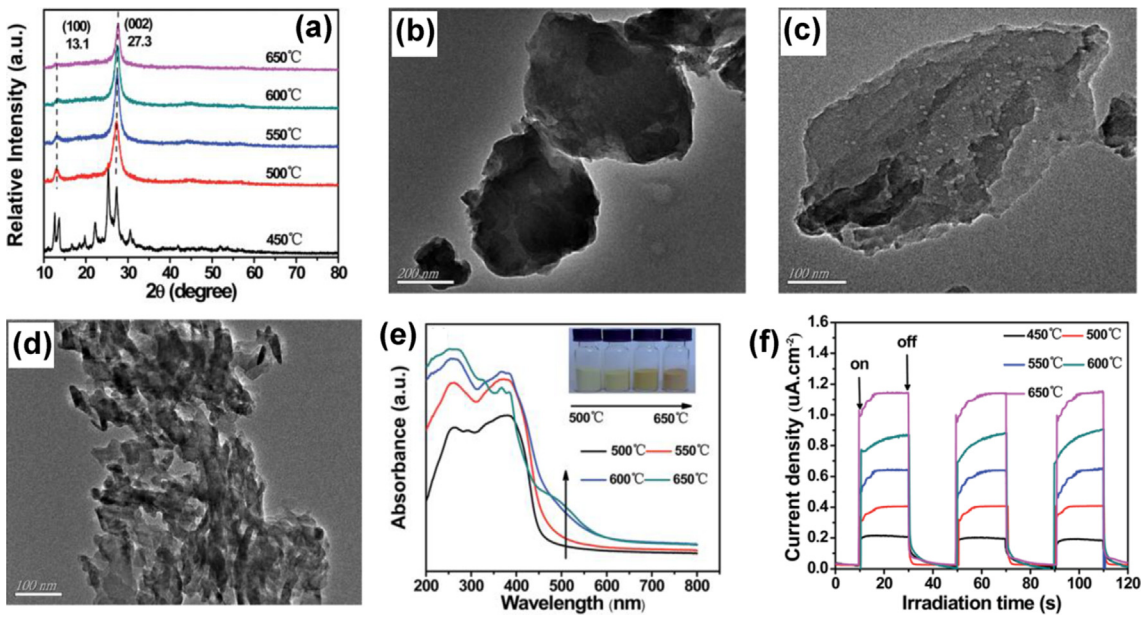

Fig. 7 (a) XRD patterns, TEM at (b) 550 °C, (c) 600 °C, and (d) 650 °C. (e) UV–vis DRS and (f) transitory current densities responses of g-C_3N_4 produced at various annealing temp. The color of the g-C_3N_4 photocatalysts produced at distinct temps is shown in the inset of (e). Reprinted with permission from Mo et al. (2015). Copyright © 2015, RSC Publishing.

peaks observed of the material synthesized at 450 °C differed from another sample, indicating that the melem analogues were present. At 600 and 650 °C, the framework of g-C_3N_4 grew extremely loose, shorter, and plump, with the formation of numerous holes on the g-C_3N_4 interface (Fig. 7b, d). Conversely, Fig. 7e shows a significant red-shift in the sharp absorption edges stretching from 470 to 570 nm, as well as a color transition from yellow to deep oranges (Fig. 7e), thereby, signifying the higher light absorption for materials with rising temperatures (Mo et al., 2015). The red shift was caused by an increase in the π-plane conjugated and increased in the degree of crystallinity. According to the transitory current density responses (Fig. 7f), the g-C_3N_4 produced at 650 °C had the maximum current density with excellent repeatability and consistency, thereby, making it more suitable for photocatalytic performance.

Despite, several efforts have been made in order to exfoliate the bulk g-C_3N_4 into sheets morphology, but yet there is still a challenging task for achieving a good yield, precise morphology, and ultrathin nanosheets, thereby, necessitating further research in this field (Ong et al., 2016). The g-C_3N_4 has transformed into nanosheets (three to two dimensional), which results in the transformation of various morphologies like nanorods/nanotubes (one dimensional) and quantum dots (zero-dimensional) aimed at industrial applications and energy harvesting (Ong et al., 2016). In this context, the g-C_3N_4 was obtained using a complicated, soft, and self-templating technique, and quantum dots were generated using a hydrothermal etching technique. From a salt-template assisted process, the honeycomb-structured g-C_3N_4 remained effectively organized (Ong et al., 2016; Naseri, 2017). Zhao et. al. proposed the current trends in merging 0D with 2D g-C_3N_4 to form 0D/2D composites with enhanced photocatalytic performance (Zhao, 2018). Wang et. al. (Wang, 2017) compared 2D/2D interface of g-C_3N_4 with other 2D nanomaterials. Unquestionably, heterojunctions such as type II, Schottky, and Z-schemes improve photo-driven

reactions by reducing the charge diffusion paths, and decreasing photogenerated charge recombination rates, along with increasing the surface area of the photocatalyst (Wang, 2018).

1.6. Elemental doping

In additional to the structural regulation outlined previously, elemental doping (both non-metal and metals) is another efficient approach of alteration (Khan, 2020; Raziq, 2020; Ullah, 2020; Shaishta, 2020; Rehman, et al., 2019; Khan, 2020; Hayat, 2019; Hayat, 2020; Hayat, 2019; Majeed, 2021; Rahman and Hayat, 2019; Hayat and Li, 2019; Hayat, 2019; Khan, 2019; Hayat, 2019; Hayat, 2019; Khan, 2018). By inserting heteroatoms, the Eg values of the compound materials may be modified to enhance the photo response range (Fig. 8a), and the resistance between the layers could be reduced to speed up the separation of charge, thereby enhancing the photocatalytic performance of g-C_3N_4 (Hasija, 2019; Liu et al., 2021; Hayat, 2022; Kongto, 2022; Alenad, 2022; Hayat, 2021; Hayat, 2021; Rehman, 2021). Fig. 8b depicts the proportions of distinct elemental doping (Hasija, 2019; Li, 2022). Notably, metal and nonmetal doping have markedly differing impacts on the corresponding photoexcitation processes.

1.6.1. Metal doping

Metal doping consists of precious metals/non-metals (such as alkali elements and transition elements) co-doping and single doping (Hayat, 2022; Pan, 2022; Taha et al., 2021; Sohail, 2021; Hayat,

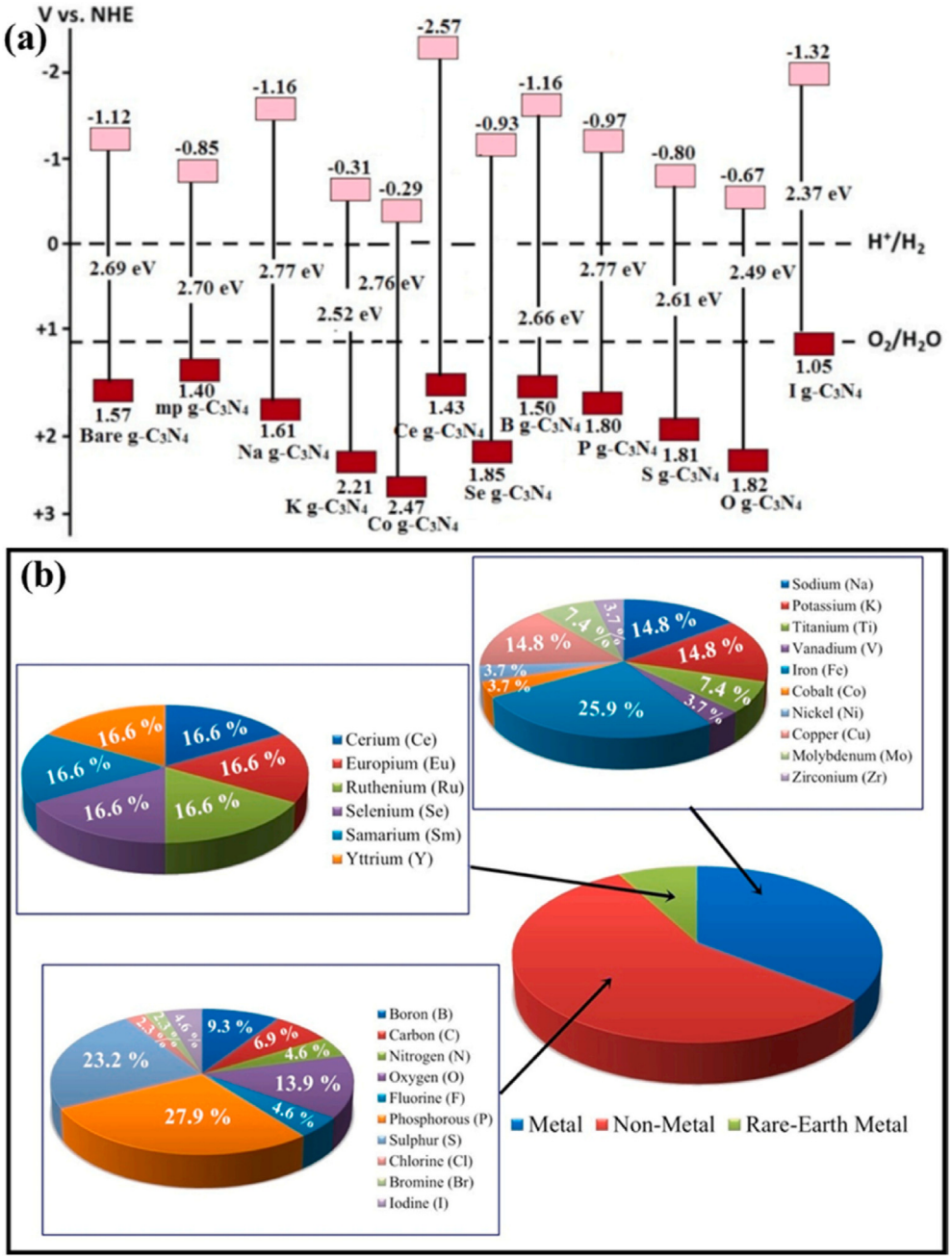

Fig. 8 (a) Band configurations for pristine and modified g-C_3N_4 and (b) a description of the ratios of several modified g-C_3N_4 photocatalysts. Reprinted with permission from Hasija (2019)). Copyright © 2019, Elsevier.

2022). In particular, metals could be incorporated within g-C_3N_4 framework by calcining or hydrothermally method of their main precursors. The doping positions of the dopants are determined by the size of the heteroatoms and their length from or within the substrate plane. For metal doping, orbital hybridization could happen among the g-C_3N_4 doped orbital and molecular orbital, producing additional energy levels to reduce the E_g value and increase the optical absorption. Furthermore, additional defective phases could be incorporated into electronic frameworks, resulting in greater active sites and a stronger e^-/h^+ separation and transport. Wang and coworker synthesized K-doped ultrathin porous g-C_3N_4 by hydrothermal crystallization for degradation of TC (Wang et al., 2018). X-ray photoelectron spectroscopy (XPS) measurements revealed that K has been effectively added into the g-C_3N_4 structure by creating K-N bonds (Fig. 9a). Furthermore, K-doped g-C_3N_4 demonstrated improved separation and transfer rates, that resulted in increased the photocatalytic activity. Moreover, porous design can supply additional active sites, that can reduce the charge recombination even more. As a result, K-doped g-C_3N_4 had the greatest degradation performance, which was roughly 2.88 times greater than pure g-C_3N_4. Yan et. al. studied the impact of Na, K, Ca and Mg doping on the morphology and photocatalytic activity of g-C_3N_4 (Yan et al., 2018). The metal doping discussed earlier caused by the modifications in the electronic structure of g-C_3N_4 (Fig. 9b), that were ascribed due to electrons supplied by metal to the nitrogen atom or those escaping from the surface of g-C_3N_4. Additionally, Na, Ca, Mg and K were introduced into g-C_3N_4 framework by creating cationic covalent bonds or by producing oxides with g-C_3N_4. This finally increased the degradation rate of TC. Metal doping impacts not just carrier mechanisms as well as the exciton behaviors of g-C_3N_4. For instance, Shu and coworkers inserted Na^+ as impurities into mesoporous g-C_3N_4 nanosheets (referred as Na-MCN) by calcining a solution of sodium chloride and dicyandiamide and examined the carriers and excitons within the resulting material. The lower fluorescence intensity of the above material suggested a lower charge recombination rate. In addition, the strong photocurrent response and low impedance circle size of Na-MCN validated the enhanced exciton dissolution and carrier transfer performance. The aforementioned findings were ascribed to the production of cyano groups in the fundamental g-C_3N_4 structure by sodium ion doping, the insertion of sodium sites, and morphological alteration inside and among the unit layers.

1.6.2. Non-metal doping

Despite metal doping could significantly enhance the efficiency of g-C_3N_4 by regulating its band gap, constraints its photo-corrosion, elevated the charge recombination but expensive cost were observed.

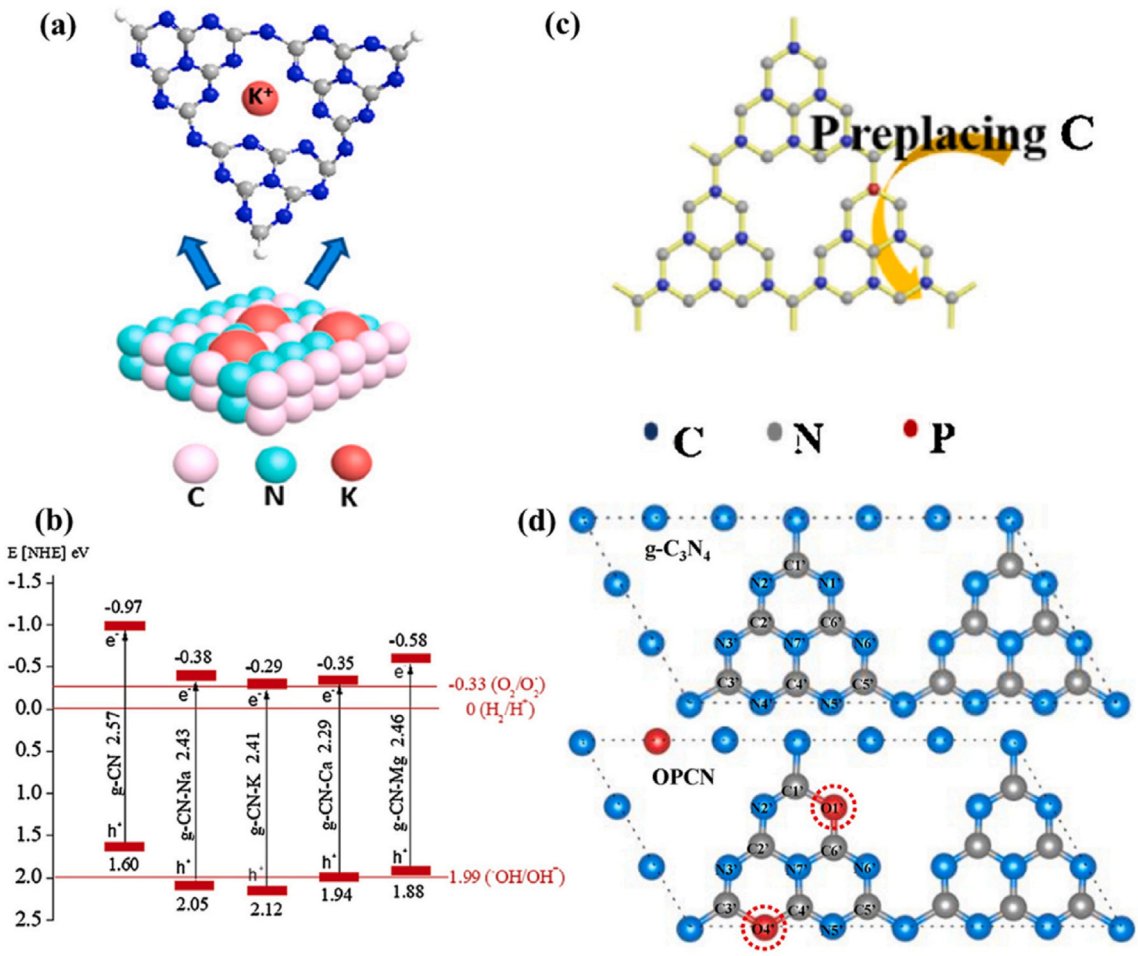

Fig. 9 (a) Illustration of modified K ions in the g-C_3N_4 layer. Reprinted with permission from Wang et al. (2018). ; (b) Band configuration of modified g-C_3N_4. Reprinted with permission from Zhang (2021). Copyright © 2021, Elsevier; (c) Proposed P loaded sites within the g-C_3N_4 skeleton. Reprinted with permission from Mao (2018). Copyright © 2019, Elsevier; (d) framework of pristine g-C_3N_4 and O/g-C_3N_4 after activation. Reprinted with permission from Yuejie (2019). Copyright © 2019, Elsevier. Copyright © 2018, American Chemical Society

Non-metallic atoms could be integrated within the skeleton of g-C_3N_4 by using thermal polymerization or the hydrothermal technique for precursors mixture. Due to their higher electronegativity and ionization potential, non-metallic atoms can readily form covalent bonds by gaining electrons (Nor, 2019; Hayat, 2022; Hayat, 2022; Hayat et al., 2022; Hayat, 2022; Hayat, 2022; Hayat, 2021; Hayat, 2021; Hayat, 2021). In comparison to metallic doping, non-metal doping could avoid the above drawbacks and achieve the identical results as of metal doping, while maintaining the non-metallic properties of g-C_3N_4. Furthermore, contrary to metallic doping, non-metal doping is mostly accomplished through interatomic displacement (i.e., C, H and N) (Li, 2009; Hamid, 2020; Raziq, 2020; Khan, 2021). This interatomic replacement could have a considerable effect on carbon and nitrogen hybridization, influencing the electrical and optical performances of doped g-C_3N_4 (Jh et al., 2020; Hayat, 2022; Ghufran, 2021). Zhou and coworkers developed a phosphorus (P) doped g-C_3N_4 by thermal copolymerization for degradation of RhB dye (Zhou, 2015). P was effectively doped into g-C_3N_4 structure by replacing two distinct carbon sites to generate P–N or P—N bonds, resulting in more defects and greater active sites. The addition of P can facilitate the separation of charges even more, leading to the formation of a P^+ center, that acts as a Lewis acid site. As a result, the Rhodamine B degradation efficiency of P-doped g-C_3N_4 enhanced 2.9-fold, when compared to pure g-C_3N_4. Despite this, Wu and coworkers discovered that P was exclusively doped into g-C_3N_4 skeleton via P-N bonds (Fig. 9c), and no P-N bond was identified (Mao, 2018). This meant that the exact doping location of P might alter based on the synthesis conditions. Recent studies have shown that inserting an oxygen (O) atom, which has merely an extra electron than nitrogen atom, enables an extremely effective substitution process. Zhang and coworkers created the double oxygen doped g-C_3N_4 (OPCN) materials through easy thermal copolymerization (Yuejie et al., 2019). They used DFT to determine the optimum oxygen replacement sites and discovered that the inserted oxygen atoms preferred to simultaneously substitute both the sp^2-hybridized nitrogen atoms at the *para*-position of melem unit (Fig. 9d). In this situation, a delocalized arrangement developed on the OPCN surface, allowing carriers to migrate, while efficiently preventing electrons/holes recombination. Furthermore, under VL, the removal performance of the optimized OPCN for several organic contaminants was enhanced, and the photocatalytic performance for BP was roughly 9 times than pure g-C_3N_4 under solar light illumination.

1.7. Defect engineering

In contrast to the approaches described earlier, adding vacancies defects in g-C_3N_4 structure is an excellent approach for modifying the thermodynamic properties, kinetics, and mechanism of photocatalytic processes (Taha et al., 2021; You, 2017; Hayat, 2021; Khan, 2021; Ullah, 2021). Vacancy defects have following impacts on g-C_3N_4 photocatalytic efficiency. (1) capturing and storing electrons, leading to separation of charge; (2) Improvement of the ability to capture light and extension of the light response edge into the near-IR region through defect state; (3) Modification of the adsorption properties of the specific contaminant, hence enabling the targeted adsorption of various contaminants by g-C_3N_4; (4) The concentration, geometry, and position of vacancy defects all have an impact on the characteristics of g-C_3N_4. As a result, investigating vacancy flaws, particularly N and C vacancies, is crucial.

1.7.1. N-vacancy defects

N-vacancies may develop the electronic structural distortions, resulting in disrupted energy areas and aiding the exciton dissociation and transmission (Yw et al., 2020). Hydrogen bonds serve as strands in polymeric melon units having amino groups (NH/NH_2) thus, g-C_3N_4 having N vacancy might be generated by removing the amino groups by means of high calcination. Zhou and colleagues discovered that difference of energy at the disordered junction induced by a N vacancy is at least 0.35 eV, that is enough to split singlet excitons having Eb of 0.2 eV into free holes and electrons (Zhou, 2020). These available electrons are used to produce activate oxygen, resulting in a significant amount of OH ions, which gives superior photocatalytic performance of the modified g-C_3N_4. Wang and coworkers created an N vacancy containing g-C_3N_4 with increased crystalline phase by using oxalyl dihydrazide (ODH) as an atmospheric modifier, which they named ODH-CNX can be seen in Fig. 10a (Yw et al., 2020). DFT simulations revealed that lowest occupied molecular orbital (LUMO) of ODH-CNX tilted toward the C-C bond, when contrasted to the electronic distribution of pure g-C_3N_4, resulting in non-coplanar HOMO and LUMO, that were advantageous for carrier production (Fig. 10b). Furthermore, the insertion of N vacancy resulted in a 0.13 eV reduction in the Eg value. Furthermore, the experimental findings revealed that crystalline structure and N vacancies improved charge transfer, exciton dissociation and VL capture. Furthermore, N vacancy promotes charge separation and transfer. Cao et. al. synthesized g-C_3N_4 having rich N vacancies (NV-g-C_3N_4) by processing melamine in a nitrogen environment and used it for carbamazepine degradation. (Cao, 2019; Li, 2020). The findings indicated that the deterioration rate of NV-g-C_3N_4 enhanced towards 270 % in comparison with bulk g-C_3N_4, that was due to capturing of electrons by N vacancies, hence limiting charge recombination. Liang et. al., examined the relation between degradation efficiency and N-vacancies (Liang, 2019). The developed catalysts greatly improved photocatalytic efficiency, because negative shift occurs in CB region of g-C_3N_4 due to N vacancies and improved both photo response and separation of charges.

1.7.2. C-vacancy defects

Multiple investigations have shown that introducing C-defects into g-C_3N_4 framework is a very attractive technique for optimizing carrier separation/transport (Dong, 2017). In general C vacancies could be produced by heating g-C_3N_4 in different environment such as ammonia (Liang, 2016; Ge, 2020), carbon dioxide (Ho, 2018), or argon atmosphere (Dong, 2016), etc. Liang and coworkers created C-vacancy modified g-C_3N_4 (VC–C_3N_4) using a simple two-step calcination procedure for increased photocatalytic performance (Liang, et al., 2018). C-vacancies can trap electrons, limit charges recombination, and transmit captured electrons to absorbed oxygen, boosting O_2 production (Fig. 10c). Wang et. al. demonstrated that photocatalytic efficiency of C-vacancy integrated g-C_3N_4 was 1.65 times greater than pure g-C_3N_4 (Wang, 2021). The researchers created oxygen doped g-C_3N_4 having C-vacancy (VC-OCN) and utilized it to degrade atrazine (ATN) and p-nitrophenol (PNP). The C-vacancies concentration might be altered by adjusting the formaldehyde concentration. Likewise, the enhanced photocatalytic effectiveness of VC-OCN was correlated to the C vacancies, that suppressed the charge recombination and encouragement of adsorption of oxygen molecule. In the end, both C and N vacancies cause the Eg value of g-C_3N_4 to drop, because of its impurity state (Li, 2020). The CB of g-C_3N_4 is connected with the 2p orbital of carbon, and the C-vacancy causes the CB to shift positive (Li, 2016), so the intermediate gaps occur below the CB. In contrary, the VB of g-C_3N_4 is connected to the 2p orbital of nitrogen, and the N vacancy produces a negative shift in the VB, allowing the intermediate gap to form above the VB. Insufficient vacancies have little influence on the electronic configuration, while an excess of vacancies may act as carrier recombination centers, thus lowering its efficiency.

1.8. Heterojunction building

g-C_3N_4 has a multilayer structure that can be combined with other semiconductors substances. For carrier excited photocatalysis, heterostructures formed by intimate interaction between different substances have the following advantages: First, photoinduced electron hole pair could be spatially separated due to the of two distinct semiconductors heterojunction (Kongto, 2022; Zhang, 2021; Hayat, 2021; Rehman, 2021; Uddin, 2021; Hayat, 2021; Arif, 2021; Hayat, 2021).

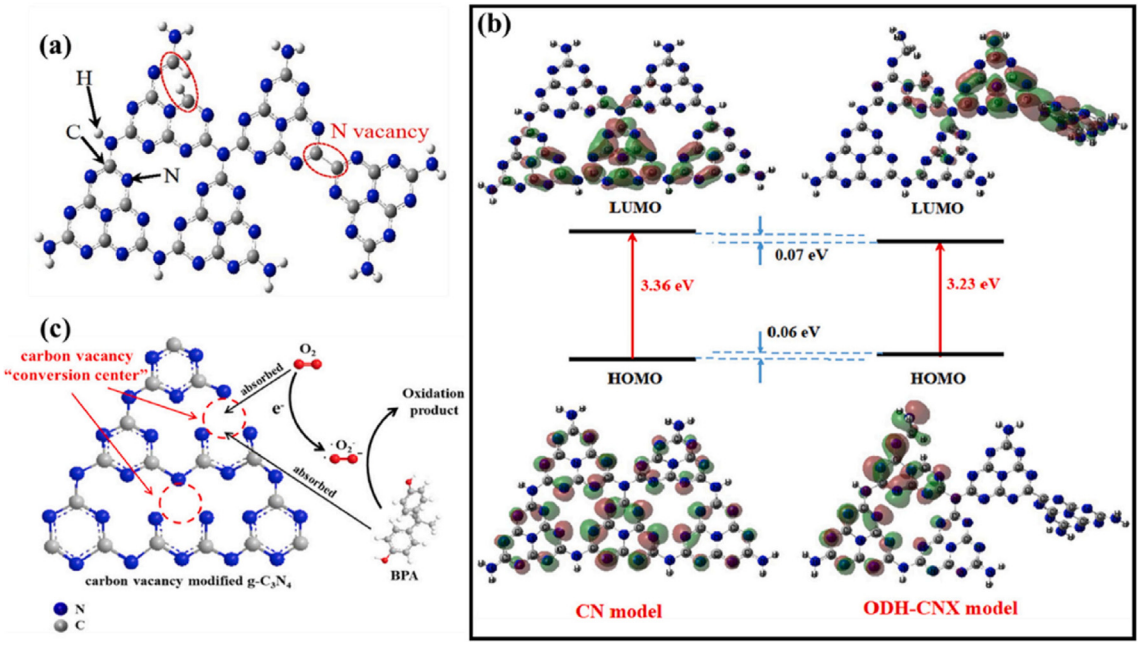

Fig. 10 (a) Structures description of ODH-CNX with N defects, and (b) the best systemic electronics pattern of CN and ODH-CNX, and the predicted potential levels. Reprinted with permission from Yw et al. (2020) Copyright © 2020, Elsevier; (c) Pathway of g-C_3N_4 activation upon C vacancies alteration. Reprinted with permission from Liang et al. (2018). Copyright © 2019, American Chemical Society.

Second the spectral response could be enhanced or the oxidation/reduction ability could be increased by combining semiconductors of various band gaps (Wang, 2021). For exciton-generated photocatalysis, the construction of a heterostructure has been demonstrated to aid in the regulation of exciton energy state and binding energy (Zhou, 2020). Furthermore, the heterojunction internal electric field can cause the reverse flow of electrons and holes, resulting in exciton dissociation. Based on how charge carrier move, heterojunction can mostly be put into three groups: traditional/conventional heterojunction (types I-III), P-N heterojunction, and Z-scheme heterojunction, as seen in Fig. 11 (Zhang, 2021).

1.8.1. Conventional/traditional heterojunctions

1.8.1.1. Type-I and Type-III heterojunctions. In accordance with band position of the two semiconductors that make up the heterojunction. There are usually 3 kinds of traditional heterojunctions (Fig. 11a)

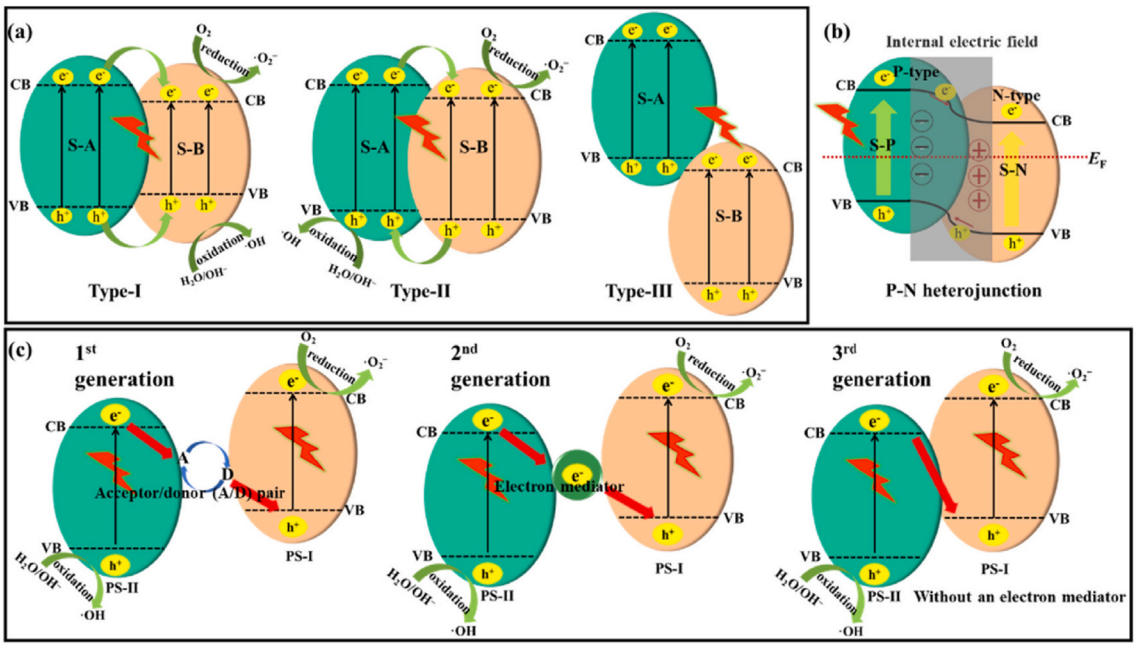

Fig. 11 Electron transport diagram using (a) three kinds of traditional heterostructures, (b) P–N heterostructure, and (c) three phases of Z-scheme heterostructure. Reprinted with permission from Zhang (2021). Copyright © 2021, Elsevier.

(Zhang, 2021). On photoexcitation, the electrons in VB of these 3 kinds of heterojunctions could be stimulated into the associated CB, generating positive holes in the VB. For type-I, semiconductor A (S-A) exceeds the semiconductor B (S-B), meaning that S-A has a much more substantial redox ability than S–B. Consequently, the electrons in the CB of S-A and holes from the VB of S–B move to the CB and VB of S-B. This form of charge transport channel could lower the Eg of the composite, extending the light response range, which is helpful for photocatalytic efficiency. Consequently, both electrons and holes are saturated on S–B, preventing effective separation of photoinduced carriers. Consequently, the redox ability of composites deteriorates dramatically. In type-III, the two semiconductors are incapable of forming a heterostructure, because their energy band locations do not overlap and the photoinduced electrons and holes cannot transfer to one another.

1.8.1.2. Type-II heterojunction. Type-II heterojunctions are the extensively kind of traditional heterojunctions (Fig. 11a) (Li, 2020). Two kinds of Type-II heterojunction formed by g-C_3N_4 and semiconductors. (1) Whenever a semiconductor has a high CB value (serving as S-A), g-C_3N_4 function as S–B, and electrons on S-A transfer to the CB of g-C_3N_4, while holes gather on the VB of S-B. Ehsan et. al. developed a g-C_3N_4/ZnSe hybrid photocatalyst for high photocatalytic performance. Analysis demonstrated that type-II heterojunction developed between ZnSe and g-C_3N_4. Due to its excellent surface charge transport pathway, the composite exhibited 1.81 and 1.57 times greater efficiency than g-C_3N_4, respectively (Ehsan, 2020). (2) When the CB of semiconductors is low (functioning as S–B), g-C_3N_4 functions as S–A. In this situation, the electrons in g-C_3N_4 can move to the CB of S–B, and this is also very rare type. Zhu and coworkers synthesized g-C_3N_4/$BiPO_4$ heterostructure catalysts using varying concentrations of g-C_3N_4 for the degradation of TC using the ball milling technique. After 120 min of exposure to light, the optimum material had 97% degradation of the TC, and the greatly improved photocatalytic activity was closely linked to the efficient transport channel owing to the successful building of Type-II heterojunction. Hu and coworkers (Hu, 2019) obtained comparable findings when they developed carbon doped g-C_3N_4 (BCCN)/TiO_2 composites (BCCNT) for improved photocatalytic performance. The improved photocatalytic efficiency was strongly linked to the creation of a type-II heterojunction between BCCN and TiO_2. DFT simulations can be used to examine the viability of Type-II heterojunction fabrication. (Sun, 2021). Sun and coworkers used electrostatic self-assembly to create 0D SnO_2 nanoparticle composite with 2D g-C_3N_4 for Rhodamine B degradation. (Sun, 2021). The direction of charge transport was identified using DFT simulations and 3D charge density. A positive mean of electron density change was discovered on SnO_2 (1 1 0), whereas a negative mean of electron density variation was seen on g-C_3N_4 nanosheets (CNNSs), revealing that electrons concentrated on SnO_2 (1 1 0). As a result, it was verified that a type-II heterojunction can occur among SnO_2 (1 1 0) and CNNSs. The degrading performance of the material was 1.5 and 32.3 times greater than that of g-C_3N_4 and SnO_2.

1.8.1.3. P–N heterojunction. Even Type-II can help in the separation of e^-—h^+ pairs, by preventing the charge separation due to electrostatic repulsion. In general, the CB and VB of N-type semiconductor (S-N) are greater than a P-type semiconductor (S-P). The fermi level (EF) of semiconductors is in the middle of CB, but it is in the band gap for semiconductors. Furthermore, the EF of S–N is near to CB, whereas the EF of S-P is near to VB. Work function (Wf) is inversely proportional to the fermi level (EF). Fig. 11b depicts the charge transfer mechanism. Once S-N and S-P together, trend is towards equilibrium, because the EF values are different. Consequently, electrons moved from P-type to N-type, until their EF values achieve equilibrium. The surface of N-type and P-type semiconductor are loaded with positive and negative charges, therefore generating the internal electric field from S-N to S-P direction. The photoinduced holes and electrons are propelled in the reverse way by the internal electric field, boosting charge separation ability under solar light illumination. The creation of P-N heterojunction could be verified by analyzing the compound semiconductor M S curve, which has both positive and negative slopes (Li, 2020). For example, Babu et. al. created P-N heterojunction in boron doped g-C_3N_4 composites with $BiVO_4$ (BCN/$BiVO_4$) by deposition of N-type $BiVO_4$ on P-type 1 % wt boron doped g-C_3N_4 and used it to remove Cr(VI) metal (Babu, 2019). The highly efficient catalyst was 50% $BiVO_4$/B-doped g-C_3N_4, for enhanced photocatalytic performance. Mass spectrometry studies found that the optimum material had an inverted U-shaped curve, suggesting the existence of negative and positive slopes, revealing the existence of P-N junction. The enhanced photocatalytic capabilities of the resultant material might be attributed to two reasons: (1) P-N junction facilitates the improvement of VL absorption; (2) P–N heterojunction can help electrons/holes pair separation while also decreasing their recombination likelihood.

1.8.1.4. Z-scheme heterojunction. The Z-scheme heterojunction system, that could be separated into three generations for addressing the problem of photocatalyst redox capacity caused by P-N and Type-II was created (Fig. 11c). Bard in 1979 introduced the concept of Z-scheme heterojunction (first generation), in which the transfer of charges was accomplished via acceptor–donor electron, that was mostly used in the aqueous phases (Bard, 1979). To expand the Z-scheme system uses, Tada and coworkers in 2006 studied Z-scheme system having all Solid state phase (second generation) in which the noble metal replaced by the electron mediator (Tada, 2006). But, due to the costly nature of valuable metals and its great light absorption capability, it is not suitable for practical uses. Vast studies on mediator free photocatalysis started in 2009 to develop more cost-effective photocatalysts (QingáLu, 2009), and Yu and colleagues introduced the direct Z-scheme system in 2013 (Third generation). Yu and his team made Ag_3PO_4/AgBr/g-C_3N_4 with dual Z-scheme system for improved the photocatalytic performance of Z-scheme heterostructure (Yu, 2020). Ag_3PO_4/AgBr-20%/g-C_3N_4 was indeed the best photocatalysts, because it was able to build a dual Z-scheme junction. The photoexcited electrons present in AgBr moved to the VB of g-C_3N_4, whereas the photoexcited holes in AgBr recombined with the photoexcited electrons in the CB of Ag_3PO_4 under solar light. In comparison to the binary Z-scheme, this ternary Z-scheme increased the separation of charges and composite material performance. Furthermore, unlike in a normal heterojunction (Fig. 12a), the oxidation and reduction reactions of dual Z-scheme system happened separately in the CB of g-C_3N_4 and the VB of Ag_3PO_4 (Fig. 12b), showing that the Eg of the composite rose, hence enhancing photocatalytic efficiency.

1.8.1.5. Isotype heterojunction. Furthermore, g-C_3N_4 may also produce an isotype heterojunction by forming heterojunctions with other semiconductors. It is widely recognized that g-C_3N_4 could be synthesized through condensation of precursors (urea, thiourea and melamine). g-C_3N_4 having varied band gap configurations could be synthesized from several precursors. The isotype heterostructure g-C_3N_4/g-C_3N_4 like Type-II (Wang, 2017), Type-I (Dong, 2015), P-N type (Liu, 2016), N-N type (Zhou, 2017), could be prepared by various precursors. For instance, Xu and coworkers used thermal copolymerization to synthesized 3D g-C_3N_4 heterojunction blocks by assembling nanowires and nanosheets building blocks (Fig. 13a) (Xu, 2019). The hierarchical porous framework created by combining nanowires and nanosheets boosted the utilization of light dramatically. Concurrently, the widespread Type-II isotype heterojunctions created an internal electric field, that aided separation of carrier and exciton dissociation (Fig. 13b). Consequently, the photocatalytic efficiency of generated 3D g-C_3N_4 units rose by >10 folds.

In particular, the isotype heterostructure could also be created by altering the crystalline nature of g-C_3N_4. Wang and coworkers synthesized the semi crystalline g-C_3N_4 by chloride assisted hydrothermal

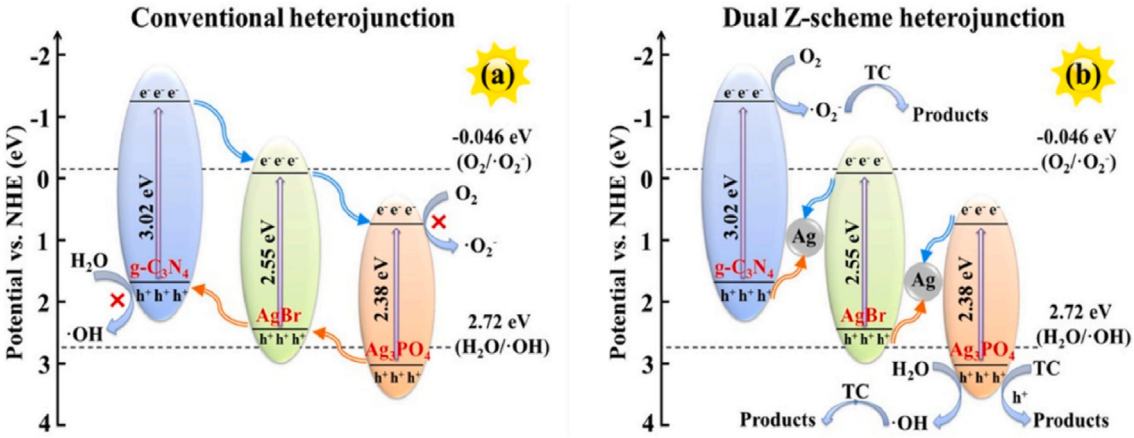

Fig. 12 Proposed pathway employing Ag_3PO_4/AgBr-20 % g-C_3N_4: Traditional heterostructure (a) and double Z-scheme heterostructure (b). Reprinted with permission from Yu (2020). Copyright © 2020, Elsevier.

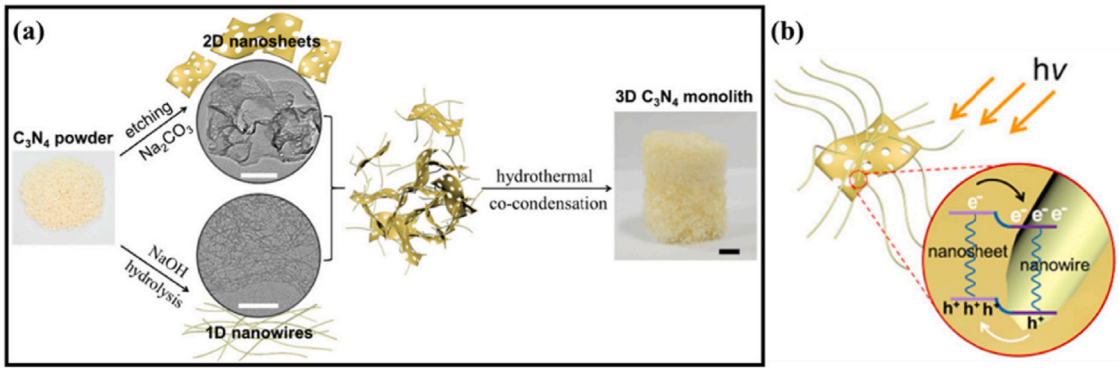

Fig. 13 Schematics of (a) the fabrication of 3D microstructural g-C_3N_4 with isoform heterostructures and (b) the isoform heterostructure fabricated at the interface region of g-C_3N_4 nanostructure and nanorods. Reprinted with permission from Xu (2019).

treatment and they got Type-II isotype heterojunction at disordered-ordered interface (Fig. 14a–b) (Wang, 2017). The rapid passage of electrons at crystalline units and the blockage of holes in networks having poor crystallinity enabled for efficient rise in exciton dissociation at the junction.

2. 2-Dimensional g-C_3N_4

2D-based materials have an extensive specific surface area, good crystallinity, numerous choices for host–guest interactions, maximum light absorption, and enhanced charge carrier separation due to their 3D analogues (Wang, 2012). Recently, g-C_3N_4 has become one of the most promising heterogeneous photocatalysts in the 2D nanomaterials field. To synthesized g-C_3N_4 nanosheets, the Ping and his colleagues proposed a simple approach called "etching" by annealing of bulk g-C_3N_4 in the air directly (Kato and Kudo, 2001). The bulk g-C_3N_4 can be reduced to the appropriate nanoscale thickness using this approach, which removes hydrogen-bonding interlayers through one oxidation, representing an easy, inexpensive and scalable synthesis. A blue shift in the intrinsic absorption edge of the UV–vis spectra is observed in resulting nanosheets compared to the bulk (Fig. 15) (Yu et al., 2004).

Similarly, the blue shift in the fluorescence emission spectra at 20 nm further confirms the increase in the band gap of nanosheets (2.97 eV), compared to their bulk intermediates (2.77 eV). The band gap has been larger, because of quantum confinement (Niu, 2012). It was found that the pristine g-C_3N_4 nanosheets exhibited semiconducting qualities, implying that the electron transport takes place within the nanosheet plane by analyzing their IV curves for related electronic properties. The bulk g-C_3N_4 had low electrical conductivity, as evidenced by the absence of any current, when a bias range of −10 to 10 V was applied. Furthermore, the lifetime of charge carriers in the nanosheets using time-resolved fluorescence decay spectra exceeded from that of bulk g-C_3N_4. According to Xiadong and co-workers, a new liquid exfoliation strategy has been proposed as a low-cost and environmentally friendly method in order to fabricate the ultrathin nanosheets from bulk g-C_3N4 (Rochkind et al., 2015). Through the liquid exfoliation route, ultrathin nanosheets of g-C_3N_4 were designed, which may be due to their high polarity. The exfoliated g-C_3N_4 revealed free-standing nanosheets at 120 nm wide that were practically transparent and showed a well-defined Tyndall effect. The photoluminescence spectra (Pl) of these g-C_3N_4 nanosheets were highly stable, when exposed to an acidic or alkaline envi-

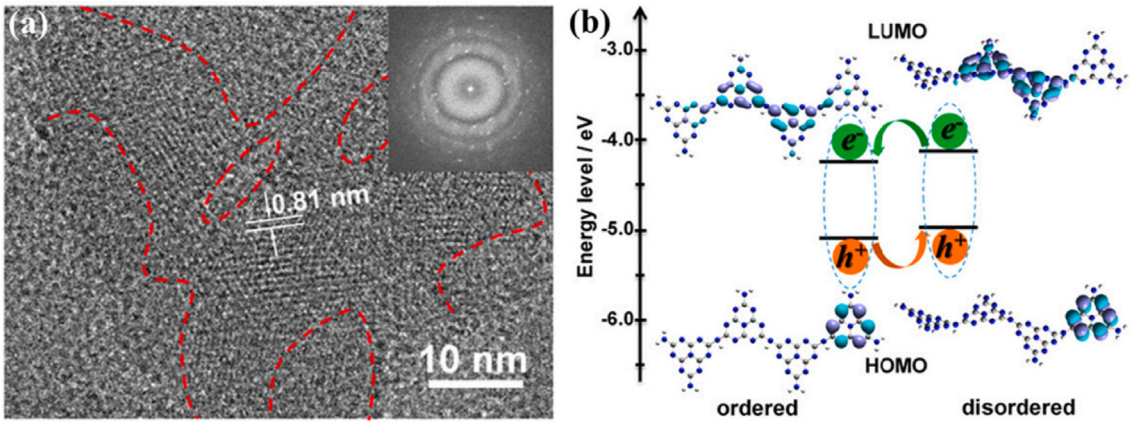

Fig. 14 (a) HR-TEM photograph of semicrystalline g-C_3N_4, and (b) Type-II isoform heterostructure created at the orderly disorderly junction and modelled using DFT analysis. Reprinted with permission from Wang (2017). Copyright © 2017, American Chemical Society.

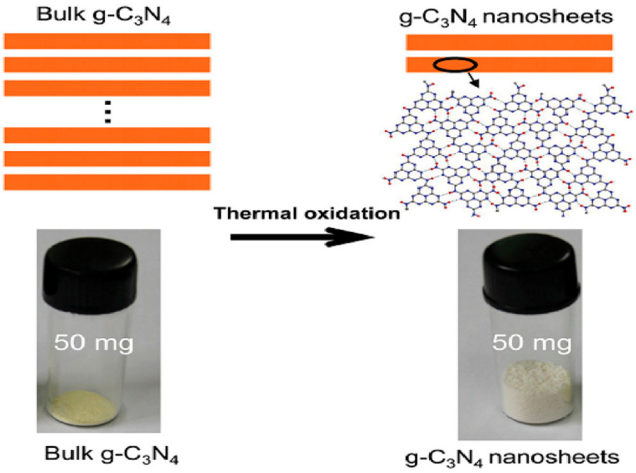

Fig. 15 Thermal exfoliation is a low-cost and green method to prepare ultrathin g-C_3N_4 nanosheets from bulk g-C_3N_4 in water. Reprinted with permission from Niu (2012). Copyright © 2012, John Wiley and Sons.

ronment. However, it was dependent on PH of material. The g-C_3N_4 nanosheets exhibit a superior photo-absorption over the bulk counterpart, leading to an unusually high PL quantum yield of up to 19.6 %. Researchers found that liquid exfoliation of g-C_3N_4 led to nanosheets with better photocatalytic efficiency for the breakdown of organic contaminants than the bulk g-C_3N_4 (Fig. 16) (Barbero and Vione, 2016; Styring, 2012; Zhang, 2013).

2.1. 1-Dimensional g-C_3N_4

One-dimensional nanostructures have recently gained immense interest as photocatalysts, due to their distinctive morphology and photophysical properties (Listorti et al., 2009; Chen et al., 2015; Bai, 2013). The nanorods with variable aspect ratios were synthesized by refluxing g-C_3N_4 nanoplates in different solvents and variations of time (Nosaka and Nosaka, 2017). An exfoliation process and subsequent re-growth of individual nanosheets resulted into the 'rolling up' nanorods from g-C_3N_4 nanoplates (Bai, 2013). This study investigated the photocatalytic activity of the as-prepared nanorods for the degradation

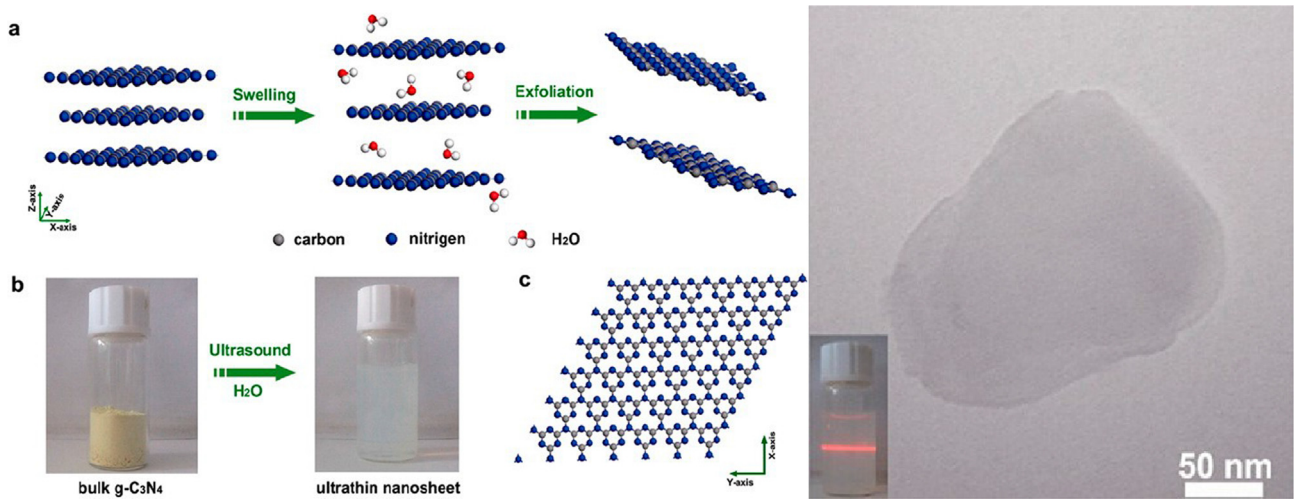

Fig. 16 Liquid exfoliation route as a low-cost and green method to prepare the ultrathin g-C_3N_4 nanosheets from bulk g-C_3N_4 in water. Reprinted with permission from Zhang (2013). Copyright © 2013, American Chemical Society.

of methylene blue (MB) under visible light (>420 nm). These nanorods were shown to be 50–100 % more active and stimulated under visible and solar light as compared to g-C_3N_4 nanoplates. Zhihong and co-workers demonstrated that the reactive thermolysis of mechanically activated molecular precursors, such as $C_3N_6H_6$ and CN_3Cl_3, under heat treatment led to the large-scale production of well-aligned g-C_3N_4 nanorods (Kubacka et al., 2012). These PL emission and UV–vis absorption of nanorods demonstrate their unique optical characteristics. A template of monodispersed, chiral, mesostructured silica nanorods was easily generated via ammonia-catalyzed hydrolysis of tetraethyl orthosilicate with F127 cetyltrimethylammonium bromide (CTAB) surfactants in order to construct the uniform g-C_3N_4 nanorods. The hexagonal mesostructured porous silica nanorods allowed g-C_3N_4 condensation within the pores (Frank and Bard, 1977). The photocatalytic activity of the g-C_3N_4 nanorods was found to be significantly higher than that seen in the presence of triethanolamine and 1 % of Pt (Lee, 2016) as cocatalysts. Nanorods made from hydrous melamine nanofibers precipitated from an aqueous solution of melamine can also be synthesized by direct calcination (Li, 2007). The as-synthesized materials demonstrate high photocatalytic performance due to high interfacial area supplied by porosity. For hydrogen (H_2) evolution, a visible light photocatalytic activity in the presence of triethanolamine was enhanced by adding oxygen atoms to the g-C_3N_4 matrix, which resulted in a more effective separation of electron/hole pairs. Similarly, a simple wet-chemical approach was also reported for the synthesis of nanofiber-like g-C_3N_4 structures with an average diameter of few nm and a length of 100 nm (Wang, 2012)., The nanofibers of g-C_3N_4 showed a slight blue shift of 0.13 eV compared to that of bulk g-C_3N_4, due to better packing, electrical coupling, and quantum confinement effects. The g-C_3N_4 nanofibers had a substantially greater photocatalytic activity than bulk g-C_3N_4 and were more stable for Rhodamine B photodegradation. The g-C_3N_4 nanotubes can be synthesized by heating melamine in a compact arrangement that favors tubular forms (Fig. 17a, d) (Wang, 2014). Commercial, low-cost, and large-scale applications were possibly made due to lack of organic templates in this method. There is potential for blue light fluorescence in this newly synthesized material, as it exhibits strong fluorescence at approximately 460 nm. The visible-light photocatalytic activity of these g-C_3N_4 nanotubes was superior to that of bulk g-C_3N_4 or P25 TiO_2 as a reference (the latter is unsurprising since pure titania is a UV band gap material). Moreover, Muhammad and coworkers also used HNO_3 pre-treatment of melamine in order to fabricate tubular g-C_3N_4 (Kato and Kudo, 2001). The g-C_3N_4 nanotubes once again became capable of degrading both MB and methylene orange (MO) and were found to be more stable than bulk g-C_3N_4 under visible light. The superior activity of the nanotubes was attributed to their larger surface area (182 m^2/g^1) and improved light absorption and charge separation/transfer. The g-C_3N_4 nanotubes can also be generated through rolling up nanosheets via an easy water-induced morphological transition, without the use of organic solvents and thus in support of green chemical principles (Jing and Guo, 2006).

Dicyandiamide (DCDA) and NaCl crystals have been used as structure-directing agents in order to generate the ribbon-like nanostructures of the g-C_3N_4. These ribbon-like g-C_3N_4 nanostructures have intriguing optical and electrical features, including a substantial blue shift in their absorption spectra corresponding to a rise in the band gap from 2.7 eV to 3.0 eV (Fig. 18) (Yuan, 2014). For that, a possible explanation is that the nitride pores are functionalized with cyano groups and Na^+ ions. While bulk g-C_3N_4 emitted yellow-green light, ribbon-like g-C_3N_4 emitted blue light roughly at 400 nm under 365-nm excitation. Nevertheless, no research has been done on the potential photocatalytic properties of these ribbon-like g-C_3N_4 nanostructures.

2.2. 0-Dimensional g-C_3N_4

0D materials like quantum dots are of tremendous interest (Wang, 2014). As, thermochemical etching has been used in order to fabricate the g-C_3N_4 quantum dots. In this multi-step process, the g-C_3N_4 is thermally exfoliated into 2D nanosheets, and then etched with concentrated H_2SO_4 and HNO_3 in order to form 1D nanoribbons. This process is adjustable. The functional groups, such as carboxylic acid, could be

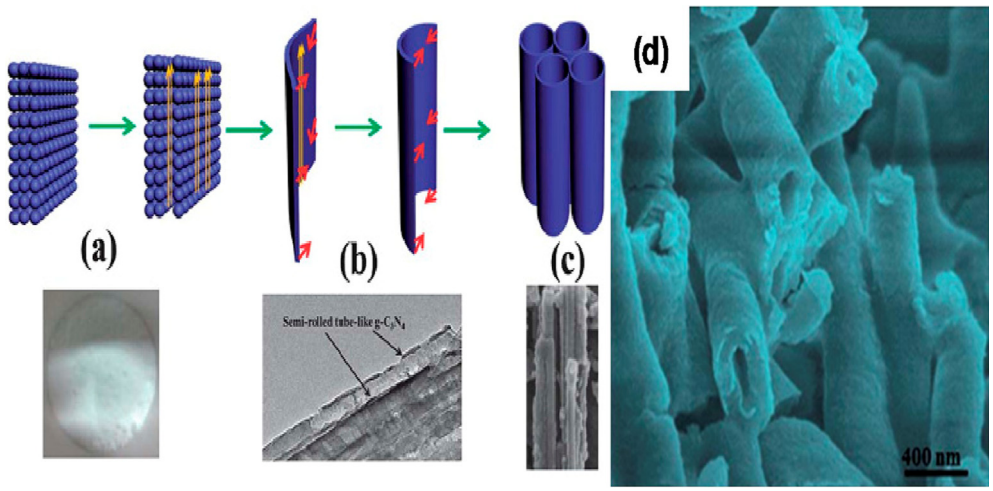

Fig. 17 (a–c) Synthetic strategy and corresponding (d) TEM image of g-C_3N_4 nanotubes. Reprinted with permission from Wang (2014). Copyright © 2014, Royal Society of Chemistry.

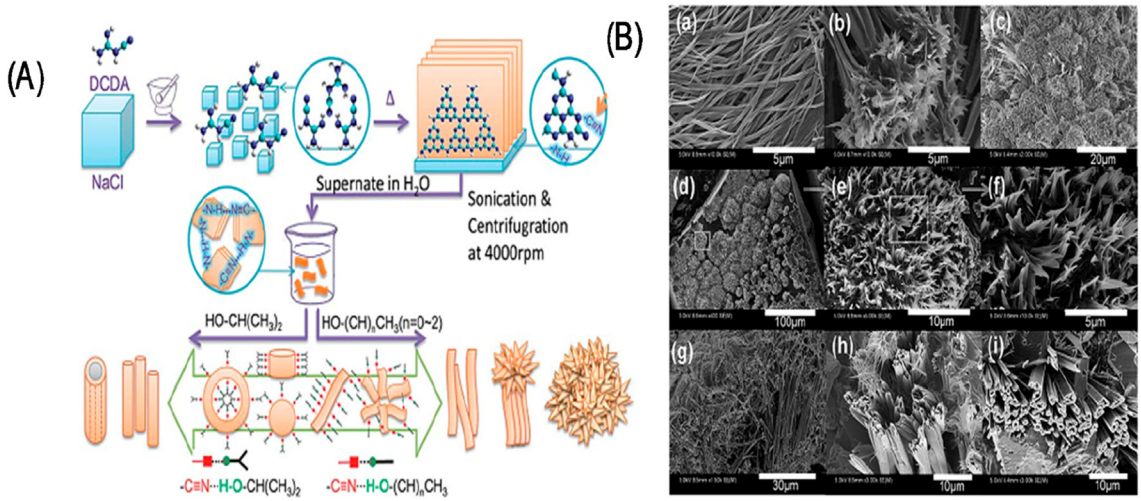

Fig. 18 Synthesis strategy (A) Ribbon-like g-C_3N_4 nanostructures (B) TEM image. Reprinted with permission from Yuan (2014). Copyright © 2014, Royal Society of Chemistry.

found at the margins and on the base of tri-s-triazine units, when some C–N linkages are oxidized. The preferential cleavage and the preferred orientation result in the formation of nanoribbons, that are approximately 10 nm in diameter and several hundred nanometers in length. The hydrothermal treatment converts nanoribbons into 0D quantum dots of 5–9 nm (Fig. 19) that are highly soluble in water and stable in solution for approximately eight months (Wang, 2014). For example, when 705–862 nm of light was irradiated onto a quantum dot, the emitted light was 350–600 nm in wavelength, thereby covering the whole visible spectrum. Anti-Stokes photoluminescence has been postulated as the mechanism for this upconversion. The g-C_3N_4 quantum dots hold great promise as a photocatalytic component for long-wavelength solar energy harvesting, Since they can convert NIR to visible light. The quantum dots increased the photocatalytic H_2 generation by platinized bulk g-C_3N_4 and P25. Remark rate-enhancements (up to 52-fold) were observed for the latter under visible light irradiation in the presence of a methanol sacrificial hole scavenger. Guoping and coworkers fabricated quantum dots for two-photon fluorescence imaging of cellular nucleus (Herron, 2015). A multi-step synthesis was used comprising the acid treatment of bulk g-C_3N_4 in order to generate a porous material and ultrathin nanosheets, followed by the addition of ammonia, hydrothermal treatment, and ultrasonication of the porous g-C_3N_4 nanosheets to liberate g-C_3N_4 quantum dots.

2.3. 3-Dimensional g-C_3N_4

The 3D nanomaterials can be used in order to create highly ordered 3D nanoporous g-C_3N_4 microspheres that can be synthesized without the need of templates, to create unique and highly efficient photochemical systems. The nano-porous g-C_3N_4 micro-spheres were first made from cyanuric chloride and melamine in acetonitrile, then thermally processed at

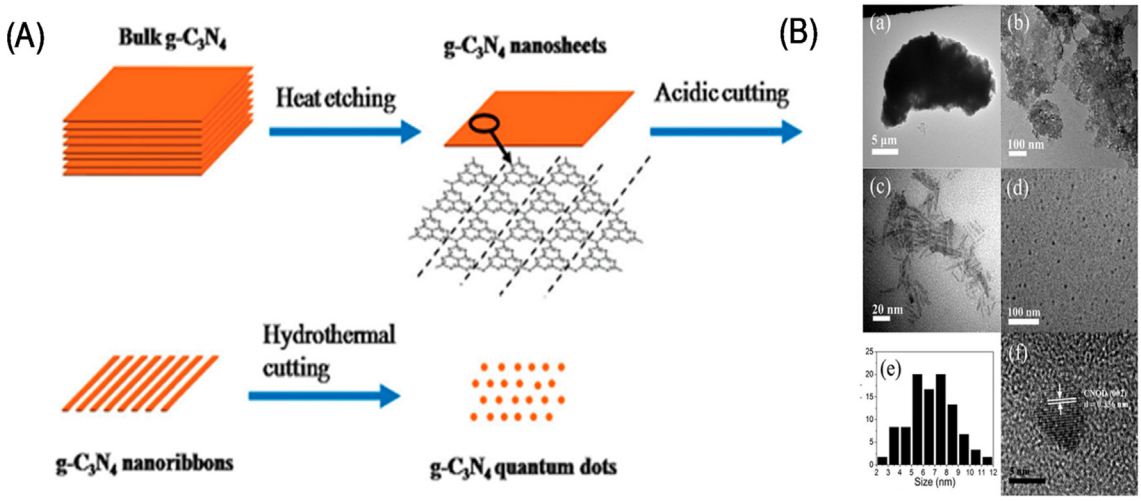

Fig. 19 (a) Synthesis of g-C3N4 nanosheets, and (b) TEM images of g-C_3N_4 quantum dots. Reprinted with permission from Wang (2014). Copyright © 2014, Royal Society of Chemistry.

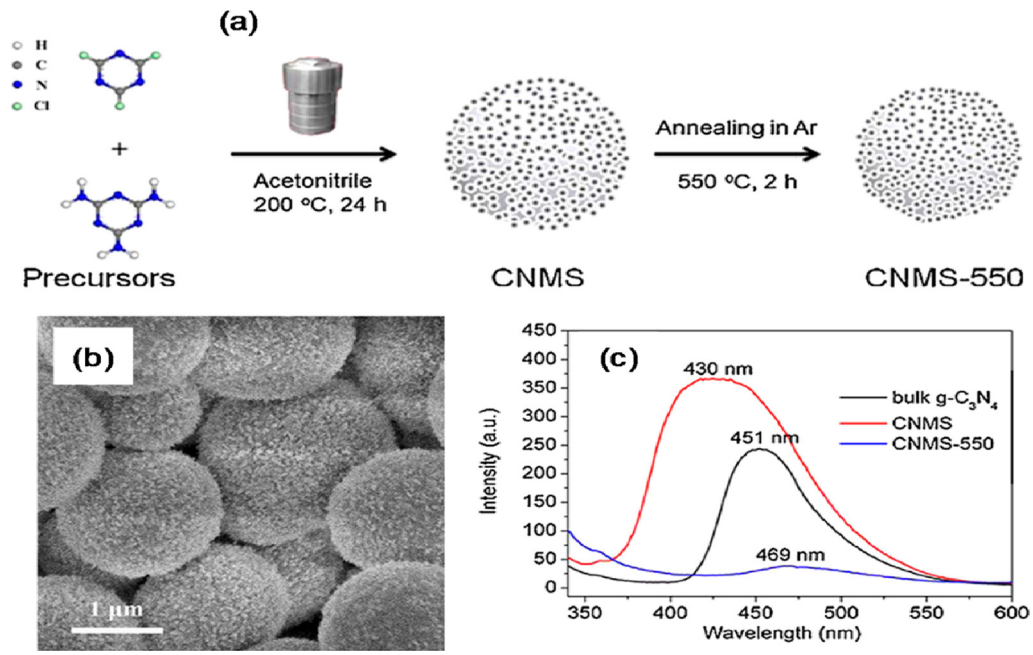

Fig. 20 (a) Synthetic strategy, (b) TEM image, and (c) room-temperature photoluminescence spectra of porous g-C_3N_4 microspheres. Reprinted with permission from Gu (2015). Copyright © 2015, Elsevier.

550 °C under argon in order to turn them into hierarchical g-C_3N_4 microspheres (Fig. 20) (Gu, 2015). These highly ordered g-C_3N_4 microspheres displayed a redshift compared to their bulk counterparts, due to a higher condensation and filling among different layers inside the micro-spheres. Hydraulic charge transfer in hierarchical g-C_3N_4 was suppressed by calcination, and the photoluminescence emission intensity of the bulk and uncalcined microspheres, respectively. A narrower band gap (2.42 eV), reduced electrical resistance, and increased photo-response of these microspheres enables highly effective harvesting and charge carriers separation generated by visible light. Jinshui and co-workers also generated highy ordered g-C_3N_4 nano-spheres, constituted of nano-sheet assemblies, using high surface area of silica nanospheres as sacrificial templates (Ong, 2016).

The silica template provides excellent cyanamide adsorption and a framework for producing the interconnected 2D g-C_3N_4 nanosheets during self-polymerization of the g-C_3N_4 polymer after heating. As a result, the silicon spheres demonstrate an outstanding thermal and mechanical durability, elevated temperature based synthesis of highly ordered g-C_3N_4 was possible, and g-C_3N_4 nanospheres might be easily detached via etching with an (NH_4HF_2) solution, while maintaining their spherical morphology. Fig. 21 shows how the highly ordered nano-spheres are fabricated from flat nanosheets that radiate from center (sphere surface) and formerly interconnect by forming a *meso*-porous shell (Zhang, 2014). This structure may be advantageous in photocatalysis, because it promotes both separation of charges and transport of mass (Fig. 21). Such kind of as-synthesized nano-spheres exhibited broader band gap as compared to bulk g-C_3N_4 owing to the effect of their quantum size. Also they have higher potential of light garnering toward whole optical range, particularly between (430 and 590 nm). It might be caused by several reflections (absorption) of incident light within the highly ordered structure and due to the existence of a higher number of defective sites linked through the revelation of low-coordination positions over strident ends of the integral nanosheets at the ends of the highly ordered *meso*-porous structure.

2.4. Hollow g-C_3N_4

The researchers have focused on designing and synthesizing hollow nanostructures having high intricacy by deploying their interior architecture, building units, chemical composition, and its geometry for improving the as-prepared materials performance in a wide variety of fields (Fu, 2018; Wang et al., 2012; Kizito, 2017). The hollow nanostructures is considered additional auspicious morphology for energy conversion and storage applications. The silica nanoparticles were used as templates in order to fabricate the hollow g-C_3N_4 nanospheres (Dong, 2014; Zhu, 2014; Sun, 2012; Kizito, 2017). Such hollow nanospheres are made of polymeric g-C_3N_4 and can withstand at 400 °C processing without the core–shell configuration (Fig. 22) (Sun, 2012). For example, the co-polymerization process could extend the π-system by anchoring aromatic motifs, which could red-shift the optical absorption by improving the separation of charge in shell deprived of d-blocking. This technique has turned the shell of hollow g-C_3N_4 nanospheres in order to boost the photocatalytic performance towards H_2 evolution in visible light. Young-Si et al. (Jariwala, 2013) demonstrate a direct facile chemical approach for assembling the triazine unit within the hollow g-C_3N_4 enabling the simultaneous textural tuning and photo-physical characteristics of g-C_3N_4.

2.5. Mesoporous g-C_3N_4

Mesporous photocatalysts have gotten a lot of research interest, because of their (relatively) high molecular mass transport in-pore, superior surface areas, higher quantum efficacy and,

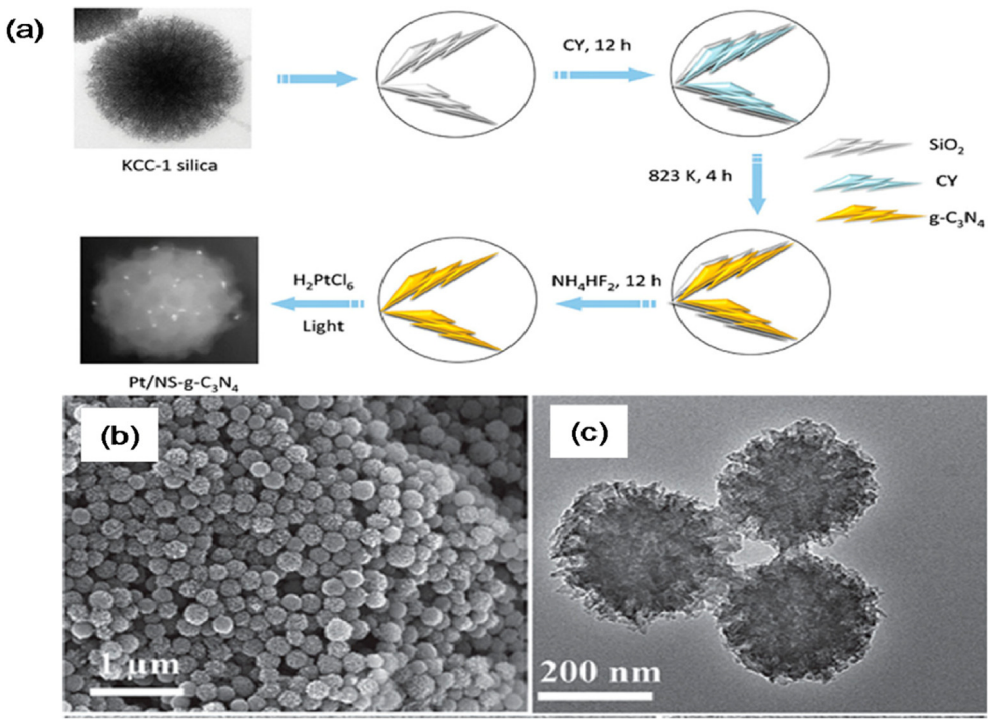

Fig. 21 (a) Synthetic strategy, and (b, c) Scanning electron microscopy and TEM images of hierarchical g-C_3N_4 microspheres. Reprinted with permission from Zhang (2014). Copyright © 2014, John Wiley and Sons.

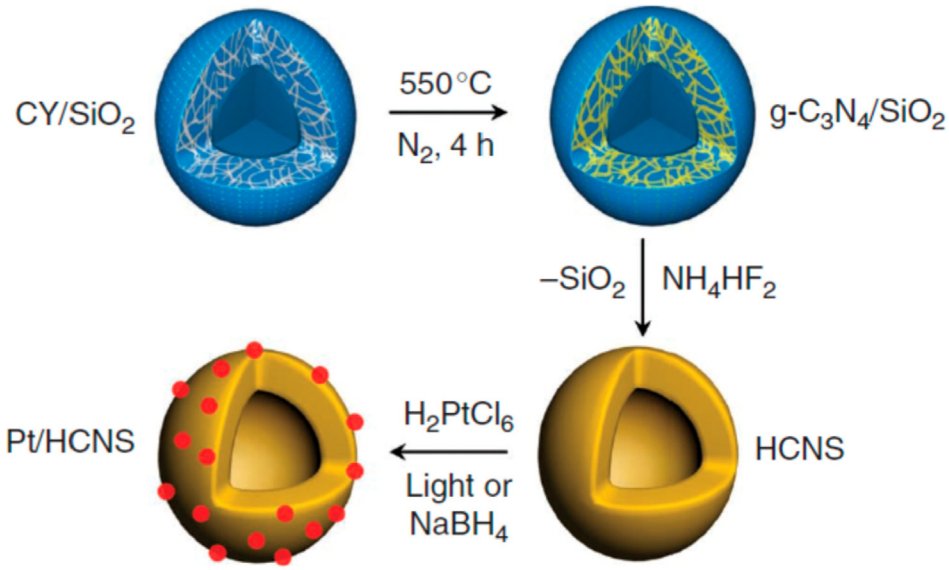

Fig. 22 Synthetic strategy for fabricating hollow g-C_3N_4 nanospheres. Reprinted with permission from Sun (2012).

prospects of improved light collecting via inner dispersion of incident light. The photocatalytic efficiency for H_2 generation was demonstrated in a recently synthesized mesoporous network of g-C_3N_4 nano-sheets (Fig. 23) (Han, 2016).

2.6. g-C_3N_4 based quantum dots

In recent years, quantum dots (QD, s) sensitized semiconductors have gotten a lot of attention, because their active sites are more visible. They have a quantum confinement effect, and have a special effect at the interface (Liu et al., 2020). Research findings have shown that quantum dots sensitized could effectively change the width of the band structure and increase the light response rate of semiconductors (Liang, 2020). Moreover, small size of quantum dots may lower the diffusion time of photoexcited electrons/holes from bulk to the surface, that enhance and boost their separation/isolation ability on catalyst surfaces, and significantly increase the quantum efficiency of

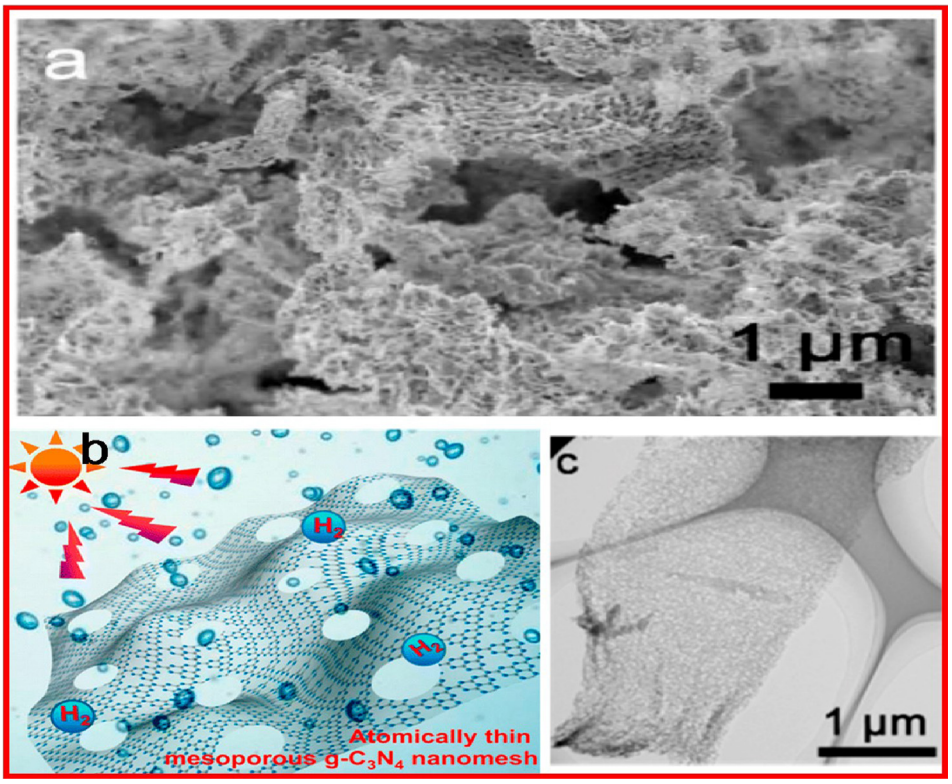

Fig. 23 (a) SEM images, (b) Sketch of photocatalytic H_2 from water splitting, and (c) TEM image of atomically thin, mesoporous g-C_3N_4 nanosheets. Reprinted with permission from Han (2016). Copyright © 2016, American Chemical Society.

the whole system (Liang, 2020; Yang, 2019). Liang and coworker (Liang, 2020) synthesized the P g-C_3N_4 (P-CNT) added with CdS QDs to make a new highly efficient (CdS QDs/P-CNT) using an in-situ oil bath method. The synthesized materials demonstrate a superior performance of photocatalytic water reduction (H_2 evolution) and was more stable. It also demonstrated a significantly increased in the optical absorption of light (Fig. 24a), which was attributed to CdS broad photo absorption edge (560 nm) (Zhou, 2018), that significantly improved the photocatalytic efficiency. Wang and coworker (Wang, 2020) used ice-assisted ultrasonic approach to synthesized black phosphorus quantum dots (BPQDs) incorporated with tubular g-C_3N_4 (BPTCN) nanohybrid with a 1D tubular framework. BPQDs refelecting an average size of 3.32 nm were scattered on the tubular CN in this system (TCN). The addition of BPQDs has greatly increased the photon absorption of BPTCN (Fig. 24b). Alternatively, BPQDs (act as electron mediator) were successfully added on TCN surface to generate a unique 0D/1D structure (interfacial PeC bonds) that slowed charge recombination (Liu, 2019). The PeC bonds established a close association between BPQDs and TCN, thereby increasing cycle stability and electron transfer (Fig. 24c–d) (Wang, 2020). Carbon quantum dots (CQDs) could change the transfer of photoexcited electrons and holes by acting as electron acceptor. Moreover, CQDs/g-C_3N_4 band alignment can help the isolation of photogenerated electron-hole pairs (Liu, 2016; Qin and Zeng, 2017). Li and coworkers (Di, 2016) fabricated g-C_3N_4 nanosheets loaded with CQDs using a simple solvothermal process in ethanol and improved the photocatalytic HER. When g-C_3N_4 nanosheets (CNNS) stimulated in light, CQDs act as photosensitizer, causing more absorption of light in order to transfer electrons to the CB of CNNS. Liu and coworkers (Liu, 2019) also employed CQDs to adorn the g-C_3N_4 by a simple polymerized process without affecting its skeletal framework. CQDs expanded the absorbance spectra of g-C_3N_4 and acted as charge carriers for photogenerated electrons, leading to increased its photocatalytic performance. Qin (2020) created a seed-mediated hydrothermal g-C_3N_4 modified by NiS_2QDs as a co-catalyst. The quantum confinement effect and small size of synthesized materials may give additional active sites and help in the formation of an intimate interface contact (Zhang, 2018; Chen, 2017). Furthermore, existence of NiS_2QDs in a NiS_2QDs/g-C_3N_4 might increase the quick transfer of photogenerated electrons from g-C_3N_4 to NiS_2QDs, considerably enhancing the effective photoexcited electrons and holes separation (Lu, 2018). Lu and coworkers fabricated a 0D/2D heterostructure by modifying Ni_2PQDs as a co-catalyst over the g-C_3N_4 surface, that could significantly boost HER and PEC activity due to improved light absorption and better photogenerated separation of electrons and holes.

Shakeelur and coworkers (Ar, s.r., 2020) created new type of catalyst composed of CdSeQDs loaded on thiol added g-C_3N_4 (TF-g-C_3N_4) and investigated for H_2 production. The fast rate of H_2 generation could be ascribed to the broad wavelength absorption and excellent reduction in recombination of electrons-holes pair of photocatalyst. Yang (2019) used a two-step approach for the synthesis of highly dispersed Co_3S_4QDs/g-C_3N_4 (Co_3S_4/CNNS) nanocomposites (water bathing and deposition). Co_3S_4QDs supplied additional active sites for HER, considerably widened the visible light range of CNNS, eased carrier separation and migration, and reduced the pho-

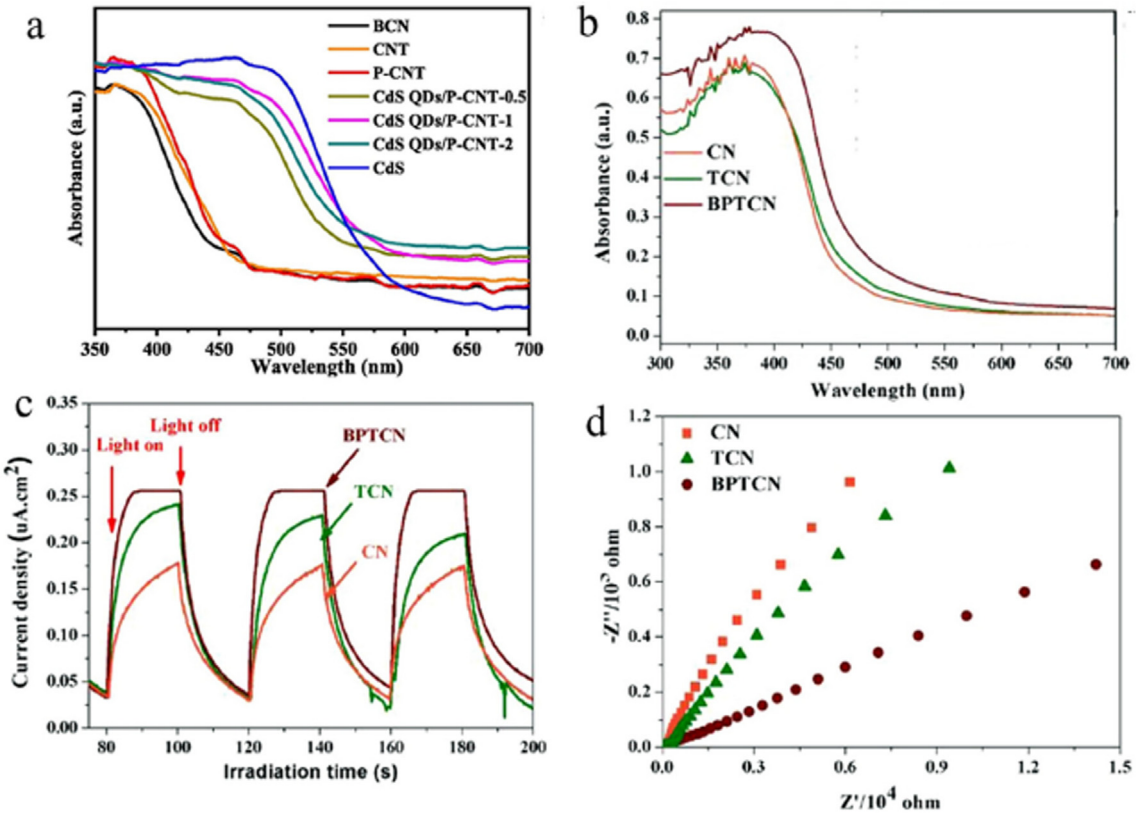

Fig. 24 (a). The optical absorption of synthesized materials (Zhou, 2018), (b) the BPQDs has greatly increased the photon absorption of BPTCN. (c, d) the increasing cycle stability and electron transfer between BPQDs and TCN materials. Reprinted with permission from Wang (2020). Copyright © 2020, Elsevier.

toinduced electron migration distance, resulting in high HER performance. Electrons from the VB of CNNS migrated to CB, and the sacrificial agent such as triethanolamine generated the holes on VB. Electrons were then transported to Co_3S_4-QDs. Co_3S_4QDs served as electron storage sites and hindered the recombination of photoexcited holes and electrons, resulting in a large quantity of active sites for HER. Following, the electrons had transferred from the CNNS to the Co_3S_4QDs reacted with the H_2O molecules to generate H_2, that was collected on the photocatalysts surfaces. QDs is a form of semiconductor material, have been identified as one of the promising architectures for suppressing the photoexcited electron-hole pair recombination (Fang, 2016). The strong quantum confinement provided by QDs is advantageous for shortening the path length of photogenerated charge transfer (Yang, 2019). On the other hand, faster the charge transport can boost the photocatalytic rates (Cao, 2013). While, QD can be used as a source of photoelectric response for the optical excitation (Meng, 2018). The considerably increased performance of g-C_3N_4 is due to the quantum dots acting as electron sources to capture electrons for improved separation and better light absorption.

3. Use of g-C_3N_4 in photocatalysis

g-C_3N_4 is an outstanding photocatalyst, which has diverse applications in different research fields (Su, 2012; Mandal and Ganguly, 2011; Anpo, 1987; Chen and Mao, 2007; Lu et al., 2009), including water splitting for hydrogen evolution reaction (HER), oxygen evolution reaction (OER) (Daniel and Astruc, 2004; Watanabe, 2014; Claus, 2000), fuel cells (Bell, 2003), CO_2 reduction to value-added products (Hu et al., 2008; Alenad, 2022; Hayat, 2021), organic synthesis (Kumar, 2016) and environmental remediation (Mclaren, 2009). Herein, we will specifically discuss the application of g-C_3N_4 in photocatalysis.

3.1. Solar fuel generation

During photocatalysis, solar fuel generation from water and carbon dioxide ($C0_2$) is the best way to produce H_2, O_2, hydrocarbons, and syngas as chemical feedstocks and sustainable energy (Li and Liu, 2011). For that purpose, g-C_3N_4 is considered as the best metal-free and excellent photocatalyst in the visible range. In the recent times, a lot of semiconductor materials were fabricated, for the photocatalytic water splitting (WS) under solar illumination. Feasibly, g-C_3N_4 photocatalyst have great potential for water splitting, since its CB and VB locations are in the right places (Yang, 2017). In general, there isn't much informative about photocatalytic oxygen progression and WS. This is even though the OER is quite complex than the HER, that only involves two electrons transfer. Fig. 25 is a simplest diagram of the photocatalytic water splitting (WS) into H_2 and O_2 over g-C_3N4 (Tian, 2019). When g-C_3N_4 is exposed to illumination, the photoinduced electrons move from VB to CB, having left gaps in VB. Electron-hole

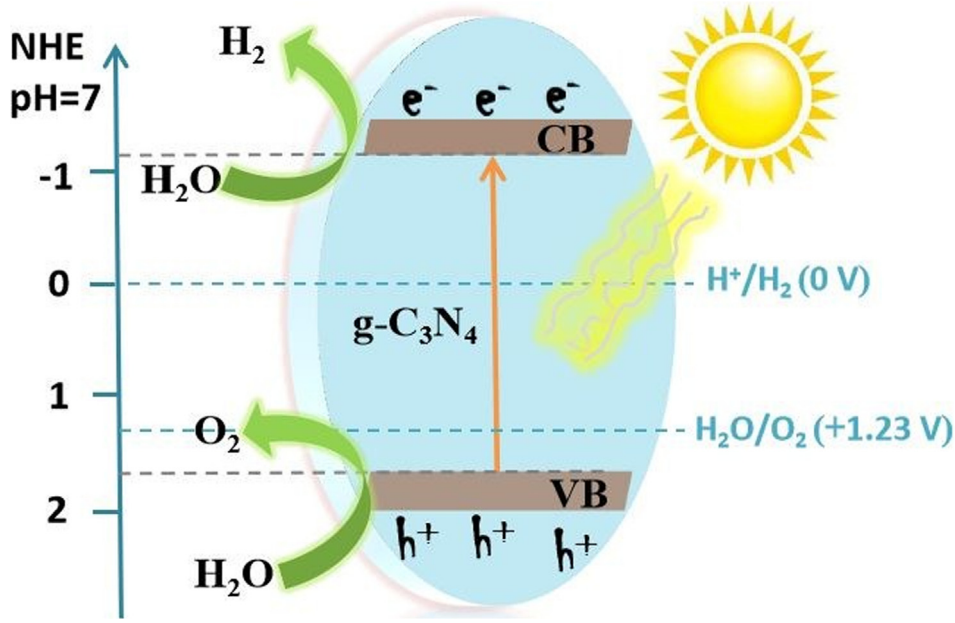

Fig. 25 Depiction of photocatalytic WS employing pristine g-C_3N_4 for H_2 and O_2 energy sources under illumination. Reprinted with permission from Tian (2019). Copyright © 2019, Royal Society of Chemistry.

pairs move individually to the activated and oxidation locations on the interface of g-C_3N_4 to turn water molecules into H_2 and O_2 in the mentioned expressions:

Reduction reaction:

$$2H^+ + 2e^- \rightarrow H_2 \quad (1)$$

Oxidation reaction:

$$2H_2O + 4H^+ \rightarrow 4H^+ + O_2 \quad (2)$$

Overall water splitting reaction:

$$2H_2O \rightarrow 2H_2 + O_2 \quad (3)$$

The photochemical H_2 and O_2 production, which existed at the g-C_3N_4/water surface is strongly based on the thickness, shape, and deficiencies of g-C_3N_4. The huge particular surface areas, powerful elevated optical absorbance, maximum charge isolation performance and plentiful surface reacting spots are all helpful for the photocatalytic H_2 formation of the g-C_3N_4. Since g-C_3N_4 does have a comparable complex architecture with graphite, the surface area might potentially be enhanced up to 2500 m^2/g^1 for ideal multilayer g-C_3N_4 (Sano, 2013). Although it is generally approximately upto 10 m^2/g^1 for the pure g-C_3N_4 material owing to the compaction of polymer nanostructure. Here are numerous papers stated earlier emphasizing the advantages for photocatalytic H_2 and O_2 development by morphological manipulation of g-C_3N_4. The AQE of the 2D g-C_3N_4 nanostructure with a diameter of ~1.2 nm, equivalent to ~4 layer, that was synthesized utilizing urea as starting material by a sustainable steaming reformer technique, may obtain up to 11.3 % at 405 nm (Fig. 26) (Yang, 2017). A surface area of 210 m^2/g^1 is achieved for such ~1.2 nm g-C_3N_4 nanostructure, that is 4.38 times greater than that of conventionally synthesized g-C_3N_4 by urea calcination. The produced nanostructure additionally promotes the charge transport, participating in the increased effective H_2 generation function.

Basically, developing nanosized unique shaped nanomaterials may reduce the diffusing route of charged particles, enabling fast movement of charges over the interface of materials to contribute in the oxidation processes (Cui, 2018). The subsequent illustration is an effective spatially anisotropy charged isolation technique for acknowledging the benefit of morphological controlling on g-C_3N_4 (Liu, 2017). Using an NH_4Br based intermediate-mediated technique, the researchers generated the numerous phenomena (porous/microporous/ultraportable/horn-like) incorporated g-C_3N_4 tubes (Fig. 27a–d) (Liu, 2017). The g-C_3N_4 tubes possessed larger surface area and aided electron transport, carrier concentrations and interface charge transport performance, therefore exhibiting an exceptional photocatalytic performance for H_2 generation with an AQE of 14.3 percent at 420 nm (Fig. 27e, f). As seen in Fig. 27g, the selected photo-deposition findings reveal that the photoinduced electrons transfer to the external layer and holes might preferred to migrate onto the interior layer of the g-C_3N_4 tubes, offering a deep understanding into charges transport dynamics and increased photo performance.

Owing to rising technical emphasis on attaining "ecofriendly" power conservation and, continued endeavors was already made to the WS reaction for the research of a conceptual modeling on g-C_3N_4 catalysts. Besides novel nanomaterial g-C_3N_4, metal and non-metal loading, deficiencies variations construction, noble metal coating etc. for boosting the WS performance were also thoroughly published and evaluated in the preceding (Xiao, 2015). Although, it is also tough and prospective to generate completely employment of non-metallic g-C_3N_4 as an OWS photocatalysts. Acquiring a profound acknowledgement of the chemistry underlying the association among water molecules and g-C_3N_4, since the photocatalytic WS reaction is an essential part to alleviate the aforementioned problem. Yu et. al. (Tian, 2017) demonstrated that the lower dimensional charge transfer and electron mediated by interfacial hydroxylation might increase the

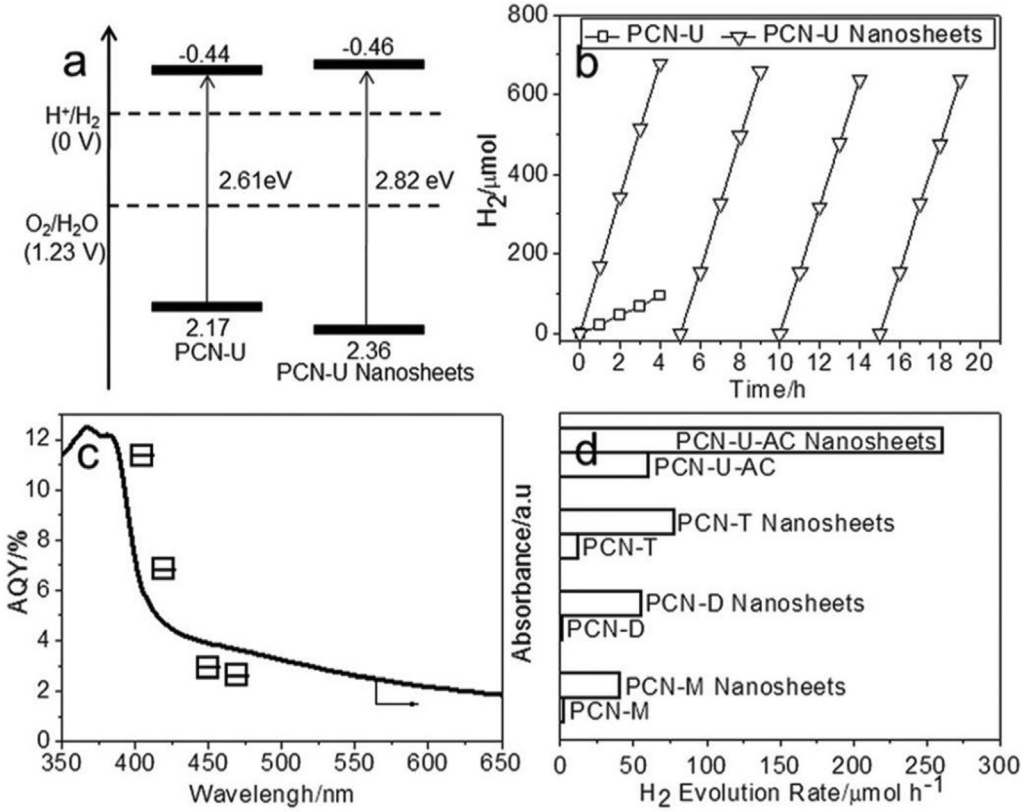

Fig. 26 (a) Graphical depiction of the electronic framework. (b) Photocatalytic performance and durability of the PCN-U and PCN-U nanostructure. (c) Wavelength dependent of AQE on the H_2 development in the PCN-U nanostructure. (d) Photocatalytic H_2 production kinetics of the PCN and PCN nanostructure produced from various intermediates. Reprinted with permission from Yang (2017). Copyright © 2017, John Wiley and Sons.

photocatalytic H_2 evolution of g-C_3N_4. The plentiful interfacial hydroxyls (—OH) inserted on the —C≡N location, therefore enlarge the 2D coupling charged particle mechanism of g-C_3N_4 to 3D space to recognize multiple scales electron transport, and radicalize the adjacent N unit (C—N═C) to encourage the electron (H^+) adsorbent and stimulation on them (Fig. 28). Incorporation of fundamental ammonium salts offers a pH-dependent hydroxylation-level mechanism and produces a ~11-time boost in H_2 productivity. These finding might alter a potential route for producing extremely active HER composites basis on surface polarization of ligands.

Many single compounds based photocatalysts for HER have weak photocatalytic activity under visible light. Moreover, combining the g-C_3N_4 with hole scavenger and metal, resulting into higher photocatalytic activity. Shubin et. al. (Niu, 2012) used thermal exfoliation approach, in order to synthesize the g-C_3N_4 nanosheets with outstanding HER in a triethanolamine/water solution, compared to bulk g-C_3N_4 with a thickness of 2 nm HER rates of 3 and 5.5 under visible and UV–vis, respectively. The activity of one layer g-C_3N_4 nanosheets for HER is better than that of bulk g-C_3N_4, which is being synthesized by exfoliation method (Alivisatos, 1996) due to better charge transport and separation. The mesoporous g-C_3N_4 thin films synthesized by the solvothermal method have an outstanding photocatalytic activity for HER (Zhang, 2013) about 8510 mol/h^1 g^1 (with a quantum efficiency of 5%, 420 nm), greater than the 1560 mol/h^1 g^1, which was observed for 2D non-porous g-C_3N_4 nanoparticles or the 350 mol/h^1 g^1, observed for bulk g-C_3N_4. The platinum (Pt) nanoparticles loaded with g-C_3N_4 nanorods with TEOA and 1% wt Pt co-catalyst (Yang, 2013). These materials also outperform their mesoporous counterparts (Pan, 2012). Even though the reason for this difference is unknown, and Jones et. al. suggested lone pairs in nitrogen are the reason for excellent performance (Tian, 2014). The TEOA is mainly used as a hole scavenger for g-C_3N_4 and gives methanol as an extra performance (a 14-fold rate boost). When TEOA is used instead of methanol (as hole scavenger), the P25 gives excellent performance for HER, but less than g-C_3N_4. The g-C_3N_4 nanomaterials synthesized by the rolling up method show perfect HER (Weng, 2014). When used with TEOA (as sacrificial agent) and Pt as co-catalyst, the g-C_3N_4 nanosheets or QDs as a catalyst give three times better performance than pristine g-C_3N_4. The band structure g-C_3N_4 QDs could be altered in order to make them more sensitive for visible and near-infrared light, allowing for even greater photocatalytic HER. Other metal-free g-C_3N_4 nanosheets have photocatalytic HER of 1596 mmol/h^1 g^1 (quantum efficiency 3.56% at 420 nm), while P-doped g-C_3N_4 nanosheets have photocatalytic HER of 1596 mmol/h^1 g^1 (quantum efficiency of 3.56%). Similarly, the WS reaction was done with 3D g-C_3N_4 nanoporous material, TEOA, and 3% wt Pt as co-catalyst (Bai, 2013) that gives

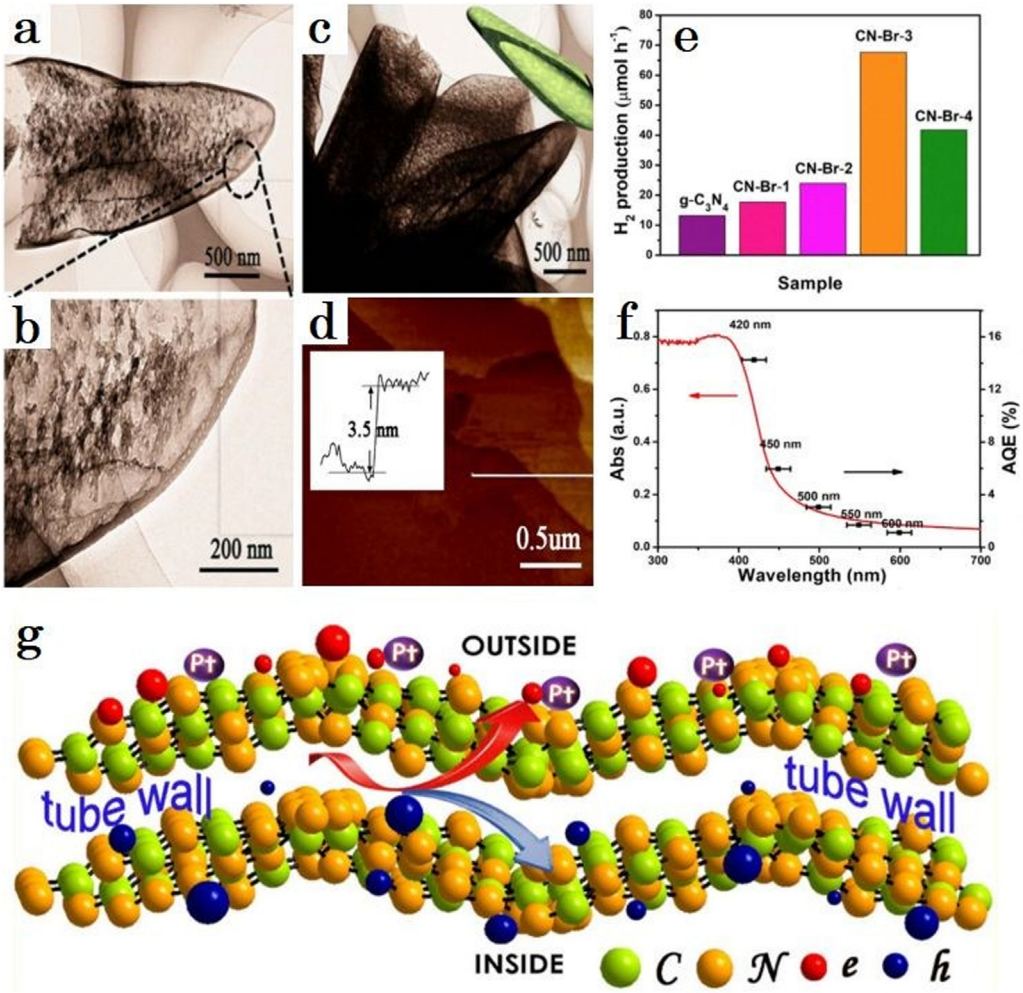

Fig. 27 (a, b) The enlarged TEM pictures of a singular g-C_3N_4 tube. (c) TEM pictures of CN-Br-3, (d) AFM imaging and diameter of g-C_3N_4 tubes shell. (e) the estimated rate ratios for HER of pristine g-C_3N_4 and CN-Br-X. (f) AQE and DRS spectra of CN-Br-3. (g) Graphical representation for the peculiar spatially charges isolation of g-C_3N_4 tubes in the photocatalytic reaction. Reprinted with permission from Liu (2017). Copyright © 2017, Elsevier.

2.5 times better HER than pristine g-C_3N_4 and remains stable after five cycles under visible light. The hollow g-C_3N_4 having a quantum efficiency of 7.5 %, has also been significant photoactivity for WS (Zhang, 2001). The inclusion of a MoS_2 co-catalyst considerably improved HER over hollow g-C_3N_4 spheres, forming a MOS_2/g-C_3N_4 hybrid (Fig. 29), thereby, increasing its light absorption and charge transfer ability (Zheng, 2016).

In order to broaden the spectrum range of g-C_3N_4, other semiconductors and metal nanoparticles have been added, which further induce surface plasmon resonance. In such heterojunction materials, the photoexcited charge carriers are better segregated, reducing charge recombination and loss of energy for fluorescence (Li et al., 2012; Zeng, 2018; Ajmal, 2020). The metal doped g-C_3N_4 has several benefits, including high diffusion of molecules, better light absorption, and more active sites (Tahir, 2014; Wang, 2014; Tahir, 2013). For creating TiO_2/g-C_3N_4 composite, the melamine was used for hydrothermal calcination, followed by solid-state reaction (Zeng, 2014). When compared the pristine g-C_3N_4 (108 mol/h^1 g^1) with TiO_2/g-C_3N_4 heterostructures, the TiO_2/g-C_3N_4 had low band gap and high photoactivity (556 mol/h^1 g^1) for HER under visible-light irradiation (130 mol/h^1 g^1). The core/shell heterojunction nanocomposites were found to be more beneficial, because of the high facial contact between core and shell components (Yuan, 2014). The core/shell nanowires of CdS/g-C_3N_4 with different g-C_3N_4 content were synthesized using the solvothermal and chemisorption method (Fig. 30) (Zhang, 2013). The g-C_3N_4 has absorbed on CdS nanowires by giving an excellent HER rate of 4152 mol/h^1 g^1 for 2 wt% g-C_3N_4. A one-step self-assembly approach for the synthesis of the core/shell nanomaterial of carbon spheres coated with g-C_3N_4 has recently been devised. These composites exhibit better light absorption, mechanical stability, and charge transfer conductivity (Weiss, 2017), resulting into maximum HER rates of 129 mol/h^1, an 8-fold excellent over new g-C_3N_4 (16 mol/h^1). Other nanocomposites of g-C_3N_4 (Gu, 2015; Zhang, 2014; Zheng, 2016; Fattakhova-Rohlfing et al., 2014; Cheng, 2017; Nguyen et al., 2015; Sun, 2012; Zheng, 2015; Jun 2013; Hong, 2014; Han, 2016; Lang et al., 2014; Zhang et al., 2015; Ye, 2015; Zheng, 2012; Maeda, 2011; Ahmad, 2015; Xu, 2013; Bandyopadhyay, 2017; Ran, 2015; Di, 2010;

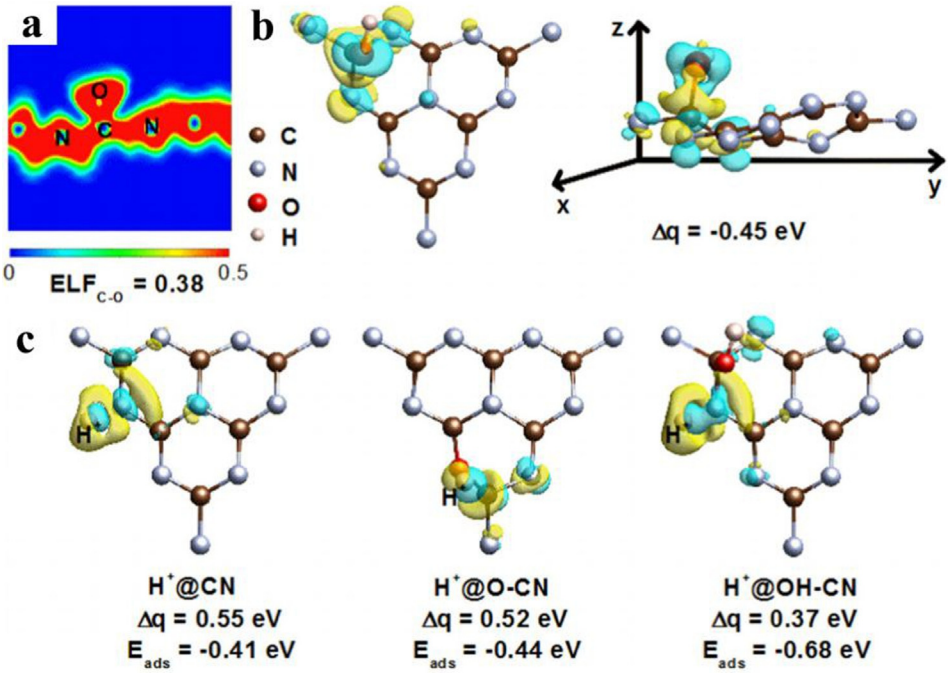

Fig. 28 (a) Interactive localized functions, (b) charged variation at upper aspect and side angle; (c) charged variation of protons deposited on CN, O-CN. Charging production is in blue and dissipation in yellow. E_{ads} and Δq represents for the absorbance and carrying charges for protons. Reprinted with permission from Tian (2017). Copyright © 2019, Royal Society of Chemistry.

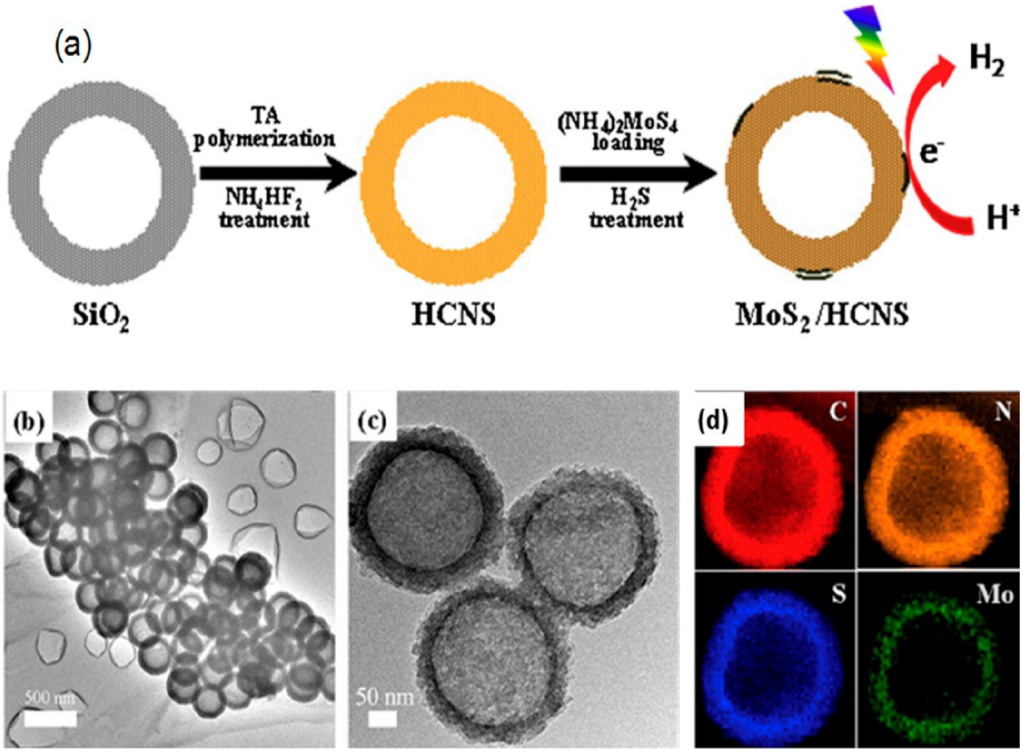

Fig. 29 (a) Synthetic strategy and (b, c) TEM images and (d) Energy dispersive X-ray spectroscopy (EDX) elemental maps of MoS_2@hollow g-C_3N_4. Reprinted with permission from Zheng (2016). Copyright © 2016, Elsevier.

Ajmal, 2018) were studied using a variety of materials and morphologies in order to get a deeper insight into the possible charge transfer pathways between g-C_3N_4 and other materials. Examples of different g-C_3N_4 heterojunctions include Z-scheme heterojunction (Ou, 2017; Wang, 2017), the Type II (Shen, 2017), p-n type (Zhang, 2013; Zhang, 2017; Ge, 2012;

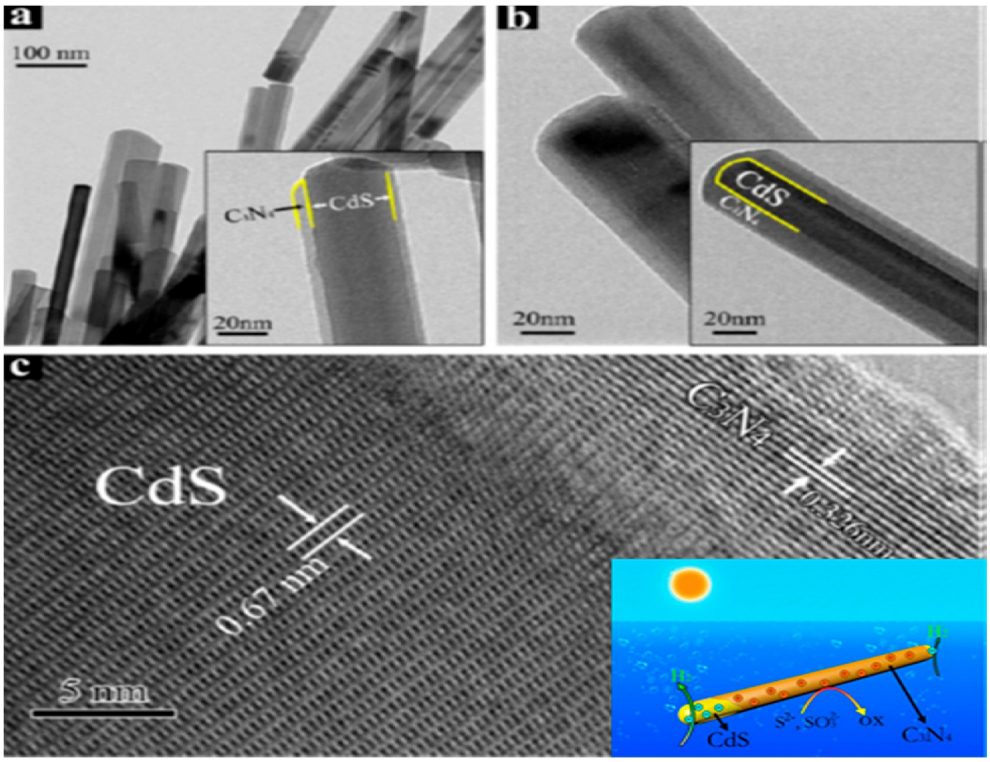

Fig. 30 (a, b) TEM and (c) HR TEM image of core–shell CdS/g-C_3N_4 heterojunction nanocomposite. Reprinted with permission from Zhang (2013). Copyright © 2013, American Chemical Society.

Xiang et al., 2011; Sun, 2017; Fang, 2017; Naseri, 2017; Lu, 2017; Xu, 2017; Zeng, 2017; Mao, 2017; Yu, 2017; Wen, 2017; Zhao, 2017; Barrio et al., 2018; Jin, 2017; Pramoda, 2017), g-C_3N_4 with metal (Ye, 2016; Xu, 2015) and g-C_3N_4 with carbon (Yuan, 2013). Controlling the structure of g-C_3N_4 heterojunctions for better light absorption is an interesting strategy in recent times.

3.2. Carbon dioxide (CO_2) reduction

The ongoing use of fossil fuels for chemical and energy production is causing severe problems (Tong, 2015; Martin, 2014). Among them, the photocatalytic CO_2 reduction to sustainable hydrocarbons and oxygenates might be a long-term solution. Because CO_2 reduction includes the multi-electron transfer, methanol, methane, formaldehyde, formic acid, and carbon monoxide formation kinetics are much slower than H_2 formation kinetics. The CO_2 reduction involves the molecule absorption onto the catalyst surface, where photoexcited electrons are transported across the semiconductor bandgap to form the anion radical. In an aqueous environment, the CO_2 reduction is caused by photoexcited holes transferred to hydrogen atoms from water, and then the proton is shifted to the CO_2 anion (Fig. 31) (Tian, 2019). The CO_2 reduction gives various products, which are shown below (relative to NHE at pH = 7):

$$CO_2 + e^- \rightarrow CO_2^{\cdot-} + O_2 \; E^\circ = -1.90\ eV \quad (4)$$

$$CO_2 + H^+ + 2e^- \rightarrow HCO_2^{\cdot-} \; E^\circ = -0.49\ eV \quad (5)$$

$$CO_2 + 2H^+ + 2e^- \rightarrow CO + H_2O \; E^\circ = -0.53\ eV \quad (6)$$

$$CO_2 + 4H^+ + 4e^- \rightarrow HCHO + H_2O \; E^\circ = -0.48\ eV \quad (7)$$

$$CO_2 + 6H^+ + 6e^- \rightarrow CH_3OH + H_2O \; E^\circ = -0.38\ eV \quad (8)$$

$$CO_2 + 8H^+ + 8e^- \rightarrow CH_4 + 2H_2O \; E^\circ = -0.24\ eV \quad (9)$$

$$CO_2 + 10H^+ + 10e^- \rightarrow C_2H_4 + 4H_2O \; E^\circ = -0.22\ eV \quad (10)$$

$$CO_2 + 12H^+ + 12e^- \rightarrow C_2H_5OH + 3H_2O \; E^\circ = -0.33\ eV \quad (11)$$

The essential features of photocatalyst, CO_2 absorption capacity, and strength are the main factors in the photocatalytic CO_2 reduction process (Gu, 2015). Electron and hole transfer kinetics to CO_2, charge separation, bandgap, and reductant are essential for photocatalytic CO_2 reduction process. g-C_3N_4 material has been studied for CO_2 reduction due to their negative CB, stability, and low bandgap (Li et al., 2015; Liang, 2015). The g-C_3N_4 activity is enhanced by doping of metal and nonmetal, heterojunction construction, and Z scheme hybrid (Han, 2015; Zhu et al., 2015; Huang, 2015; Wu, 2014; Han, 2015; Ajmal et al., 2021). Pengfei et. al. (Li, 2015) used ultrathin sheets of g-C_3N_4 for excellent CO_2 reduction, which gives tremendous charge carrier potential, greater surface area for absorption, and improved light absorption with methane and methanol productivities of 1.39 and 1.87 mol/h^1 g^1, respectively. According to Jianguo and colleagues (Wu, 2014), the decline in overpotential of CO_2 is due to the better charge separation of Pt nanoparticles on metal/

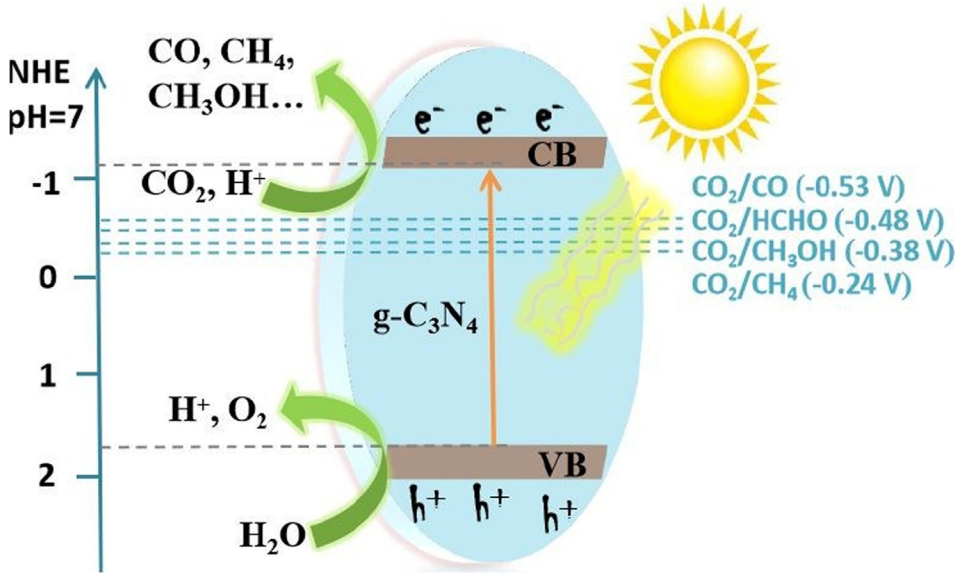

Fig. 31 Graphical depiction of photocatalytic conversion of CO_2 to fossil energy under photoexcitation upon pure g-C_3N_4. Reprinted with permission from Tian (2019). Copyright © 2019, Royal Society of Chemistry.

semiconductor surface area. According to Qingqing et. al. (Wang, 2013) the Pd nanoparticles with double defect increase the reduction of CO_2 into CH_4 and carbon monoxide (CO) over g-C_3N_4 nanosheets. The 61.4 % conversion of CO_2 achieved and average CO production was 4.3 mol/g^1 h^1, with an average methane (CH_4) production rate of 0.45 mol/g^1 h^1, which showed reactive CO_2 and many active sites. The g-C_3N_4 nanotubes doped with oxygen synthesized by thermal oxidation and condensation of pristine g-C_3N_4, were demonstrated to have considerable photocatalytic CO_2 reduction capability under visible light (Zhang, 2012). The oxygen-doped g-C_3N_4 nanotubes have multi-walled tubes and have a diameter of 30 nm, and give methanol at the rate of 0.88 mol/g^1 h^1, which is five times greater than individual g-C_3N_4 nanotubes (0.17 mol/g^1 h^1). The ZnO/g-C_3N_4 heterojunction was synthesized by one-step calcination (Sui, 2013). The bulk g-C_3N_4 demonstrate 2.5-fold performance due to a direct Z-scheme mechanism indicating robust transportation of electrons from g-C_3N_4 towards ZnO surface. Zhong Xing et. al. showed that modified g-C_3N_4 with CeO_2 representing an excellent photocatalytic activity for CO_2 reduction to CH_4, with an average production rate of 4.79 mmol/g^1 h^1, which is 3 times greater than g-C_3N_4. Wang et. al. did a situ redox reaction between $MnSO_4$ and $KMnO_4$ and then synthesized a 2D/2D-MnO_2/g-C_3N_4 heterojunction photocatalyst for CO_2 reduction to CO (9.6 mmol/g^1), which gives excellent charge separation. The g-C_3N_4/SnS_2 was used for photocatalytic CO_2 reduction in which SnS_2 electrons interact with holes of g-C_3N_4 to give CH_3OH (2.3 mol/g^1) and CH_4 (2.3 mol/g^1), respectively. A unique Z scheme method was used in MoO_3/g-C_3N_4 heterojunction (Liu, 2015). TRyo et. al. used a different method in which they connected Ru(biby) complex into the structure of g-C_3N_4, which enhanced the performance of the reduction of CO_2 to formic acid, having an average quantum yield of 5.7% at 400 nm (Fig. 32) (Kuriki, 2015). The active photocatalysts for CO_2 reduction are generated, when polyoxometalate clusters are attached to g-C_3N4

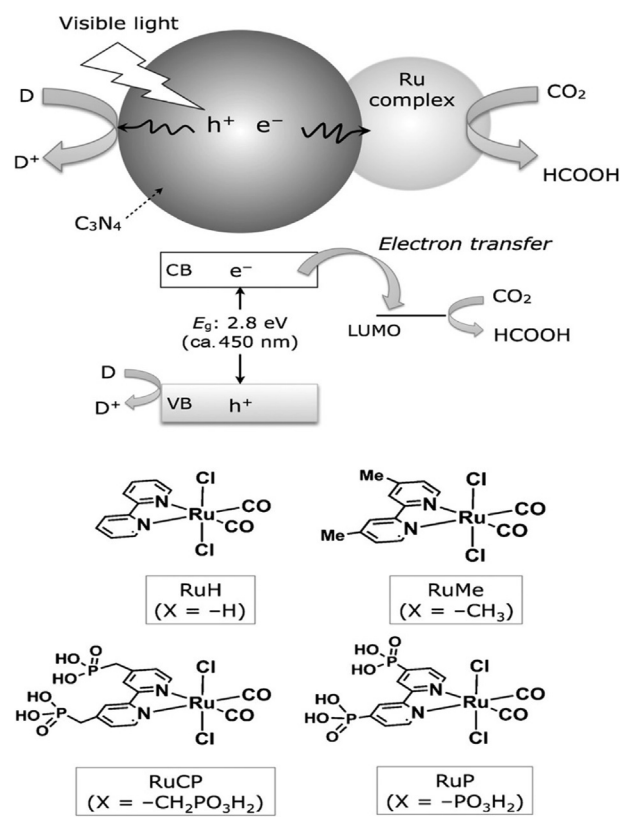

Fig. 32 The photocatalytic reduction of CO_2 via Ru complexes structure and Ru complex/C_3N_4 hybrid photocatalyst. Reprinted with permission from Kuriki (2015)). Copyright © 2015, John Wiley and Sons.

(Zhang et al., 2015). After 10 h of visible light irradiation, the Co_4/g-C_3N_4 hybrid photocatalyst produced 107 mol/g^1 h^1 of CO and 94% selectivity for CO, significantly exceeding unpromoted g-C_3N_4.

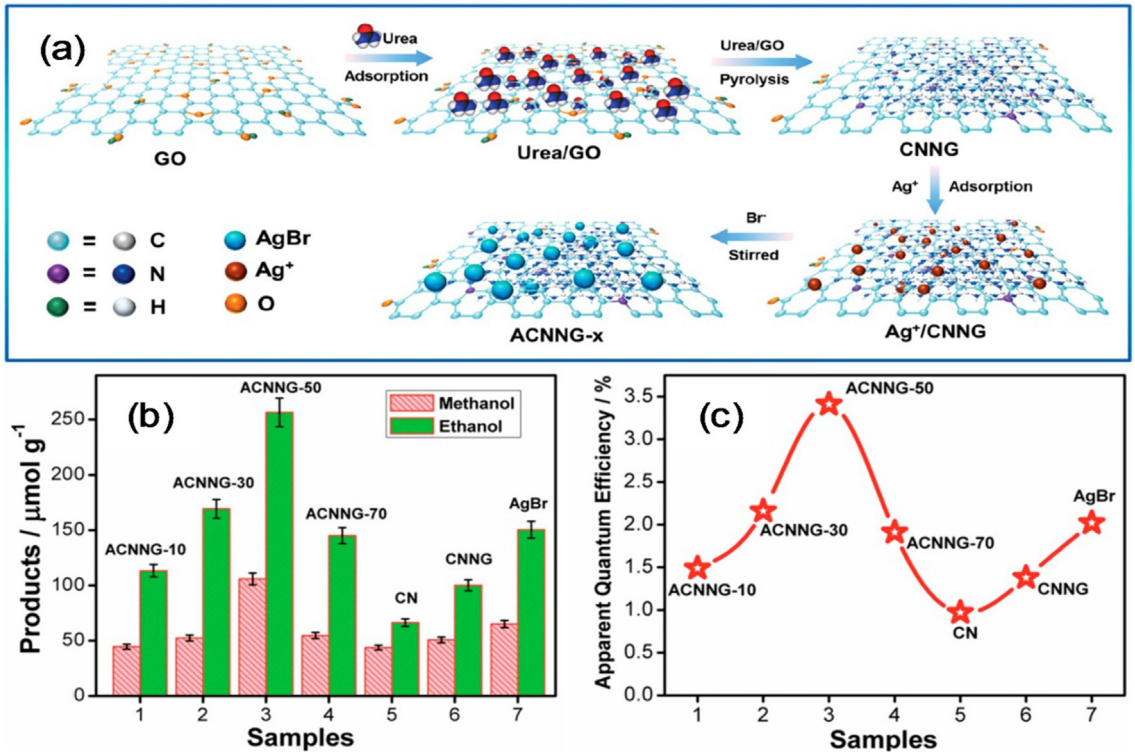

Fig. 33 (a) Synthetic strategy, and (b, c) photocatalytic performance for CO_2 reduction of intercorrelate super hybrid g-C_3N_4 nanocomposites under visible light and corresponding apparent quantum efficiencies. Reprinted with permission from Li (2015). Copyright © 2015, John Wiley and Sons.

An intercorrelated super hybrid formed of g-C_3N_4 with AgBr ornamented onto N-doped graphene (produced by chemical synthesis) was also employed to show photocatalytic CO_2 reduction to CH_3OH and C_2H_5OH (Fig. 33) (Li, 2015). Using Cu/TiO_2/g-C_3N4 (Cao, 2013), nanocomposites fabricated by impregnation and pyrolysis, the Oluwatobi et. al. demonstrated an increased rate of photo-reduction of CO_2 to CH_3OH and HCOOH under UV–vis radiation, with peak rates of CH_3OH at 2574 and HCOOH at 5069 mmol/g^1, respectively. The increased performance was attributed to the nanocomposite photoexcited electrons distribution and metal position. The Hailong et. al. demonstrated that AG/TiO_2/g-C_3N_4 heterojunction has excellent performance toward CO (28 mol/g^1) and CH_4 (19 mol/g^1) production from CO_2 reduction. However, depending upon lower Fermi level, the photoexcited electrons were transferred towards the TiO_2/g-C_3N_4 homojunction and then after TiO_2 to Ag nanoparticles, thereby, resulting into a significant reduction in electron-hole recombination onto the TiO_2 surface-modified Ag nanoparticles.

Yu et. al. (Fu, 2017) developed hierarchy permeable O incorporated g-C_3N_4 nanotubes (OCN-Tube) via serial heat oxidizing exfoliating and curling-condensation of pristine g-C_3N_4. The OCN-Tubes composed of interconnecting multi-walled nanotube with consistent sizes of 20–30 nm. Upon light irradiation, the photocatalytic methanol generation ratio of OCN-Tubes is 0.88 μmol/g^1 h^1, that is 5-fold greater that of pure g-C_3N_4 (0.17 μmol/g^1 h^1) (Fig. 34a). The improved photocatalytic performance of OCN-Tube is attributed to the synergism impact of hierarchy nanotube configuration and O coupled interaction. The hierarchy nanotubes design imbues OCN-Tube, increased particular surface area, increased light usage reliability, and enhanced mobility dynamics, owing to the numerous exposure energetic sides and various illumination dispersion pathways. Furthermore, the integration of O improves the electronic structure of g-C_3N_4, leading in a smaller absorption edge, stronger CO_2 affinities and an improved isolation of photoinduced electrons transportation. As demonstrated in Fig. 34b, whenever 13CO_2 was employed as the fuel, a significant pattern with the m/z value of 29 ascribed to 13CO was found (Ou, 2018). Consequently, it is established that CO is contributed from CO_2 in the photocatalytic reaction.

Qin et. al. employed barbituric acid (BA) integrated g-C_3N_4 for the reduction of CO_2 to CO and H_2 as a biproduct (Qin, 2015). Despite alleviating the physical/chemical parameters of g-C_3N_4 with improved photostability, the molecular doping of urea and barbituric acid considerably simplified the charged transfer and isolation through the creation of interfacial chemical heterostructures. As demonstrated in Fig. 35a, the optimum CNU-$BA_{0.03}$ displayed a substantially improved photocatalytic CO generation, surpassing 15 times (31.1 μmol/h^1) more pristine g-C_3N_4 (2.1 μmol/h^1). Furthermore, high loading of BA resulted to the reduction in the CO generation ratio, that was ascribed to the degradation of g-C_3N_4 polymer structure due to BA monomer. It obviously illustrates the necessity of specific handling of the level of copolymerization in boosting the photoreduction performance. Furthermore, the tendency of the materials such as CO and H_2 coincided effectively with the light absorbance of CNU-$BA_{0.03}$ predicated on the reaction spectra (Fig. 35b) and also

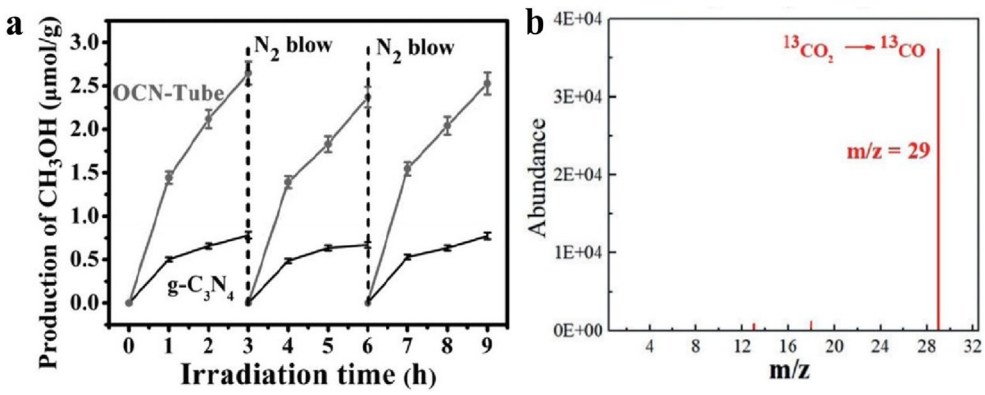

Fig. 34 (a) Time trends of photocatalytic performance for CH_3OH generation over pure g-C_3N_4 and O/CN Tubes (Fu, 2017). (b) GC–MS data of 13CO generated over 20 CPB-PCN from $13CO_2$ isotopes analysis. Reprinted with permission from Ou (2018). Copyright © 2018, John Wiley and Sons.

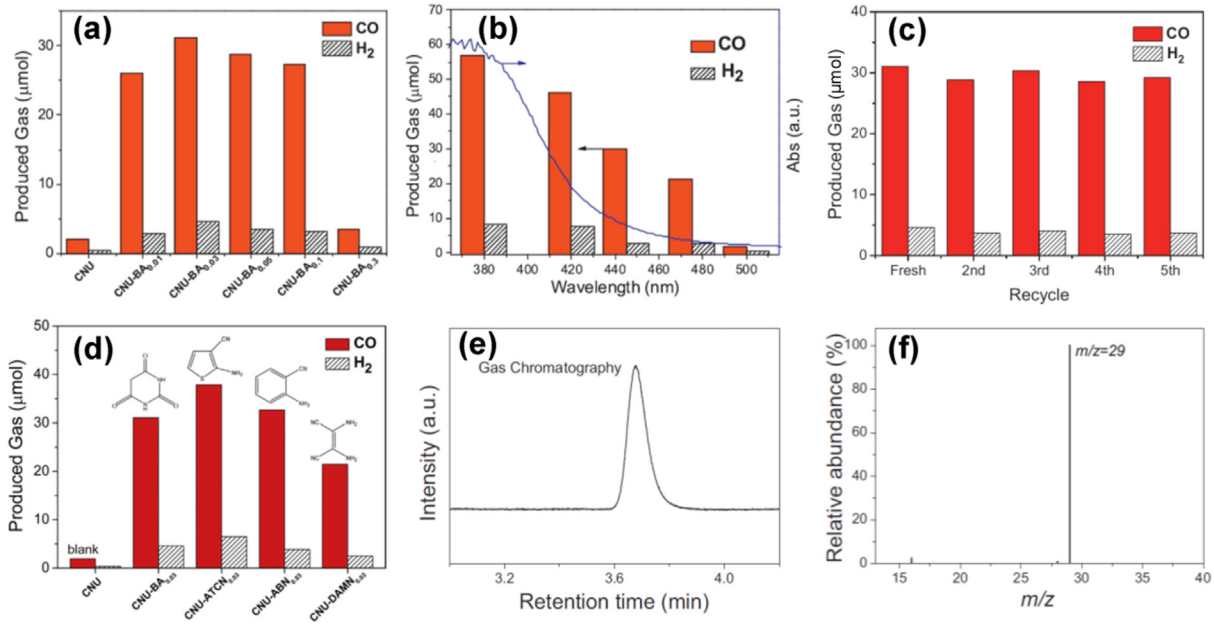

Fig. 35 (a) Production of CO and H_2 from the photocatalytic CO_2 reduction employing CNU-BA_x with varying quantities of barbituric acid embedded g-C_3N_4. (b) Wavelength based production photocatalytic CO_2 reduction. (c) Durability analysis of the generation of CO and H_2 ove CNU-$BA_{0.03}$ material. (d) Influence of several monomers integrated g-C_3N_4 on the synthesis of CO and H_2 under illumination. (e–f) GC–MS findings of the produced CO from the reduction reaction of $13CO_2$ over the CNU-$BA_{0.03}$ material. Reprinted with permission from Qin (2015). Copyright © 2015, Elsevier.

the material held a good reliability with no declination in the final products (Fig. 35c). To extensively reveal the involvement of molecular doping process, various monomers comprising ABN, ATCN and DAMN were also applied to combine with urea raw material. Surprisingly, an elevated photocatalytic efficiency in all comonomer integrated g-C_3N_4 materials was detected contrasted with the simple g-C_3N_4 (Fig. 35d). This signifies those plentiful options of organic monomers may be merged with g-C_3N_4 using the co-polymerization approach to boost the reduction reaction of CO_2 source. To validate the formation of CO from the CO_2 photoreduction, a 13C tagged isotopic tracing assay utilizing $13CO_2$ was demonstrated (Fig. 35e–f). Depending on the MS data, a fundamental signal pertaining to the 13CO (m/z value of 29) was depicted rather than 12CO (m/z value of 28). It contended the generation of CO exclusively resulted from the photocatalytic CO_2 reduction instead of the breakdown of carbon contaminants from the surface of photocatalysts.

The integration of metals with g-C_3N_4 is also an intriguing technique for the creation of noble metal-based g-C_3N_4 heterostructure materials for efficient CO_2 reduction to sustainable compounds. Lately, a researcher team has showed an improved conversion of CO_2 to CH_4 using Pt integrated g-C_3N_4 composites, that has been synthesized via a chemical reduction technique in the solvent of ethylene glycol (Ong, 2014). This research enabled the photocatalytic reaction extra competitively possible and operationally practicable by employing a low-power of 15 W energy-saving daylight bulb

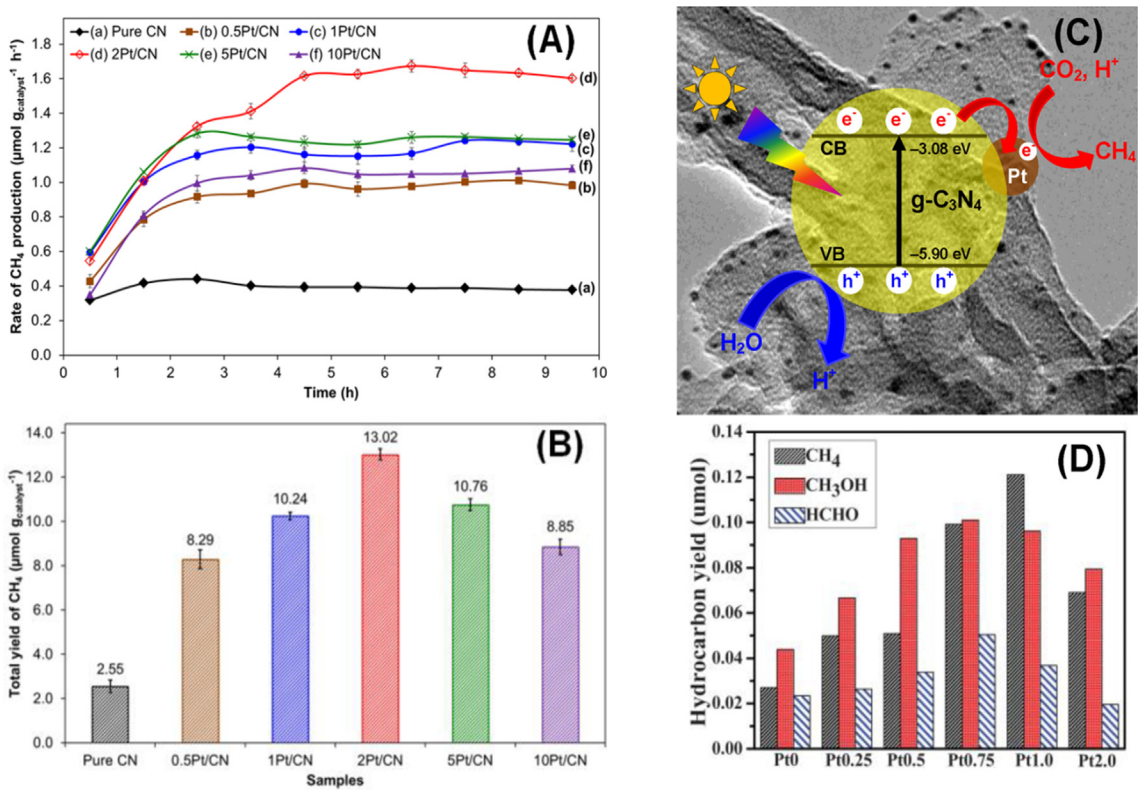

Fig. 36 (A) Photoreduction time function, (B) overall CH_4 output over g-C_3N_4 and Pt/g-C_3N_4 catalysts for 10 h of operation. (C) Charge transport process for CO_2 reduction using H_2O to CH_4 using Pt/g-C_3N_4 composite. Reprinted with permission from Ong (2014). (D) Output rate of hydrocarbons with regard to various integration of Pt (0–2.0 wt%) coated on the g-C_3N_4 nanostructure under visible light for 4 h of operation. Reprinted with permission from Ref. (Yu, 2014). Copyright © 2015, ROYAL SOCIETY OF CHEMISTRY. Copyright © 2014, ROYAL SOCIETY OF CHEMISTRY.

as the illumination. As indicated in Fig. 36A–B, the photocatalytic CH_4 generation over the 2Pt/g-C_3N_4 with an ideal 2 wt % level of Pt can be obtained up to 13.02 μmol/g^1 after 10 h of solar illumination, that was 5.1 times larger than the pristine g-C_3N_4 (2.55 μmol/g^1). Therefore, the considerably enhanced photoactivity of Pt/g-C_3N_4 was attributed to the enhanced optical absorbance and remarkable surface electron transport from g-C_3N_4 to Pt owing to its reduced Fermi level to restrict the replication of electrons/hole pairs (Fig. 36C). Correspondingly to another prior report by Yu and team utilized Pt/g-C_3N_4 mixture photocatalysts for the reduction of CO_2 under visible illumination (Yu, 2014). With the ideal amount of Pt, CO_2 was decreased to potential hydrocarbon products, i.e., CH_4, CH_3OH and HCHO in the liquid–liquid interactions (Fig. 36D). Following the use of Pt, the alternating voltage was drastically lowered, thereby enabling the electron transport the photoreduction of CO_2. Table. 1 compares the performance of different g-C_3N_4 photocatalysts for photocatalytic CO_2 reduction and H_2 production.

3.3. Environmental remediation

Polluted water is being discharged into the aquatic environment by several large-scale petrochemical, textile, and food sectors (Yuan, 2015). The use of organic dyes are often is being oftently observed in the printing, textile, as well as photography sectors. A significant amount of such colors is released into the effluent wastewater streams during the dying process. These colors are toxic to people and animals even at low concentrations (Jiang, 2015; Yuan, et al., 2014). As a result, modern oxidation methods are being developed in order to treat the contaminated drinking water and wastewater containing hazardous or non-biodegradable compounds (Sridharan, 2015; Li, 2015). The photocatalysis via semiconductors (Hou, 2013; Wu, 2014; Wen, 2015; Pany and Parida, 2015), is regarded as a low-cost, high-efficiency technique towards efficient removal of refractory organic/inorganic compounds from wastewater. The procedure of photocatalytic degrading of contaminants during light treatment on g-C_3N_4 is depicted in Fig. 37 (Tian, 2019). The principal active components in photocatalytic ecosystem cleaning are photoexcited holes, which are effective oxidants in and of themselves or combine with water in order to form hydroxyl radicals ($^{\bullet}OH$), those are strong oxidants having oxidation potential about (2.8 eV). (NHE). Adsorbed pollutants on photocatalyst surfaces or in the solution can be attacked by reactively generated OH, causing them to mineralize as water and CO_2. The literature has broadly premeditated the organic pollutants photocatalytic oxidation in H_2O (Chen, 2015; Zhang, 2015; Kamat, 2007).

$$SC + h + hv \rightarrow SC \times (e^{-}_{CB} + h^{+}_{VB}) \quad (12)$$

$$hVB^{+} + H_2O \rightarrow {}^{\cdot}OH + H^{+} \quad (13)$$

Table 1 Photocatalytic H_2 production and CO_2 reduction over g-C_3N_4.

Serial No.	Photocatalysts	Co-Catalysts (Loading)	Experimental details	H_2/CO_2 productivity/ $\mu mol \cdot g^{-1} \cdot h^{-1}$	Enhancement Relative to Conventional g-C_3N_4	Refrences
1	g-C_3N_4 nanosheets	Pt (1 wt%)	10 vol% TEOA full sunlight and $\lambda > 400$ nm	1395	5.6	(Tong, 2015)
2	K-g-C_3N_4	Pt (0.5 wt%)	10 vol% TEOA 300 W Xe ($\lambda > 400$ nm	1028	14	(Wu, 2014)
3	AuPd/g-C_3N_4	Au and Pd	10 vol% TEOA 300 W Xe ($\lambda \geq 400$ nm)	326	3.5 1.6	(Han, 2015)
4	Cu_2O@g-C_3N_4 core@shell		10 vol% TEOA 300 W Xe	202.28	5.7	(Liu, 2015)
5	CdS/g-C_3N_4 core/shell	Pt (0.6 wt%)	0.35 M Na_2S and 0.25 M Na_2SO_3 300 W Xe ($\lambda \geq 420$ nm)	4152		(Ou, 2017)
6	MoS_2/g-C_3N_4	N/A	10 vol% TEOA, 300 W Xe ($\lambda > 400$ nm	252	8	(Zhao, 2015)
7	$CaIn_2S_4$/g-C_3N_4	Pt (1 wt%)	0.5 M Na_2S and 0.5 M Na_2SO_3 300 W Xe	102	3	(Jiang, 2015)
8	CdS nanorods/g-C_3N_4	NiS	10 vol% triethanolamine, 300 W Xe ($\lambda \geq 420$ nm)	2563	1.6	(Yuan, 2015)
9	AgQCs/g-C_3N_4	Pt (1 wt%)	25 vol% methanol simulator AM 1.5 G	5.59	1.7	(Sridharan, 2015)
10	Thiourea and urea derived g-C_3N_4		300 W Xe/420 nm, 40 mg catalysts	Urea derived g-C_3N_4 CO: 0.56, CH_3CHO: 0.44, CH_4: 0.04 thiourea derived g-C_3N_4 CO: 0.36, CH_3CHO: 0.26, CH_4 = 0.025	N/A	(Wang, 2016)
11	Melamine & urea derived g-C_3N_4		300 W Xe (420 nm), 0.2 g and 1.0 M NaOH solution (100 mL)	Urea derived g-C_3N_4 CH_3OH: 6.28, C_2H_5OH: 4.51, O_2: 21.33 melamine derived g-C_3N_4 CH_3OH: TRACE, C_2H_5OH: 3.64, O2: 10.29	N/A	(Mao, 2013)
12	Sulfur-doped g-C_3N_4		300 W simulated solar Xe and 200 mL Pyrex reactor, 100 mg 1 wt% Pt co-catalyst, 0.12 g $NaHCO_3$ and 0.25 mL 4 M HCl solution	CH_3OH: 0.37	1.37	(Wang, 2015)
13	Pt-loaded g-C_3N_4		15 W energy-saving daylight bulb, flow rate of CO_2 fixed at 5 $mL \cdot min^{-1}$	CH_4: 1.3	5.2	(Ong, 2015)
14	Ag_3PO_4/g-C_3N_4		500 W Xe/420 nm, stainless-steel reactor 132 mL, 10 mg in 4 mL H_2O, 0.4 MPa CO2 at 80 °C	CO: 44, CH_3OH: 9, CH_4: 0.2, C_2H_5OH: 0.1	CO: 11	(He, 2015)
15	BiOI/g-C_3N_4		300 W Xe (400 nm), 0.10 g catalyst, CO_2 bubbled through water	CO: 3.58, O_2: 1.96, H_2: 0.4, CH_4: 0.2	CO: 17.9	(Wang, 2016)
16	CeO_2/g-C_3N_4		300 W Xe, reactor volume 500 mL, 50 mg catalyst, CO_2 bubbled through water	2 wt% CO: 11.8 and CH_4: 9.08 3 wt% CO: 10.16 and CH_4: 13.88	CH4: 69.4	(Li, 2016)
17	g-C_3N_4/$NaNbO_3$		300 W Xe, reaction volume 230 mL, 50 mg catalyst, reactor purged with CO_2, then 2 mL H_2O injected	CH_4: 6.4	8	(Shi, 2014)

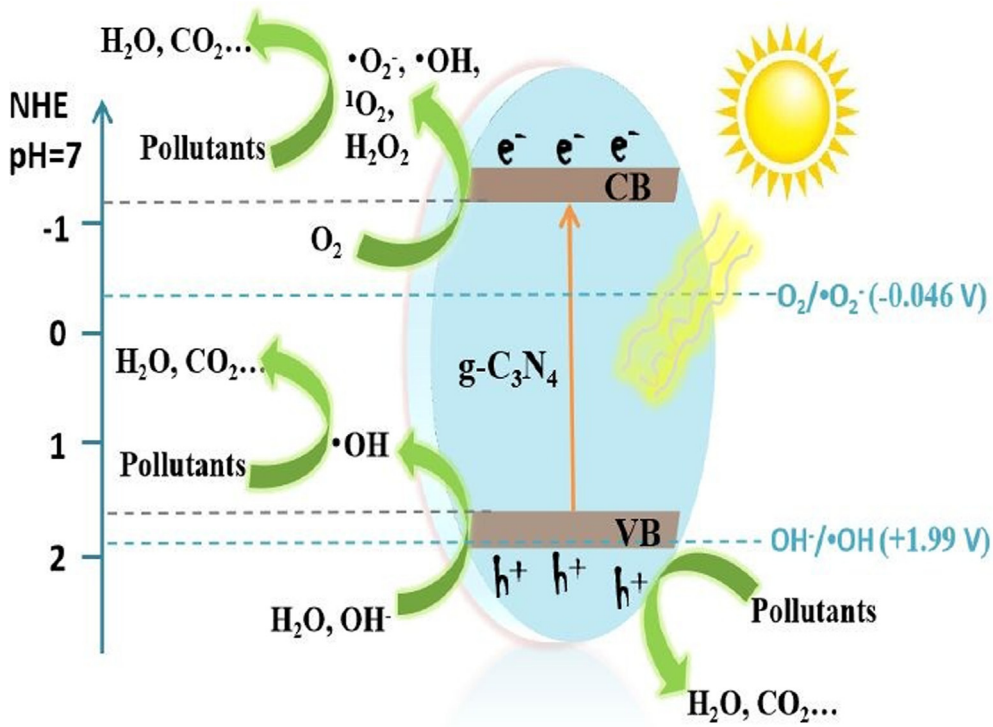

Fig. 37 Scheme of photocatalytic degrading of different contaminants under solar illumination employing pristine g-C_3N_4. Reprinted with permission from Tian (2019). Copyright © 2019, Royal Society of Chemistry.

$$O_2 + e^-_{CB} \rightarrow O_2^{\cdot -} \quad (14)$$

$$O_2^{\cdot -} + H^+ \rightarrow HO_2^{\cdot} \quad (15)$$

$$HO_2^{\cdot} + HO_2^{\cdot} \rightarrow H_2O_2 + O_2 \quad (16)$$

$$O_2^{\cdot} + HO_2^{\cdot} \rightarrow O_2 + HO_2^- \quad (17)$$

$$HO_2^- + H^+ \rightarrow H_2O_2 \quad (18)$$

$$H_2O_2 + hv \rightarrow 2\,^{\cdot}OH \quad (19)$$

$$H_2O_2 + O_2^{\cdot} \rightarrow {}^{\cdot}OH + OH^- + O_2 \quad (20)$$

$$H_2O_2 + e^-_{CB} \rightarrow {}^{\cdot}OH + OH^- \quad (21)$$

$$\text{Organic compund} + {}^{\cdot}OH + e^-_{CB} \rightarrow \text{Degradation products} \quad (22)$$

$$\text{Organic compund} + SC\ (h^+) \rightarrow \text{Degradation products} \quad (23)$$

$$\text{Organic compund} + SC\ (e^-) \rightarrow \text{Degradation products} \quad (24)$$

Mineralization causing oxidants have been related to a number of reactive species, including OH, HO_2, and H_2O_2, with $^{\bullet}OH$ being the most probable candidate as illustrated in Eq. (22). The 'photo-Kolbe reaction,' in which photoexcited holes oxidize carboxylic acids, which directly produce the CO_2, has also been shown. The VB and CB must be sited, so hydroxyl radicals E (NHE) and superoxide radicals E (NHE) oxidation and reduction potentials for semiconductor photocatalysts are well located within the band gap of materials. However, the requirement for photocatalysts thermodynamically dictate that the hydroxyl radicals E (NHE) and superoxide radicals E (NHE) oxidation and reduction potentials are well located within the band gap. To put it another way, holes must have a sufficiently positive redox potential to make $OH^{\bullet}$ radicals, whereas photoexcited electrons must have a sufficiently negative redox potential to generate $O_2^{\bullet}$. It has taken a long way to synthesize photocatalysts for water purification under the sunlight. The g-C_3N_4 materials physical properties are modified by doping some heteroatom and synthesizing heterojunction with the aim of increasing its surface area and porosity, thereby, making nanostructured based g-C_3N_4 as probable photo-catalysts for a wide variety of pollutants (Kumar, 2012; Yu et al., 2015). The ultrathin g-C_3N_4 nanosheets fabricated through methanol exfoliation from bulk g-C_3N_4 showed better photocatalytic activity towards methylene blue (MB) degradation (Kuriki, 2015). Under visible light, g-C_3N_4 nanotubes have a higher photoactivity towards MB degradation as compared to P25 or pristine g-C_3N4 (Walsh, 2016). Tahir and colleagues discovered that tubular g-C_3N_4 displayed improved stability and activity than bulk g-C_3N_4 towards photocatalytic MB degradation and methyl orange (MO) under visible light due to larger surface area of (182 m^2/g^1), more excellent light absorption, and efficient separation/transfer of charges (Yu, 2014). Under visible light (>420 nm) and imitation sun light (>290 nm), one-dimensional g-C_3N_4 nanorods of varied ratios were studied for MB degradation (Gao, 2016). The g-C_3N_4 nanorods had 1.5–2.0 times greater photocatalytic activity and photocurrent responsiveness of g-C_3N_4 nanoplates. Aother effective but a facile chemical approach was employed in order to synthesize

the nanofiber-like g-C_3N_4, which showed a probable photodegradation performance during Rhodamine B (RhB) degradation (Wang, 2015). One typical technique in order to drive the photo-generated charge carriers is the use of g-C_3N_4 doping to increase spectrum utilization and band alignment. In environmental pollution applications, metals like Fe and Cu (Fu, 2017; Mao, 2013; Shi, 2014), non-metal such as C, B, S or O (He, 2015; Li, 2015; Lin et al., 2014; Xia, 2017; Han, 2017), and Co doping (Wang, 2017; Di, 2017; Feng, 2017) all have been used. For the comparison purpose, with primeval g-C_3N_4 nanosheet, the O and S co-doped g-C_3N_4 were synthesized via melamine polymerization process followed by H_2O_2 activation subsequent to the functionalization of trithiocyanuric acid (Fig. 38a) which brought about the significant increased in the photo-catalytic degrading of RhB (Fig. 38b) up to 6-fold (You, 2017). It is due to the incremental increase in the total number of surface active sites, possibly leads to the enhanced separation and ultimate transfer of photo-generated electrons and holes, which in turn results into the high degree of delocalization in the HOMO and LUMO.

Similarly, a popular antibiotic photocatalytic degradation namely tetracycline chloride, whose uncontrolled release cause problem was examined (Li, 2017; Brini, 2021; Brini, 2021). The process containing the photodeposition of (7–15) nm of (Au and Pt) nanoparticles over g-C_3N_4 surface sites are good examples. The surface plasmon resonance of Au increases the optical adsorption range, but Pt sinks the photoexcited electrons. The multicomponent heterostructures like Ag_3PO_4/g-C_3N_4 for MO degradation (Huang, 2015; Niu, 2014) are viable for environmental pollution (Wang, 2016; Ong, 2015; Ni, 2016; Huang, 2015; Essekri, 2021). The coupling of g-C_3N_4 and metals provide adjustable heterojunctions with excellent charge transfer than typical nanocomposites (Wang, 2016; Li, 2016; Raziq, 2017; Maeda, 2014; Ong, 2016; Zhang, 2016; Wang, 2016), and multicomponent heterostructures like Ag_3PO_4/g-C_3N_4 systems for MO degradation (Ong, 2015; Zhou, 2014; Wu, 2017). The composite such as Ag_3PO_4/g-C_3N_4 core–shell converted MB at a rate of 97% in 30 min, compared to 79% Ag_3PO_4 and g-C_3N_4 components physical mixture and 69% untainted Ag_3PO_4. Actually, the g-C_3N_4 shell may make the composite more stable by preventing Ag_3PO_4 from dissolving. The core–shell g-C_3N_4@TiO_2 were seven times more photoactive than pristine g-C_3N_4/TiO_2, which was prepared via in situ sol–gel re-assembly pathway and then utilized to remove phenol during light source. Photo-degradation rate constant was fund to be enhanced from (0.0018–0.0386 h^1) by increasing the thickness of g-C_3N_4 shell from (0 to 1 nm). However the bigger shells impeded transport of charge towards external surface of photocatalyst, and ultimately decreasing the overall performance. A simple, environmentally friendly, and low-cost ultrasonic dispersion approach was used in order to efficiently construct a Z-scheme N-doped g-C_3N_4/ZnO core–shell nanomaterials (Fig. 39a, b). The thickness of the g-C_3N_4 shell can be adjusted with g-C_3N_4. A novel energy level was generated into the N-doped ZnO band gap by creating straight interaction between g-C_3N_4 shell and N-doped ZnO core by significantly reducing it. Therefore, these such kind of composite based core–shell demonstrated a considerably higher visible-light photocatalytic efficiency towards RhB deterioration than simple g-C_3N_4 and N-doped ZnO counterparts (Fig. 39a, c) (Kumar, 2014). Magnetically detachable g-C_3N_4/Fe_3O_4 hybrid composite were made via simple, repeatable, template-free synthesis (Fig. 39b, a) (Kumar, 2014). The mono-dispersed Fe_3O_4 nanoparticles with an (8 nm) diameter were consistently produced on g-C_3N_4 sheets, displaying better charge separation and photocatalytic performance for RhB degradation (Fig. 39b, c). After six recycles, the photocatalytic activity of these g-C_3N_4/Fe_3O_4 nanocomposites remained unchanged, permitting magnetic catalyst recovery (Fig. 39b, d) (Kumar, 2013). The Xiao et. al. demonstrated that during organic pollutants presnece, the g-C_3N_4 photocatalytic oxidation stability is due to the last intense of hydroxyl radicals in normal conditions, thereby, ensuing into the preferential decomposition of the pollutants over g-C_3N_4 (Maeda et al., 2013).

Similarly, Li (2018) devoted greater emphasis on addressing two interfaces of 2D layer g-C_3N_4, including the disorganized of electron transport and inefficient intercellular electrons

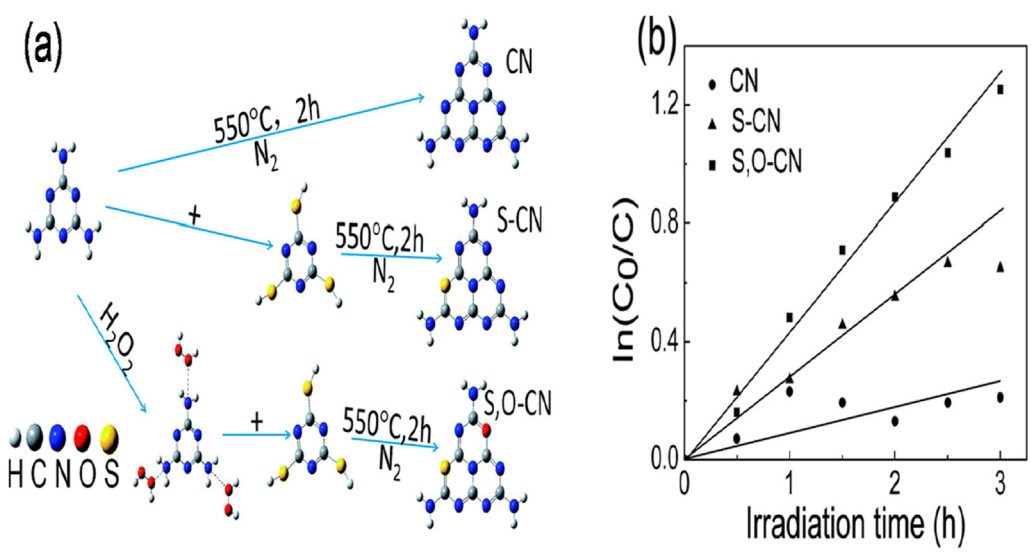

Fig. 38 (a) Fabrication process, and (b) O and S co-doped g-C_3N_4 phtocaalytic performamce towards RhB degradation. Reprinted with permission from You (2017). Copyright © 2017, RSC Publishing.

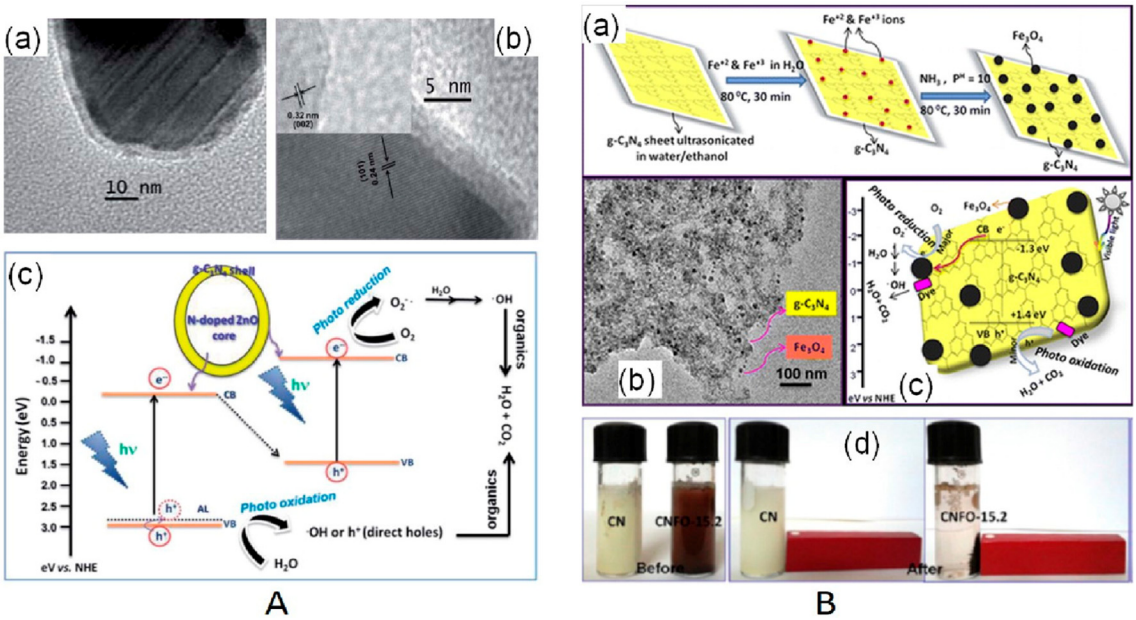

Fig. 39 (a, b) As prepared N-ZnO-g-C_3N_4 core–shell nanoplates TEM pictures, along with (c) Z-scheme mechanism. Reprinted with permission from Kumar (2014). (B) (a) fabrication approach, (b) TEM photograph, and (c) g-C_3N_4–Fe_3O_4 nanocomposite based photodegradation mechanism along with (d) photocatalyst post-reactions magnetic separation. Reprinted with permission from Kumar (2013). Copyright © 2014, RSC publishing.Copyright © 2013, American Chemical Society.

propagation. Researchers created interior van der Waals heterojunction (IVDWHj) inside g-C_3N_4 using a straightforward synthetic method, greatly increasing the interfacial coulomb association and allowing the axially directed charged dissociation (Fig. 40a, b). The resulting g-C_3N_4 containing IVDWHs showed an improved protracted photocatalytic performance, with over 100 percent augmentation of NO effectiveness comparison with pristine g-C_3N_4 (Fig. 40c, d). NO purifying over CN premised materials is performed by NO oxidation to NO_2^- and NO_3^- by photoinduced superoxide radicals, including •O_2^- and •OH. The improved •O_2^- and •OH levels (Fig. 40e, f) clearly demonstrate the accelerated electrons activation and charge transport in O, K^- integrated CN.

3.4. g-C_3N_4-based 3D hydrogels for waste water treatment

Direct discharge of wastewater containing organic contaminants is particularly hazardous for environment and human health (Zubair, 2021; Liang, 2019). These organic contaminants can be removed by absorption using porous materials (Tan, 2015), but degradation of these organic contaminants using photocatalyst (Hao, 2018), could help to solve this problem (Huang, 2021). In particular, polymeric hydrogels having high specific surface area might be effective contaminant adsorbents. To enhance the waste water treatment performance, g-C_3N_4-based hydrogels has shown to be great approach for degradation of organic contaminants photcatalyically. It is because photocatalyst-based hydrogels have greater ultra violet and light response rate, producing active species to convert contaminants into CO_2 and water, but they have greater porous structure, large pore volume and surface area, enabling for effective contaminant adsorption. Self-assembled g-C_3N_4/graphene type and polymeric g-C_3N_4-based hydrogels are utilized for the photodegradation of hazardous organic and inorganic contaminants in wastewater. The 3D CNGA porous framework enhanced light absorption and boost the photoexcited electrons transfer from g-C_3N_4 to the surface of GO through interconnected pores (Tong, 2015; Hao, 2021). Furthermore, organic pollutants with high adsorption capacity (32 mgmg/1 for methyl orange (MO) dye) implies the availability of numerous active sites, so kinetically advantageous for photocatalytic reactions on surface. The degradation efficiency was significantly reduced after adding methanol and EDTA in a photocatalytic mechanism test, demonstrating that CO_2@ and COH are species involve in methyl orange degradation utilizing CNGA materials (Fig. 41a).

Wu and colleagues found that g-C_3N_4/GO based aerogel can degrade MO and MB (20 mgL@1) >90% in just half an hour under solar light and active CO_2 @ species were main element for MO degradation in oxygen environment (O_2 + e@!CO_2 @) (Tang, 2017). Zhang et. al. discovered self-assembled g-C_3N_4 hydrogel exhibited incredibly preferential dye adsorption due to its large surface area (190 m^2 g^{-1}) and induced by high negative or positive charge character (Zhang, 2016). Furthermore, the negative zeta potential of self-assembled hydrogels (h-CN), have strong electrostatic π-π interaction among self-assembled hydrogels and dye molecules having distinct charge states, determine the extraordinary capacity for photocatalytic reaction and selective adsorption of h-CN system (Fig. 41b). Shalom and team also demonstrated the adsorption of cationic dyes for MB using self-standing h-CN (Sun, 2017). The fact that the adsorbate and h-CN have strong chemical bonds suggests that dye adsorption on hydrogel is important for its removal as consistent with previous study. In addition, as a hybrid hydrogel composite comprising conductive material (PANI), synthetic polymer (PA) and

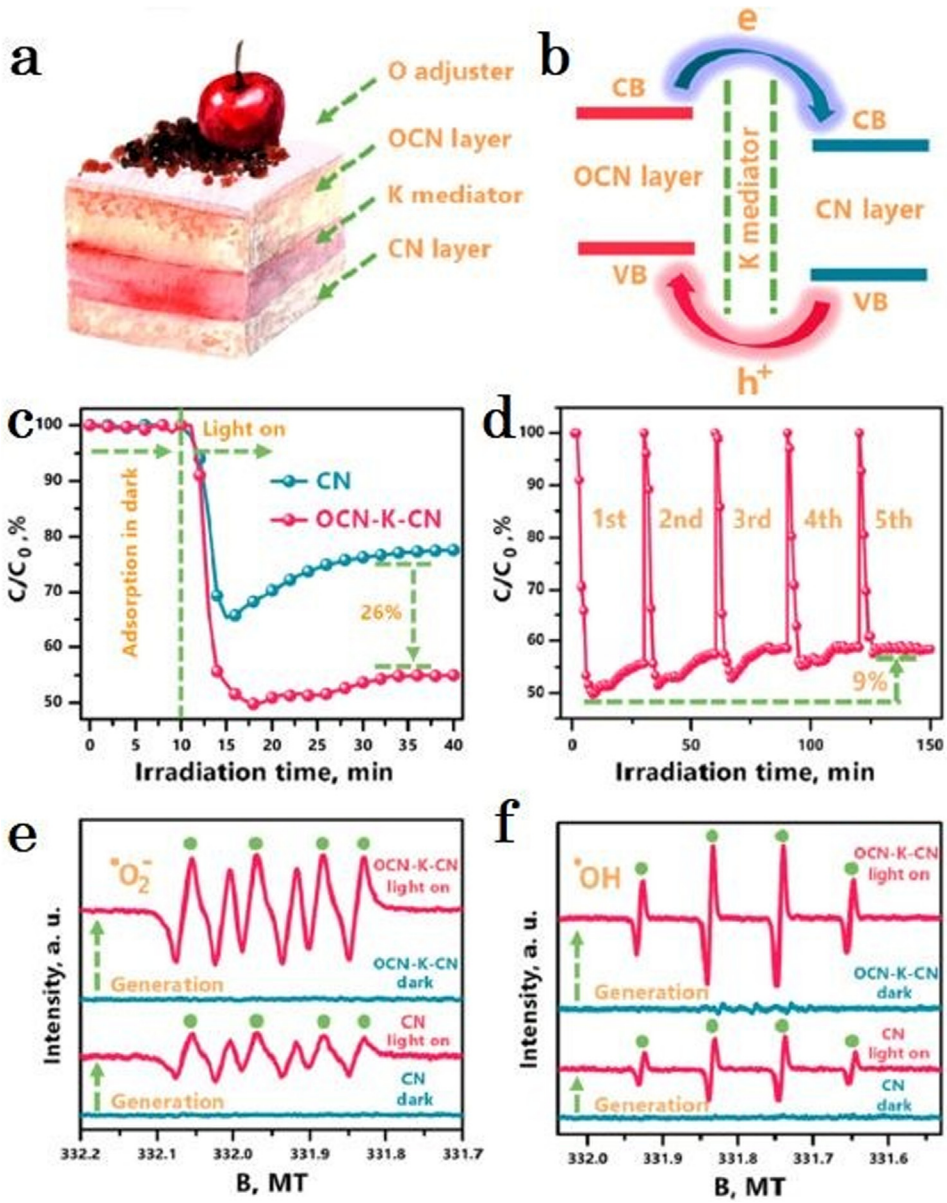

Fig. 40 Graphical depiction of the interior van der Waals heterojunction (IVDWHj) (a) "cake Framework" configuration of OCN-K-CN; (b) Band design of the OCN-K-CN IVDWH; (c, d) Photocatalytic performance contrast of CN and OCN-K-CN against NO purifying and (c) stability assess of OCNK-CN (d); (e, f) DMPO ESR peaks of CN and OCNKCN in dark/light region ($\lambda \geq 420$ nm). Reprinted with permission from Li (2018). Copyright © 2018, American Chemical Society.

biopolymer (Agar) were synthesized with g-C_3N_4 (Zhang, 2016; Jiang, 2016; Lamkhao and Randorn, 2017). Zhu and colleagues demonstrate a direct co-condensation process for the synthesis of g-C_3N_4/agar hydrogel with easy transfer of mass for adsorption and decontamination (Zhang, 2016). A PANI/h-CN having 3D framework demonstrates suitable HOMO and LUMO for good transmission of photoinduced electrons/holes pair, leading to increased the photocatalytic performance (Jiang, 2016). Zhu and colleagues discovered that a g-C_3N_4/SiO_2 hybrid hydrogel had adsorption capabilities of 3.5 and 48 mgg@1 for phenol and MB, respectively (Zhang, 2016). The zeta potential of the SiO_2 hydrogel got more negative as the g-C_3N_4 content increased, but the adsorption ability for organic contaminants don't have any effect. Zhang and co-workers discover the idea that the zeta potentials and surface charge natures of g-C_3N_4/SiO_2 hydrogels alter their adsorption abilities, especially for MB and phenol adsorption (Zhang, 2016). Among all, the coupling of BiOBr or Cu_2O can result in more effective charge separation for g-C_3N_4-based hydrogels (Yu, 2017; Yan, 2017). The photocatalytic performance of these oxide loaded g-C_3N_4 based hydrogels depend on two factors. First one is of good surface area due to 3D porous structure, which allow for multiple surface-active sites, while the other is the p–n heterostructure interface among g-C_3N_4 and oxide materials, which allows for excellent separation of charges (Fig. 42). The performance of oxide loaded g-C_3N_4 hydrogel is increased by working together in both mechanisms.

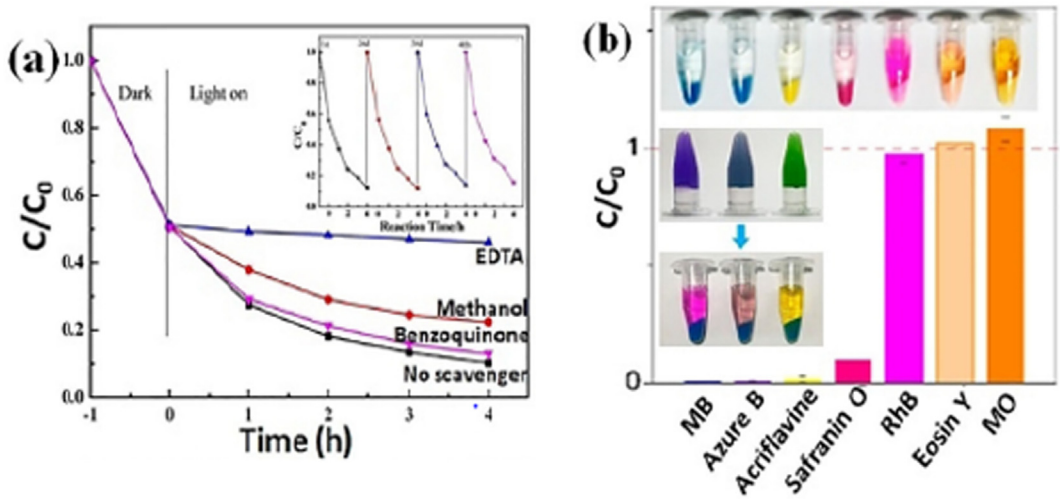

Fig. 41 (a) Degradation of MO dye with CNGA in the presence of scavengers and inset showing the cyclic test of CNGA, (b) Highly selective dye adsorption toward MB, azure B, acriflavine, safranin O, RhB, eosin Y, and MO using h-CN. Inset of (b) shows photographs of dyes. Reprinted with permission from Tong (2015). Copyright © 2015, American Chemical Society.

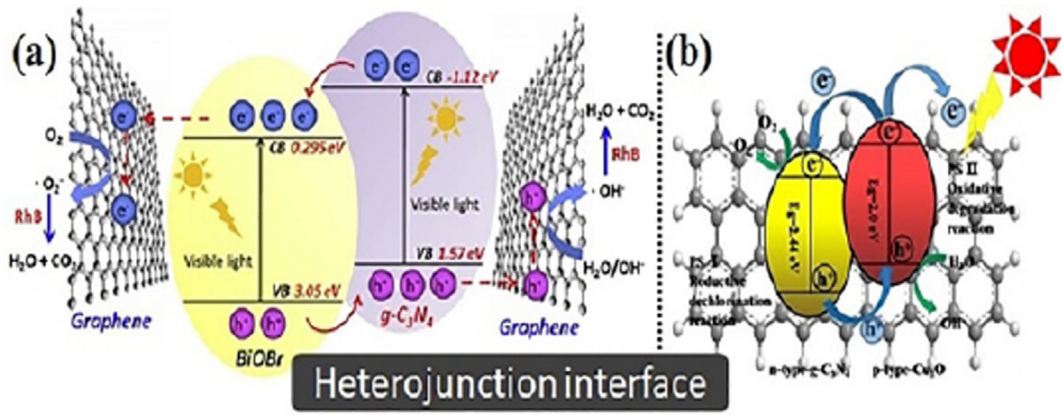

Fig. 42 Schemattic representation of heterostructure of the g-C_3N_4/GO hydrogel with (a) BiOBr. Reprinted with permission from Yu (2017). Copyright © 2017, Elsevier, and (b) Cu_2O. Reprinted with permission from Yan (2017). Copyright © 2017, Elsevier.

3.5. Nitrogen photo-fixation

Nitrogen fixation is a revolutionary achievement by using g-C_3N_4 photocatalyst. Nitrogen could be transformed to ammonium, nitric acid, nitrous acid, and ammonia that are more valuable products than normal nitrogen. Fig. 43 depicts the nitrogen fixation procedure utilizing g-C_3N_4 as a photocatalyst (Ajiboye et al., 2020). In recent decades, photocatalytic N_2 fixation technique has been attracted more attention in energy and fuel production for its easy reaction conditions, low utilization of energy, cheap, and sustainable method that relies solely on limitless clean sunlight energy (Chen, 2018; Hao, 2020). Especially metal-free g-C_3N_4 photocatalysts, having nitrogen vacancies and matched heterostructure surfaces, have attracted the attention of N_2 fixation process (Li, 2018; Liang et al., 2017; Shi, 2018; Cao, 2018). Nitrogen vacancies are useful in chemical adsorption and activations of nitrogen, because the nitrogen atoms in dinitrogen have identical size and shape.

Dong and coworkers demonstrated integration of nitrogen vacancies within g-C_3N_4 framework that could photo reduced the nitrogen content and considerably improve isolation of charge carriers by capturing the photoexcited electrons and stimulating their transfer to the adsorbed nitrogen (Dong et al., 2015). Liu and coworkers demonstrated the fabrication of MXene derived TiO_2@C/g-C_3N_4 heterostructure by calcination of melamine and Mxene $Ti_3C_2T_x$ (Chen, 2015). The fabrication method yields carbon nanosheets (2D-Planer) supported on TiO_2 with a high amount of Ti_3^+ entities, that are compactly enfolded by in situ synthesized g-C_3N_4 nanosheets. Surprisingly, as-prepared catalyst showed good photocatalytic performance for reduction of nitrogen to NH_3 with an average rate of 250 mmol/g^1 h^1. Such high performance is owing to the presence of adequate surface defects, increased light capture, and remarkable charge separation and transfer ability of materials. For 2D graphene, Hu and coworkers created metal free 2D/2D nanocomposites of g-C_3N_4/rGO by connecting protonated g-C_3N_4 and rGO, in which reduced GO works as a conductive material (Hu, 2016). The as-prepared heterostructure produced five times more NH_3 than bulk g-C_3N_4, owing to appropriate interaction of rGO and protonated g-C_3N_4

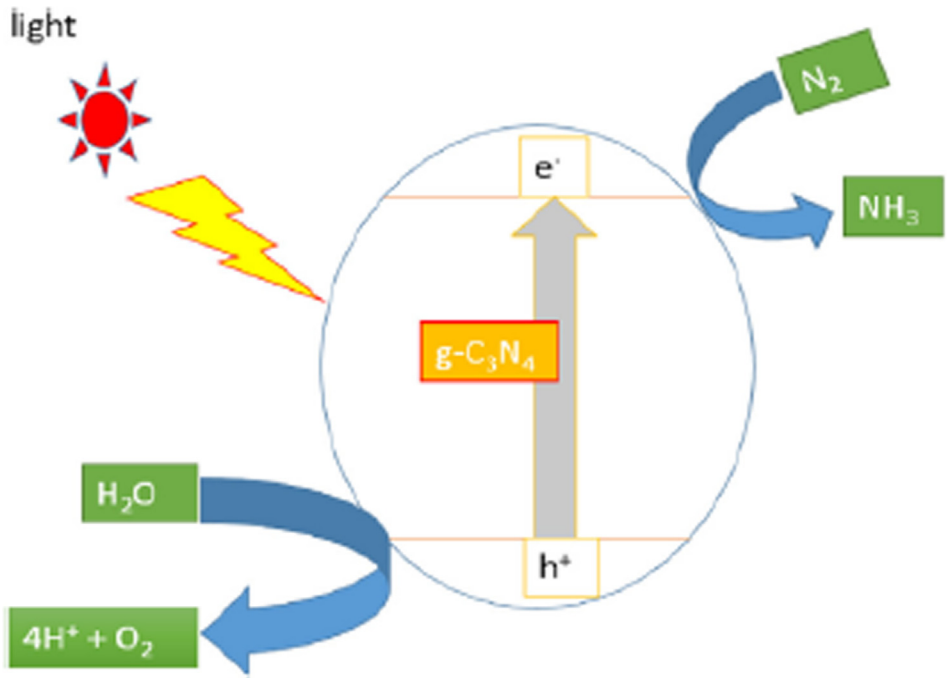

Fig. 43 Nitrogen fixation using g-C_3N_4 mechanism. Reprinted with permission from Ajiboye et al. (2020). Copyright © 2020, Elsevier.

across the g-C_3N_4/rGO heterostructure, that effectively suppressed the radiative charge carrier recombination and improved charge separation and transfer ability. Other than 2D/2D heterostructure, multi metal oxides with tunable band structures suit well with g-C_3N_4 semiconductor photocatalyst through intact heterostructure. Wang and coworkers effectively demonstrated the fabrication of a g-C_3N_4/MgAlFeO nanorod heterostructure for excellent performance for nitrogen reduction (Wang, 2017). Similarly, in Fig. 44a, a Z scheme heterostructure was formed, in which the photoinduced electrons from the CB of MgAlFeO moved to VB of g-C_3N_4, leading in better separation of charge and higher interfacial charge transfer, resulting in strong N_2 photofixation. Cao et. al. discovered a comparable Z-scheme heterostructure method for nitrogen photofixation, in which 3,4-dihydroxybenzaldehyde doped Ga_2O_3/g-C_3N_4 (Ga_2O_3-DBD/g-C_3N_4) was synthesized by introducing Ga_2O_3-DBD nanoparticles within the g-C_3N_4 structure through a simple post-grafting approach (Fig. 44b) (Cao, 2017). In the composites, the benzene ring act as a electron mediators that enhanced the separation of photogenerated charges by making well-matched interface among Ga_2O_3-DBD/g-C_3N_4 and making it easier to change nitrogen into ammonia with help of reducing ability of CO2 (Hao, 2021. 2021.), as seen in Fig. 44c. The preceding research effectively demonstrated that the metal free g-C_3N_4 photocatalyst with rational heterostructure fabrication can provide impressive performance towards ecofriendly nitrogen photofixation technology for global growth.

3.6. Photoelectronic application

The addition of nitrogen into the carbon matrix brought an improvement in its electrical, structural, and mechanical properties, particularly its electronic properties, which in turn makes it a potential candidate to be used in rechargeable batteries (He, 2015; Li, 2017; Reli, 2016; Ohno, 2014; Hao, 2021), light-emitting devices (He, 2015; Zhao, 2017), fuel cells (Li, 2015; Bai, 2016; Li, 2017; Liu, 2017; Ye, 2016), solar cells, and other applications (Shi, 2015; Bai, 2016). Moreover, the g-C_3N_4 has been regarded as a most promising candidate in the overhead application domains. The sp^2 hybridization of nitrogen and carbon results in forming a π-conjugated electronic structure, which has an excellent photoelectronic characteristic (Richardson and Ternes, 2014).

3.6.1. Light-emitting devices

Due to its semiconductor features, the researchers are now concentrating onto the luminescence of g-C_3N_4 (Tyborski, 2013). In general, the optical band gap of g-C_3N_4 dominates the photoluminescence area, and it has been shown that the band gap of g-C_3N_4 is tunable by adjusting the processing temperature. The optical band gap and synthesized temperature are thought to be efficiently connected in the tectonic unit of g-C_3N_4, as shown in Fig. 45 (Tyborski, 2012).

The photoluminescence functionality of g-C_3N_4 was explored in depth by Dong's group. As shown in Fig. 46 (Zhang, 2013), the resultant emission area of g-C_3N_4 ranging from 400 nm to 510 nm, due to constant modulation of the processing temperature. On the basis of two-dimensional conjugated polymeric system and the lone pair of g-C_3N_4, a promising energy level mechanism diagram has been proposed, thereby, concluding that the narrow band gap was primarily instigated through the advancement of the conjugated polymeric structure and electron delocalization.

Chen et. al. lately stated the ECL of g-C_3N_4 nanoflake films. The substantial ECL performance with (435 nm) blue light emission was estimated, under reductive-oxidative co-reactants environment (Jo, 2017). This is noteworthy that the ultrathin (g-C_3N_4) nanosheets might be fabricated via exfoliating bulk g-C_3N_4, and its PL quantum vintage could be high

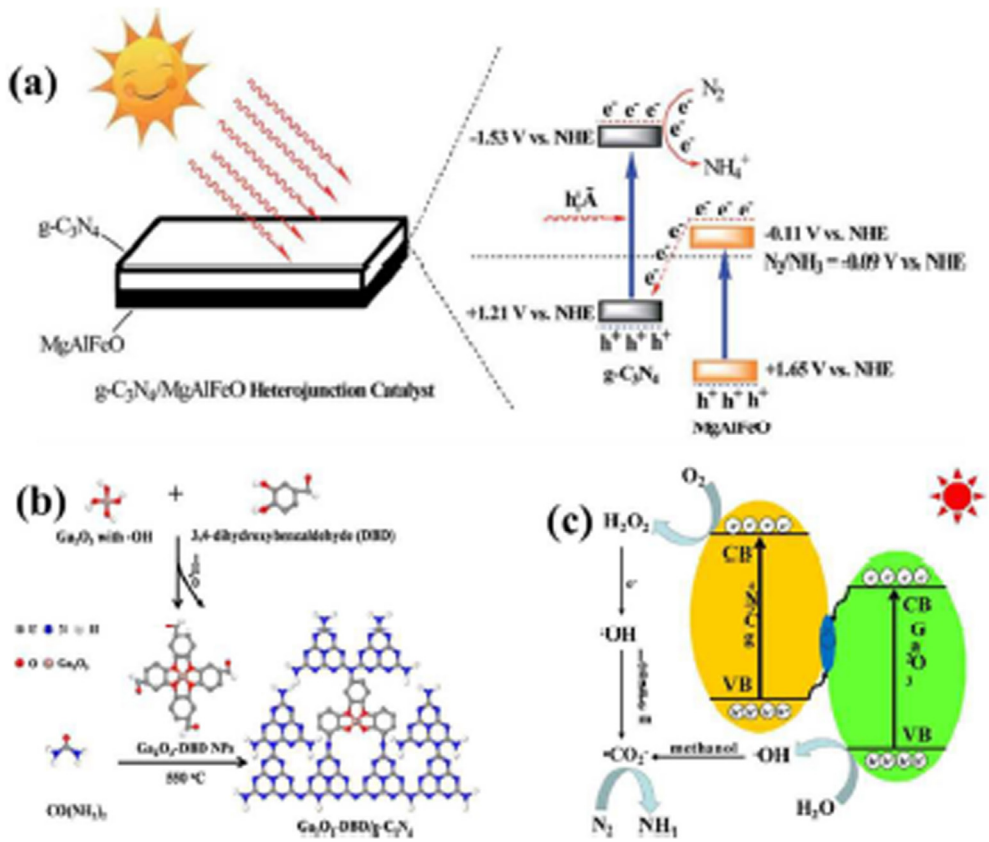

Fig. 44 (a) g- C_3N_4/MgAlFeO possible mechanism, (b) The synthesis scheme and, (c) photocatalytic N_2 reduction mechanism of Ga_2O_3-DBD/g-C_3N_4. Reprinted with permission from Cao (2017). Copyright © 2017, Elsevier.

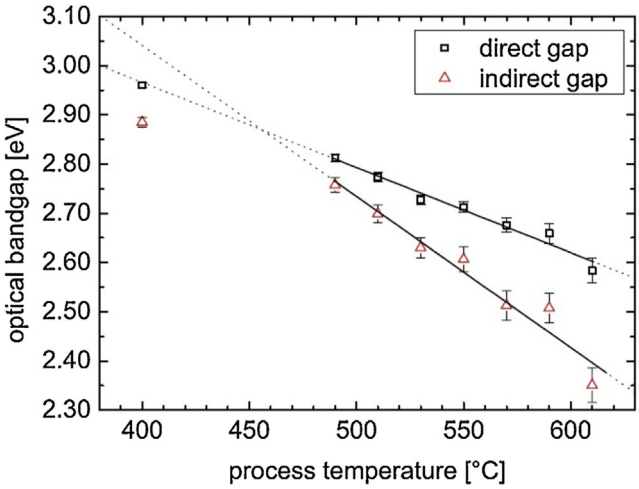

Fig. 45 Values of direct (squares) and indirect bandgaps (triangles) for carbon nitride powders processed at different temperatures. The solid black lines denote linear fits in the range between 490 and 610 ∘C, the dotted lines being extrapolations. Reprinted with permission from Tyborski (2012). Copyright © 1989, IOP Publishing.

about 19.6% (Li et al., 2016). The optical characteristics and ECL activity of g-C_3N_4 demonstrate a superior performance in light-emitting devices. In light-emitting devices, the fluorescence powers of commercial nitrides via doped with transition ions or rare-earth ions are commonly employed. Although their luminescence qualities and quantum efficiency are good, metal toxicity, standard synthesis parameters, and their limit utilization (Tonda, 2014; Gao, 2015; Essekri, 2020). The Reyes et. al. further employed amorphous-CNx as a light-emitting material in order to develop a light maneuver, that exhibited a white–blue electro-luminescence at ambient temperature, which is presented in Fig. 47 (Yan et al., 2010; Ji, 2017). According to their investigations on the white light-emitting device, the C-N link of amorphous g-C_3N_4 emits green and blue light, whereas the C-H bond emits red light. However, it has been further proposed that g-C_3N_4 might be employed as a semiconductor layer in light-emitting devices, since it has a similar emission area to amorphous-CNx.

3.6.2. Photocathodes

Semiconductor materials used in photoelectrochemical cells (PEC) for solar energy conversion into value-added chemicals are vital in developing sustainable energy to address current energy issues. The photoanodes for PEC water oxidation by employing n-type semiconductors i.e., WO_3, Fe_2O_3, ZnO, and TiO_2, are extensively investigated. Furthermore, few investigations have been conducted on the use of p-type semiconductors as photocathodes for photoelectrochemical cell reduction of water. The g-C_3N_4 is considered as a possible semiconductor for photocathodes, because of its high chemical durability and unusual electrical structure. The Zhang et. al.

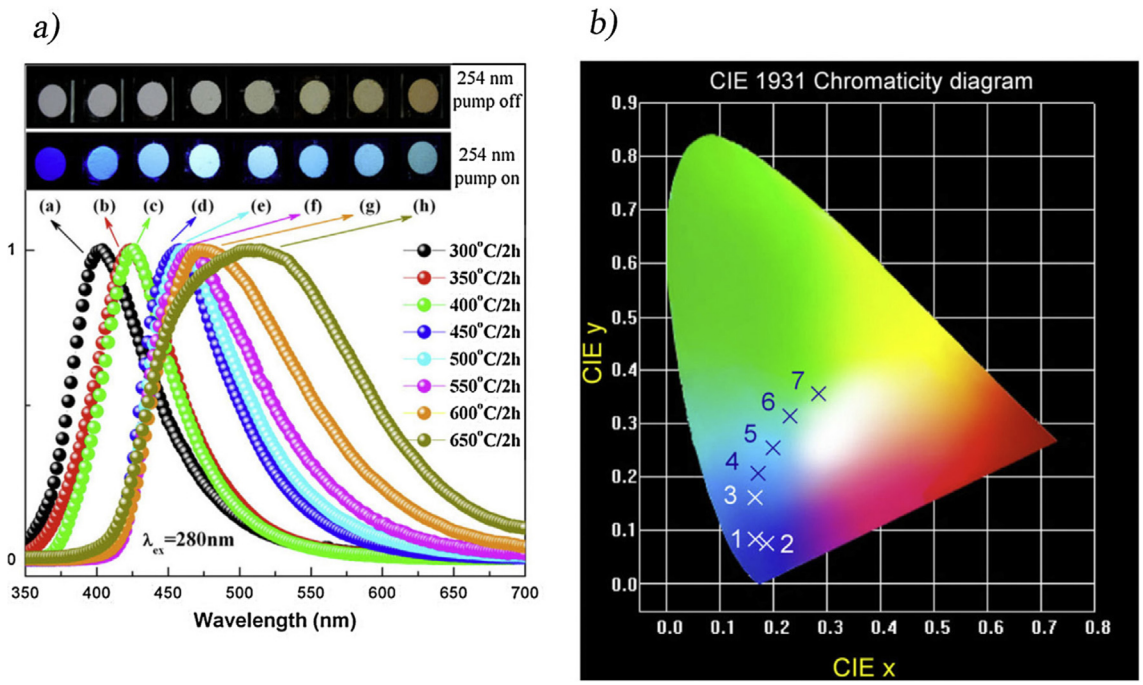

Fig. 46 (a) The normalized PL emission spectra of the g-C_3N_4 products were synthesized via melamine's thermal condensation at different temperatures for 2 h (ex = 280 nm). The inset shows the digital photos of g-C_3N_4 products with (bottom) and without (upper) 254 nm excitation; (b) The Commission International de L'Eclairage (CIE) chromaticity diagram of the carbon nitride products synthesized at different temperatures for 2 h. (1) 350 ∘C, (2) 400 ∘C, (3) 450 ∘C, (4) 500 ∘C, (5) 550 ∘C, (6) 600 ∘C, (7) 650 ∘C. Reprinted with permission from Zhang (2013). Copyright © 2013, Springer Nature.

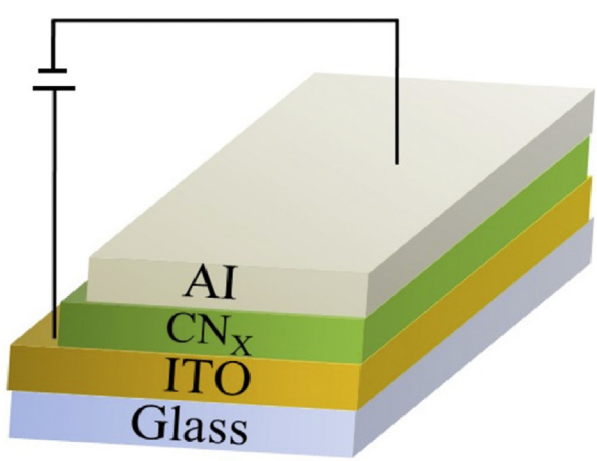

Fig. 47 Emitting light device configuration (Ji, 2017).

integrated active carbon sites to fabricate a long-lasting photocathode with three times more cathodic PEC performance as compared to pristine g-C_3N_4 (Panneri, 2017). Carbon inclusion is anticipated to significantly impact the electrical characteristcis of the g-C_3N_4 structure via the following mechanisms: (1) Charge separation efficiency is demonstrated by a decrease in photoemission intensity, which enhances charge mobility; (2) the π-conjugated framework is improved. Both of these elements help to increase the mobility of the charge. Furthermore, the nanostructure influences the free carrier diffusion, mass transfer, and active sites, impacting PEC efficiency. Fig. 48 depicting the differences in PEC activity amid pure and carbon-doped g-C_3N4 (Zhang, 2013). The PEC activity is projected to increase as electrical structures, change-carrier mobility, and surface area are all balanced.

3.6.3. Optical sensors

Optical sensor systems have attracted much research interest, because of their precise and reasonable detection limit and guaranteed biocompatibility and flexibility. Usually, the optical sensor is a molecule receptor with variable optical capabilities based on the specific visitors (Dai, 2013). Presently, fluorescent receptors are commonly used as optical sensors for detections by the interaction of fluorescent with adherent guests. The optical response is dominated by the transport of electrons from receptors to their binding guests. It is well known that g-C_3N_4 is an excellent catalyst to substantially absorb metal ions via chelation or redox reaction, since it has functions such as NH_2/NH/N over surface site. Despite many sensors with an optical receptor attaches to permeable materials, the g-C_3N_4 is the receptor itself and has excellent sensitivity. Lee et. al. investigated the possibility of using g-C_3N_4 as an optical sensor to check the presence of metal ions in an aqueous solution by examining its photoluminescence quenching effects (You, 2017; Dai, 2013). The findings in Fig. 49 reveal that g-C_3N_4 has good Cu^{2+} sensitivity. The Cu^{2+} entirely quenches photoluminescence thru no visible interfering from other metals, because photo-generated electrons are collected by Cu2+ (Lee, 2010). Furthermore, the Stern–Volmer equation may be used in order to quantify the degree of quenching: I0/I = 1 + KSV[Q], where I_0 and I indicate the luminescence intensity in the absence and presence of metal ions, respectively. The Stern–Volmer constant (You,

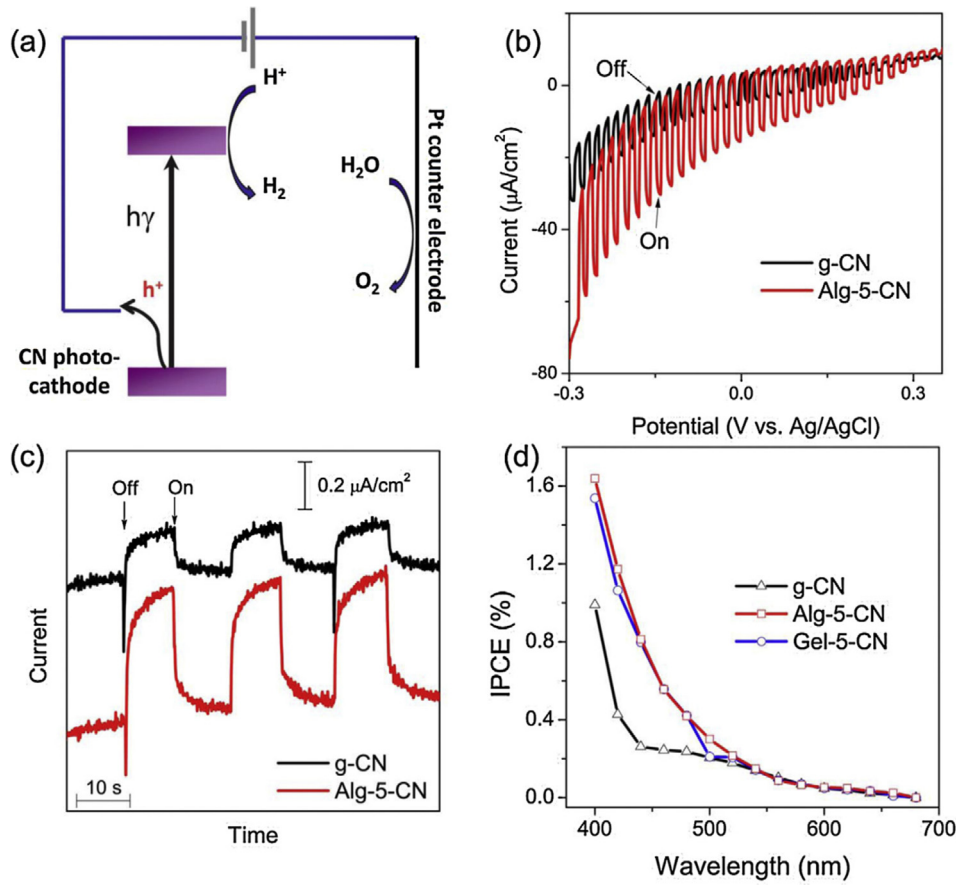

Fig. 48 Photoelectrochemical (PEC) properties of carbon nitrides in 0.1 M KCl aqueous solution. (a) The PEC cell configuration and possible charge transfer (the reference electrode was omitted for clarity). (b) Characteristic photocurrents at g-CN (black) and Alg-5-CN (red) photocathode under a chopped sunlight simulator at a scan rate of 10 mV/s. (c) The transient current response of g-CN (black) and Alg-5-CN (red) at −0.2 V vs Ag/AgCl (sat. KCl) under chopped monochromatic light at 440 nm. (d) Photo action spectra of g-CN (black), Alg-5-CN (red), and Gel-5-CN (blue) biased at −0.2 V vs Ag/AgCl (sat. KCl). Reprinted with permission from Zhang (2013). Copyright © 2013, Springer Nature.

2017) is denoted by [Q], which is molar concentration of the metal ion. This comparation depicts a roughly linear relationship between the effect of Cu^{2+} concentration on g-C_3N_4 photoluminescence.

3.7. Bacterial disinfection

It is critical for human health to remove pathogenic bacteria from water. Although earlier disinfection processes such as chlorination and ozonation were highly successful for inactivation, as they frequently produced hazardous disinfection by-products having carcinogenic and mutagenic potential (Muellner, 2007; He, 2016; Malik, 2021). In 1985, the Matsunaga et. al. (Matsunaga, 1985), were the first to demonstrate photocatalytic sterilization of microbial cells in water. The first time Huang et. al. found the bactericidal effects of g-C_3N_4 on Escherichia coli (E.coli) K-12 in water, when irradiated with visible light (Huang et al., 2014). Mechanistic illustration showed that, the light-induced holes over g-C_3N_4 surface sites were shown to be a major source of the inactivation of bacteria. As a result, using a hole scavenger like OH had minimal influence on the inactivation efficiency (Huang et al., 2014). The use of single layer g-C_3N_4 was invetigated by Zhao et. al. in order to examined the photocatalytic disinfection of E. coli in visible-light (Zhao, 2014). The Fig. 50a displays the disinfection activity of several photocatalysts for E. coli, with single-layer g-C_3N_4 by providing the best results. As demonstrated in (Fig. 50b), adding isopropanol or Cr (VI) caused in killing around five log10 of E. coli cells in 4 h. Though, only about two log10 of E. coli cells were smashed, when KI was added. As a result of the findings above, the disinfection in visible light seems to be a hole oxidation process. The effects of disinfection on E Coli were investigated further using microstructure and morphology analysis earlier and afterward disinfection. Fig. 50c shows the E Coli cell wall, before photocatalytic disinfection, which is highly conserved. The cell wall of bacteria is destroyed after 12 h of irradiation, as seen in Fig. 50d, f.

Wang et. al. developed a metal-free heterostructure of cow wrapping Sulfur (−S8) on rGO sheets and g-C_3N_4 for bacteria disinfection during visible light. They examined the disinfection of E. coli K-12 cells via two diverse heterostructures (Fig. 51a) and rGO was found between -S8 and g-C_3N_4 in the first structure (CNRGOS8), whereas g-C_3N_4 was found between -S8 and rGO in the second structure (CNRGOS8). The aforesaid synthesized heterostructures (CNRGOS8 and

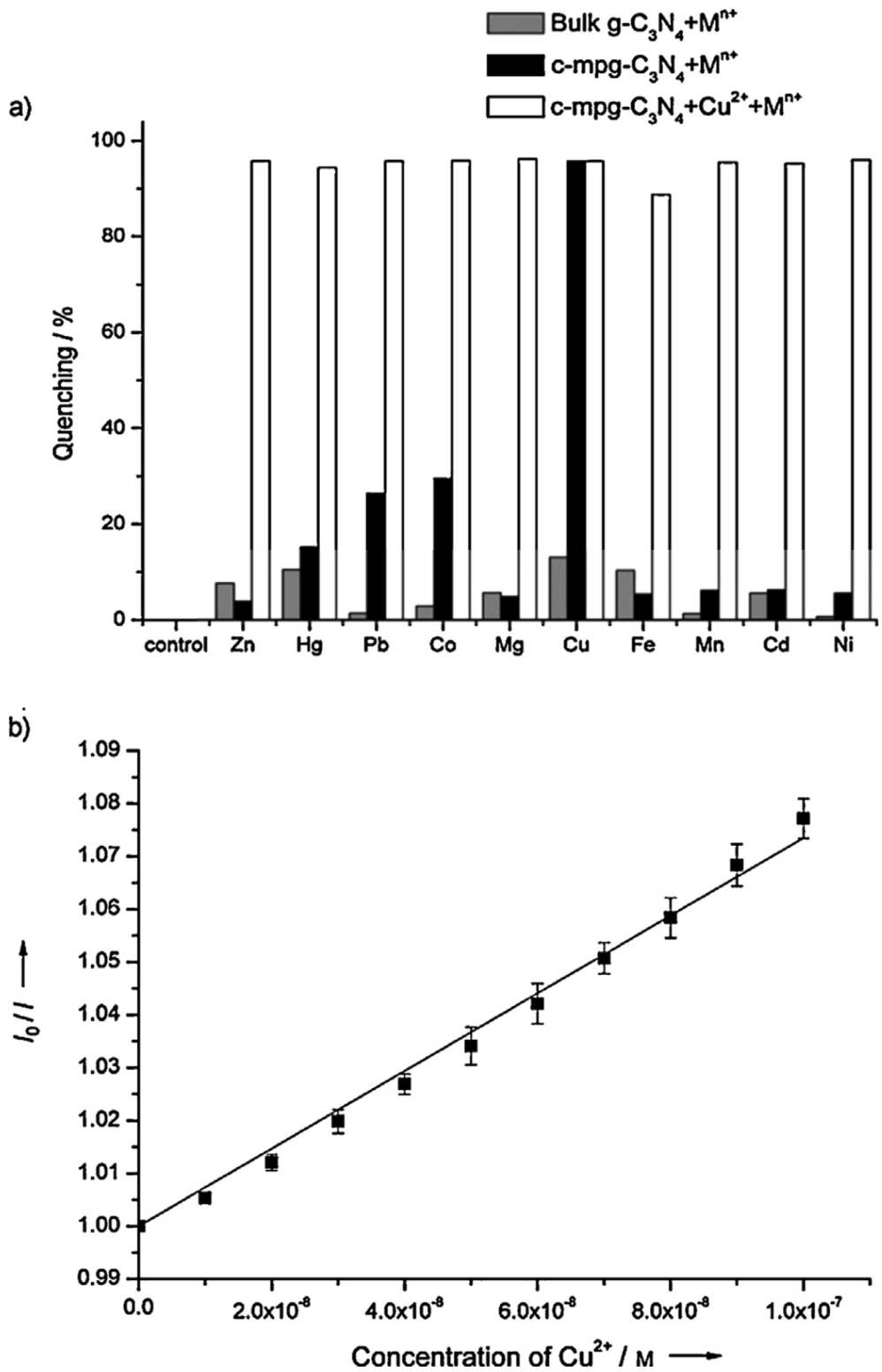

Fig. 49 (a) PL spectra of both c-mpg-C_3N_4 (black bar) and bulk (gray bar) after 1 mm of metal ion solutions treatment, and (1 mm) of other metal ions intrusion with (1 mm) Cu_2^+ (white bar); (b) PL spectra of c-mpg-C_3N_4 to Cu_2^+ in 10–100 nm concentration range. Reprinted with permission from Lee (2010). Copyright © 2010 John Wiley and Sons.

RGOCNS8) exhibit different photocatalytic performance towards E. coli K-12 in anaerobic and aerobic conditions (Fig. 51b, c). As shown in Fig. 51a, b, the CNRGOS8 has a more excellent photocatalytic activity for bacterial inactivation in an aerobic environment than RGOCNS8, whereas the RGOCNS8 works better in anaerobic situations (Fig. 51C). The photocatalytic route in an anaerobic environment was more reductive than the oxidation process. Therefore, such dis-

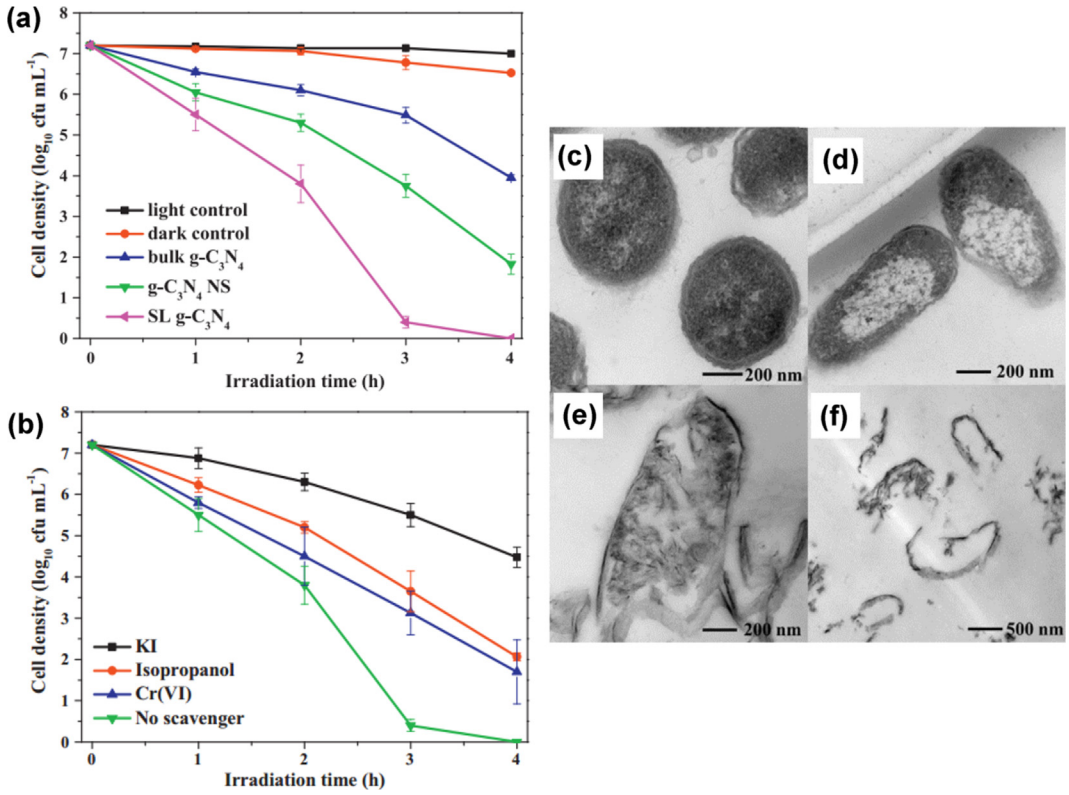

Fig. 50 Photocatalytic disinfection performace of (a) various g-C_3N_4 and (b) single-layer g-C_3N_4 with diverse scavengers. g-C_3N_4 NS and SL g-C_3N_4 indicates g-C_3N_4 nanosheets and, single-layer g-C_3N_4, correspondingly. The TEM picture of E. coli before and after photocatalytic disinfection: (c) Before reaction and after irradiation for (d) 4 h, (e) 8 h, and (f) 12 h. Reprinted with permission from Zhao (2014). Copyright © 2014, Elsevier.

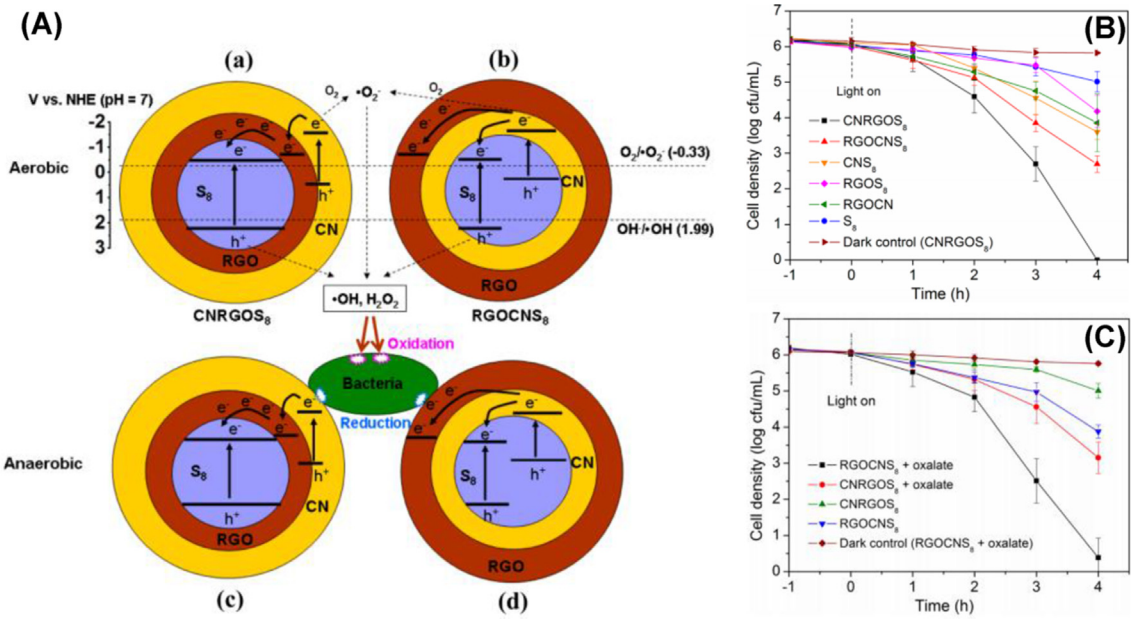

Fig. 51 (A) Graphic represnetation of mechanism of photocatalytic bacterial inactivation (a) CNRGOS8 and (b) RGOCNS8 in aerobic and (c) CNRGOS8 and (d) anaerobic conditions of RGOCNS8. Photocatalytic inactivation activity vs E. Coli K-12 during as-prepared samples presence (B) aerobic and (C) anaerobic conditions under visible-light irradiation. Reprinted with permission from Wang (2013). Copyright © 2013, American Chemical Society.

covery unfastens inventive paths for studying the use of metal-free catalysts to improve bacterial photoinactivation effectiveness (Wang, 2013).

4. Future prospective

Despite tremendous advances in past years, the major challenges persist in rationally designed extremely effective g-C_3N_4-based photocatalyst in terms of the number of their uses and the full knowledge of the fundamental tailoring process of g-C_3N_4-based photocatalysts. Hence, several unresolved concerns and areas exist, where more research is needed. So far, deep studies are urgently needed to fully explore the structural and electrical characteristics of g-C_3N_4 composites. Conversely, the diverse features of g-C_3N_4-based photocatalysts also need to be thoroughly investigated. Owing to the challenges in developing extremely efficient and sustainable g-C_3N_4-based photocatalysts with decreased band gaps, the creation of low band gap conjugated polymers may yield additional concepts for speeding organic semiconductor-based photocatalysis advances. The g-C_3N_4 nanosheets further require accurate surface defect regulation and simple scale preparation techniques. Advanced photo-electrocatalysts must be employed to explore the applications of a g-C_3N_4-based catalysts for the scientific community. In constructing practical g-C_3N_4-based photocatalysts, dimension controll, pore-size modifications, heterostructure building, cocatalyst and catalyst loading, and nanocarbon loading appear to be the most promising design strategies. More research into this method is required at this time. In these photocatalytic areas, developing Earth-abundant co-catalysts is still a challenging task. Nanocarbons will forever play vital roles in the construction of highly effective g-C_3N_4-based photocatalysts. In addition, the uses of g-C_3N_4-based photocatalyst are primarily concentrated on H_2 evolution and pollutant degradation. In contrast, during the photocatalytic CO_2 reduction process, these catalysts have grown in popularity over the past few years. The fundamental character of the surface of g-C_3N_4 dictates its promising future in CO_2 reduction fields. Moreover, study of OER from the water splitting half reaction, which involves both CO_2 reduction and overall water splitting, should receive more attention in the coming years. Furthermore, the process's precise mechanism, especially CO_2 reduction by g-C_3N_4-based catalyst, remains unclear and unexplored. Deep research in reaction pathways is mandatory for elucidating the fundamentals improvements of photocatalysis and designing effective g-C_3N_4-based photocatalysts in the future. Moreover, a few key concerns that are necessary for good photocatalytic activity, such as light absorption, charge separation and transfer, and band structure, must be thoroughly evaluated using both DFT and practical experiments to gain theoretical insights. Charge separation and transfer ability, substrate adsorption sites and molecular orbitals should all be comprehensively studied pertaining to experimental efforts. The collaborative efforts of researchers from many fields and countries should result in an exciting period for g-C_3N_4-based photocatalysts.

5. Conclusions

This review article mainly deals with recent progress in the improvement of photocatalytic performance of a wide variety of properly tuned highly active carbon based g-C_3N_4 photocatalysts in photocatalysis research field. However, due to electrical, optical, and mechanical properties, the g-C_3N_4 could be further tailored for solar energy use in environmental applications and other energy conversions. The g-C_3N_4 nanomaterials with their varying porosity and dimensionality and their incorporation in multi-functional nanocomposites, have brought about the significant enhancement in the solar light absorption, charge separation/transportation, quantum yields, and photocatalytic performance. At the same time, the main difficulty still being experienced is the lack of multidisciplinary actions, and the use of sacrificial reagents to improve the photoreactor design persists. The preliminary step in the photocatalytic reduction of CO_2 is the utmost selection of the best specific product—either energy (e.g., CO, CH_4, or formic acid) or chemicals (e.g., olefins or alkanes)—to improve the activity and the capacity as well. Although the quantitative comparisons are found to be difficult owing to the decoupling of adsorption from the reaction medium to the photocatalysis process as through photo-chemical stimulation of chromophores, the dearth of calibration in experimental protocols, and the design of the reactor during wastewater treatment using a g-C_3N_4-based photocatalyst appears to be remarkable.

Declaration of Competing Interest

The authors declare that they have no known competing financial interests or personal relationships that could have appeared to influence the work reported in this paper.

Acknowledgments

We gratefully acknowledge the support of this research by funding from the Foundation of Yangtze Delta Region Institute (Huzhou) of UESTC, China, (Nos. U03210057). Authors acknowledge support and funding of King Khalid University through Research Center for Advanced Materials Science (RCAMS) under grant no: RCAMS/KKU/008/21.

References

Ahmad, H. et al, 2015. Hydrogen from photo-catalytic water splitting process: a review. Renew. Sustain. Energy Rev. 43, 599–610.

Ahmed, S. et al, 2021. Solvent assisted synthesis of hierarchical magnesium oxide flowers for adsorption of phosphate and methyl orange: kinetic, isotherm, thermodynamic and removal mechanism. Surf. Interf. 23, 100953.

Ajiboye, T.O., Kuvarega, A.T., Onwudiwe, D.C., 2020. Graphitic carbon nitride-based catalysts and their applications: a review. Nano-Struct. Nano-Obj. 24, 100577.

Ajmal, Z. et al, 2018. Phosphate removal from aqueous solution using iron oxides: adsorption, desorption and regeneration characteristics. J. Colloid. Interf. Sci. 528, 145–155.

Ajmal, Z. et al, 2020. Probing the efficiency of magnetically modified biomass-derived biochar for effective phosphate removal. J. Environ. Manage. 253, 109730.

Ajmal, Z. et al, 2020. Use of nano-/micro-magnetite for abatement of cadmium and lead contamination. J. Environ. Manage. 264, 110477.

Ajmal, Z. et al, 2021. Prospects of photocatalysis in the management of nitrate contamination in potable water. In: Oladoja, N.A., Unuabonah, E.I. (Eds.), Progress and Prospects in the Management of Oxyanion Polluted Aqua Systems. Springer International Publishing, Cham., pp. 185–217.

Aleksandra et al, 2014. Strategies for improving the efficiency of semiconductor metal oxide photocatalysis. Mater. Horiz.

Alenad, A.M. et al, 2022. Selectivity, stability and reproducibility effect of Uric acid integrated carbon nitride for photocatalytic application. J. Photochem. Photobiol., A 423, 113591.

Alivisatos, A.P., 1996. Semiconductor clusters, nanocrystals, and quantum dots. Science 271 (5251), 933–937.
Anpo, M. et al, 1987. Photocatalytic hydrogenation of propyne with water on small-particle titania: size quantization effects and reaction intermediates. J. Phys. Chem. 91 (16), 4305–4310.
AR, S.R. et al, 2020. CdSe quantum dots modified thiol functionalized g-C3N4: intimate interfacial charge transfer between 0D/2D nanostructure for visible light H2 evolution. Renew. Energy 158, 431–443.
Arif, N. et al, 2021. Homogeneous iron-doped carbon-nitride-based organo-catalysts for sensational photocatalytic performance driven by visible light. Polym. Int. 70 (9), 1273–1281.
Asahi et al, 2001. Visible-light photocatalysis in nitrogen-doped titanium oxides. Science.
Babu, P. et al, 2019. Serendipitous assembly of mixed phase $BiVO_4$ on B-doped g-C_3N_4: an appropriate p–n heterojunction for photocatalytic O_2 evolution and Cr (VI) reduction. Inorg. Chem. 58 (18), 12480–12491.
Bai, X. et al, 2013. Photocatalytic activity enhanced via g-C_3N_4 nanoplates to nanorods. J. Phys. Chem. C 117 (19), 9952–9961.
Bai, Y. et al, 2016. Size-dependent role of gold in g-C_3N_4/BiOBr/Au system for photocatalytic CO_2 reduction and dye degradation. Sol. Energy Mater. Sol. Cells 157, 406–414.
Bai, Y. et al, 2016. g-C_3N_4/Bi_4O_{512} heterojunction with I_3^-/I^- redox mediator for enhanced photocatalytic CO_2 conversion. Appl. Catal. B 194, 98–104.
Bandyopadhyay, A. et al, 2017. Photocatalytic activity of g-C_3N_4 quantum dots in visible light: effect of physicochemical modifications. J. Phys. Chem. C 121 (3), 1982–1989.
Barbero, N., Vione, D., 2016. Why Dyes Should not be used to Test the Photocatalytic Activity of Semiconductor Oxides. ACS Publications.
Bard, A.J., 1979. Photoelectrochemistry and heterogeneous photocatalysis at semiconductors. J. Photochem. 10 (1), 59–75.
Barrio, J.s. et al, 2018. Design of a unique energy-band structure and morphology in a carbon nitride photocatalyst for improved charge separation and hydrogen production. ACS Sustain. Chem. Eng. 6 (1), 519–530.
Bell, A.T., 2003. The impact of nanoscience on heterogeneous catalysis. Science 299 (5613), 1688–1691.
Brini, L. et al, 2021. Synthesis and characterisation of PANI- coated Heliotrope Leaves (PANI@HL) with high clean-up capacity for Orange G dye from aqueous media. Int. J. Environ. Analyt. Chem., 1–17
Brini, L. et al, 2021. Synthesis and characterization of arginine-doped heliotrope leaves with high clean-up capacity for crystal violet dye from aqueous media. Water Sci. Technol. 84 (9), 2265–2277.
Cao, S.-W. et al, 2013. In-situ growth of CdS quantum dots on g-C_3N_4 nanosheets for highly efficient photocatalytic hydrogen generation under visible light irradiation. Int. J. Hydrogen Energy 38 (3), 1258–1266.
Cao, S. et al, 2017. All-solid-state Z-scheme 3, 4-dihydroxybenzaldehyde-functionalized Ga_2O_3/graphitic carbon nitride photocatalyst with aromatic rings as electron mediators for visible-light photocatalytic nitrogen fixation. Appl. Catal. B 218, 600–610.
Cao, S. et al, 2018. Nitrogen photofixation by ultrathin amine-functionalized graphitic carbon nitride nanosheets as a gaseous product from thermal polymerization of urea. Appl. Catal. B 224, 222–229.
Cao, J. et al, 2019. Photocatalytic activation of sulfite by nitrogen vacancy modified graphitic carbon nitride for efficient degradation of carbamazepine. Appl. Catal. B 241, 18–27.
Chen, S. et al, 2015. Efficient visible-light-driven Z-scheme overall water splitting using a $MgTa_2O_6$− xNy/TaON heterostructure photocatalyst for H_2 evolution. Angew. Chem. 127 (29), 8618–8621.
Chen, J. et al, 2015. Nitrogen-doped CeOx nanoparticles modified graphitic carbon nitride for enhanced photocatalytic hydrogen production. Green Chem. 17 (1), 509–517.
Chen, F. et al, 2017. Facile synthesis and enhanced photocatalytic H_2-evolution performance of NiS_2-modified g-C_3N_4 photocatalysts. Chin. J. Catal. 38 (2), 296–304.
Chen, X. et al, 2018. Photocatalytic fixation of nitrogen to ammonia: state-of-the-art advancements and future prospects. Mater. Horiz. 5 (1), 9–27.
Chen, X., Mao, S.S., 2007. Titanium dioxide nanomaterials: synthesis, properties, modifications, and applications. Chem. Rev. 107 (7), 2891–2959.
Chen, D., Zhang, X., Lee, A.F., 2015. Synthetic strategies to nanostructured photocatalysts for CO_2 reduction to solar fuels and chemicals. J. Mater. Chem. A 3.
Chen, D., Zhang, X., Lee, A.F., 2015. Synthetic strategies to nanostructured photocatalysts for CO_2 reduction to solar fuels and chemicals. J. Mater. Chem. A 3 (28), 14487–14516.
Cheng, C. et al, 2017. WO_3/g-C_3N_4 composites: one-pot preparation and enhanced photocatalytic H_2 production under visible-light irradiation. Nanotechnology 28 (16), 164002.
Child, M. et al, 2018. Sustainability guardrails for energy scenarios of the global energy transition. Renew. Sustain. Energy Rev. 91, 321–334.
Claus, P. et al, 2000. Supported gold nanoparticles from quantum dot to mesoscopic size scale: effect of electronic and structural properties on catalytic hydrogenation of conjugated functional groups. J. Am. Chem. Soc. 122 (46), 11430–11439.
Cui, L. et al, 2018. Constructing highly uniform onion-ring-like graphitic carbon nitride for efficient visible-light-driven photocatalytic hydrogen evolution. ACS Nano. acsnano.8b01271.
Dai, H. et al, 2013. Synthesis and characterization of graphitic carbon nitride sub-microspheres using microwave method under mild condition. Diam. Relat. Mater. 38, 109–117.
Daniel, M.-C., Astruc, D., 2004. Gold nanoparticles: assembly, supramolecular chemistry, quantum-size-related properties, and applications toward biology, catalysis, and nanotechnology. Chem. Rev. 104 (1), 293–346.
Di, Y. et al, 2010. Making metal carbon nitride heterojunctions for improved photocatalytic hydrogen evolution with visible light. ChemCatChem 2 (7), 834–838.
Di, J. et al, 2016. Carbon-nanotube fibers for wearable devices and smart textiles. Adv. Mater. 28 (47), 10529–10538.
Di, T. et al, 2017. A direct Z-scheme g-C_3N_4/SnS_2 photocatalyst with superior visible-light CO_2 reduction performance. J. Catal. 352, 532–541.
Dong, G. et al, 2014. A fantastic graphitic carbon nitride (g-C_3N_4) material: electronic structure, photocatalytic and photoelectronic properties. J. Photochem. Photobiol., C 20, 33–50.
Dong, F. et al, 2015. A general method for type I and type II g-C_3N_4/g-C_3N_4 metal-free isotype heterostructures with enhanced visible light photocatalysis. New J. Chem. 39 (6), 4737–4744.
Dong et al, 2016. Effective photocatalytic H2O2 production under visible light irradiation at g-C3N4 modulated by carbon vacancies. Appl. Catal. B Environ. Int. J. Devot. Catal. Sci. Appl.
Dong, G. et al, 2017. Carbon vacancy regulated photoreduction of NO to N_2 over ultrathin g-C_3N_4 nanosheets. Appl. Catal. B 218, 515–524.
Dong, G., Ho, W., Wang, C., 2015. Selective photocatalytic N_2 fixation dependent on g-C_3N_4 induced by nitrogen vacancies. J. Mater. Chem. A 3 (46), 23435–23441.
Ehsan, M.F. et al, 2020. Reactive oxygen species: New insights into photocatalytic pollutant degradation over g-C_3N_4/ZnSe nanocomposite. Appl. Surf. Sci. 532, 147418.
Essekri, A. et al, 2020. Enhanced adsorptive removal of crystal violet dye from aqueous media using citric acid modified red-seaweed: experimental study combined with RSM process optimization. J. Disper Sci. Technol., 1–14
Essekri, A. et al, 2021. Novel citric acid-functionalized brown algae with a high removal efficiency of crystal violet dye from colored

wastewaters: insights into equilibrium, adsorption mechanism, and reusability. Int. J. Phytorem. 23 (4), 336–346.
Fang, S. et al, 2016. Effect of carbon-dots modification on the structure and photocatalytic activity of g-C_3N_4. Appl. Catal. B 185, 225–232.
Fang, L.J. et al, 2017. Facile fabrication of large-aspect-ratio g-C_3N_4 nanosheets for enhanced photocatalytic hydrogen evolution. ACS Sustain. Chem. Eng. 5 (3), 2039–2043.
Fattakhova-Rohlfing, D., Zaleska, A., Bein, T., 2014. Three-dimensional titanium dioxide nanomaterials. Chem. Rev. 114 (19), 9487–9558.
Faunce, T. et al, 2013. Artificial photosynthesis as a frontier technology for energy sustainability. Energy Environ. Sci. 6 (4), 1074–1076.
Faunce, T.A. et al, 2013. Artificial Photosynthesis as a Frontier Technology for Energy Sustainability. Social Science Electronic Publishing.
Feng, Z. et al, 2017. In situ preparation of Z-scheme MoO_3/g-C_3N_4 composite with high performance in photocatalytic CO_2 reduction and RhB degradation. J. Mater. Res. 32 (19), 3660–3668.
Frank, S.N., Bard, A.J., 1977. Heterogeneous photocatalytic oxidation of cyanide and sulfite in aqueous solutions at semiconductor powders. J. Phys. Chem. 81 (15), 1484–1488.
Frank, S.N., Bard, A.J., 1977. Heterogeneous photocatalytic oxidation of cyanide ion in aqueous solutions at titanium dioxide powder. Cheminform 8 (14), 303–304.
Fu, J. et al, 2017. Hierarchical porous O-doped g-C_3N_4 with enhanced photocatalytic CO2 reduction activity. Small 13 (15), 1603938.
Fu, J. et al, 2018. g-C_3N_4-Based heterostructured photocatalysts. Adv. Energy Mater. 8 (3), 1701503.
Fujishima, A., Honda, K., 1972. Electrochemical photolysis of water at a semiconductor electrode. Nature 238 (5358), 37–38.
Fujishima, A., Zhang, X., Tryk, D.A., 2008. TiO_2 photocatalysis and related surface phenomena. Surf. Sci. Rep. 63 (12), 515–582.
Gao, J. et al, 2015. One-pot synthesis of copper-doped graphitic carbon nitride nanosheet by heating Cu–melamine supramolecular network and its enhanced visible-light-driven photocatalysis. J. Solid State Chem. 228, 60–64.
Gao, G. et al, 2016. Single atom (Pd/Pt) supported on graphitic carbon nitride as an efficient photocatalyst for visible-light reduction of carbon dioxide. J. Am. Chem. Soc. 138 (19), 6292–6297.
Gaya, U.I., Abdullah, A.H., 2008. Heterogeneous photocatalytic degradation of organic contaminants over titanium dioxide: a review of fundamentals, progress and problems. J. Photochem. Photobiol., C 9 (1), 1–12.
Ge, L. et al, 2012. Synthesis and efficient visible light photocatalytic hydrogen evolution of polymeric g-C_3N_4 coupled with CdS quantum dots. J. Phys. Chem. C 116 (25), 13708–13714.
Ge, J. et al, 2020. Nitrogen photofixation on holey g-C_3N_4 nanosheets with carbon vacancies under visible-light irradiation. Chin. Chem. Lett. 31 (3), 792–796.
Ghufran, S. et al, 2021. Biochemical analysis of root exudates of canola plant in response to chemical and physical abiotic stress. Other Conferences.
Gu, Q. et al, 2015. Temperature-controlled morphology evolution of graphitic carbon nitride nanostructures and their photocatalytic activities under visible light. RSC Adv. 5 (61), 49317–49325.
Gu, Q. et al, 2015. Template-free synthesis of porous graphitic carbon nitride microspheres for enhanced photocatalytic hydrogen generation with high stability. Appl. Catal. B 165, 503–510.
Habisreutinger, S.N., Schmidt-Mende, L., Stolarczyk, J.K., 2013. Photocatalytic reduction of CO_2 on TiO_2 and other semiconductors. Angew. Chem. Int. Ed. 52 (29), 7372–7408.
Hamid, A. et al, 2020. Probing the physio-chemical appraisal of green synthesized PbO nanoparticles in PbO-PVC nanocomposite polymer membranes. Spectrochim. Acta Part A Mol. Biomol. Spectrosc. 235, 118303.
Han, Q. et al, 2015. One-step preparation of iodine-doped graphitic carbon nitride nanosheets as efficient photocatalysts for visible light water splitting. J. Mater. Chem. A 3 (8), 4612–4619.
Han, C. et al, 2015. AuPd bimetallic nanoparticles decorated graphitic carbon nitride for highly efficient reduction of water to H_2 under visible light irradiation. Carbon 92, 31–40.
Han, Q. et al, 2016. Atomically thin mesoporous nanomesh of graphitic C_3N_4 for high-efficiency photocatalytic hydrogen evolution. ACS Nano 10 (2), 2745–2751.
Han, Q. et al, 2016. Atomically thin mesoporous nanomesh of graphitic C_3N_4 for high-efficiency photocatalytic hydrogen evolution. ACS Nano 10 (2), 2745–2751.
Han, Z. et al, 2017. The band structure and photocatalytic mechanism for a CeO_2-modified g-C_3N_4 photocatalyst. New J. Chem. 41 (18), 9724–9730.
Hao, Q. et al, 2018. A separation-free polyacrylamide/bentonite/graphitic carbon nitride hydrogel with excellent performance in water treatment. J. Cleaner Prod. 197, 1222–1230.
Hao, D. et al, 2020. Surface defect-abundant one-dimensional graphitic carbon nitride nanorods boost photocatalytic nitrogen fixation. New J. Chem. 44 (47), 20651–20658.
Hao, D. et al, 2021. A reusable, separation-free and biodegradable calcium alginate/g-C_3N_4 microsphere for sustainable photocatalytic wastewater treatment. J. Cleaner Prod. 314, 128033.
Hao, D. et al, 2021. Emerging artificial nitrogen cycle processes through novel electrochemical and photochemical synthesis. Mater. Today 46, 212–233.
Hao, D. et al, 2021. 2021.. A green synthesis of Ru modified g-C_3N_4 nanosheets for enhanced photocatalytic ammonia synthesis. Energy Mater. Adv. 2021.
Hasija, V. et al, 2019. Recent advances in noble metal free doped graphitic carbon nitride based nanohybrids for photocatalysis of organic contaminants in water: a review. Appl. Mater. Today 15, 494–524.
Hayat, A. et al, 2019. Rational Ionothermal copolymerization of TCNQ with PCN semiconductor for enhanced Photocatalytic full water splitting. ACS Appl. Mater. Interf. 11 (50), 46756–46766.
Hayat, A. et al, 2019. Visible-light enhanced photocatalytic performance of polypyrrole/g-C_3N_4 composites for water splitting to evolve H_2 and pollutants degradation. J. Photochem. Photobiol., A 379, 88–98.
Hayat, A. et al, 2019. Fusion of conjugated bicyclic co-polymer within polymeric carbon nitride for high photocatalytic performance. J. Colloid Interface Sci. 554, 627–639.
Hayat, A. et al, 2019. Nickel oxide nano-particles on 3D nickel foam substrate as a non-enzymatic glucose sensor. J. Electrochem. Soc. 166 (15), B1602–B1611.
Hayat, A. et al, 2019. Synthesis and optimization of the trimesic acid modified polymeric carbon nitride for enhanced photocatalytic reduction of CO_2. J. Colloid Interf. Sci. 548, 197–205.
Hayat, A. et al, 2020. Molecular engineering of polymeric carbon nitride based Donor-Acceptor conjugated copolymers for enhanced photocatalytic full water splitting. J. Colloid Interface Sci. 560, 743–754.
Hayat, A. et al, 2021. π-deficient pyridine ring-incorporated carbon nitride polymers for photocatalytic H2 evolution and CO_2 fixation. Res. Chem. Intermed. 47 (1), 15–27.
Hayat, A. et al, 2021. Molecular engineering of carbon nitride towards photocatalytic H_2 evolution and dye degradation. J. Colloid Interface Sci. 597, 39–47.
Hayat, A. et al, 2021. Organic conjugation of polymeric carbon nitride for improved photocatalytic CO_2 conversion and H_2 fixation. Energy Technol. 9 (10), 2100091.
Hayat, A. et al, 2021. Molecular grafting based polymeric carbon nitride for wondrous artificial photosynthesis. Int. J. Energy Res.
Hayat, A. et al, 2021. Organic heterostructure modified carbon nitride as apprehension for Quercetin Biosensor. Synth. Met. 278, 116813.

Hayat, A. et al, 2021. A superficial intramolecular alignment of carbon nitride through conjugated monomer for optimized photocatalytic CO_2 reduction. Catalysts 11 (8), 935.
Hayat, A. et al, 2021. A simplistic molecular agglomeration of carbon nitride for optimized photocatalytic performance. Surf. Interf. 25, 101166.
Hayat, A. et al, 2021. A butterfly shaped organic heterojunction photocatalyst for effective photocatalytic CO_2 reduction. CrystEngComm 23 (28), 4963–4974.
Hayat, A. et al, 2021. A molecular amalgamation of carbon nitride polymer as emphasized photocatalytic performance. Int. J. Energy Res. 45 (14), 19921–19928.
Hayat, A. et al, 2022. Enhanced photocatalytic overall water splitting from an assembly of donor-π-acceptor conjugated polymeric carbon nitride. J. Colloid Interf. Sci. 624, 411–422.
Hayat, A. et al, 2022. Graphitic carbon nitride (g–C3N4)–based semiconductor as a beneficial candidate in photocatalysis diversity. Int. J. Hydrogen Energy 47 (8), 5142–5191.
Hayat, A. et al, 2022. Biomass lignin integrated polymeric carbon nitride for boosted photocatalytic hydrogen and oxygen evolution reactions. Mole. Catal. 518, 112064.
Hayat, A. et al, 2022. Fabrication, characteristics, and applications of boron nitride and their composite nanomaterials. Surf. Interf. 29, 101725.
Hayat, A. et al, 2022. Recent advancement of the current aspects of g-C3N4 for its photocatalytic applications in sustainable energy system. Chem. Rec.
Hayat, A. et al, 2022. State of the art advancement in rational design of g-C3N4 photocatalyst for efficient solar fuel transformation, environmental decontamination and future perspectives. Int. J. Hydrogen Energy 47 (20), 10837–10867.
Hayat, A. et al, 2022. Molecular grafting based polymeric carbon nitride for wondrous artificial photosynthesis. Int. J. Energy Res. 46 (2), 1882–1893.
Hayat, A. et al, 2022. Molecular engineering control defects within carbon nitride for optimized co-catalyst Pt induced photocatalytic CO_2 reduction and NO_2 oxidation reaction. Int. J. Hydrogen Energy 47 (31), 14280–14293.
Hayat, A., Li, T., 2019. A facile supramolecular aggregation of trithiocyanuric acid with PCN for high photocatalytic hydrogen evolution from water splitting. Int. J. Energy Res. 43 (10), 5479–5492.
He, Y. et al, 2015. New application of Z-scheme Ag3PO4/g-C_3N_4 composite in converting CO_2 to fuel. Environ. Sci. Technol. 49 (1), 649–656.
He, Y. et al, 2015. Z-scheme SnO_2− x/g-C_3N_4 composite as an efficient photocatalyst for dye degradation and photocatalytic CO_2 reduction. Sol. Energy Mater. Sol. Cells 137, 175–184.
He, Y. et al, 2015. High-efficiency conversion of CO_2 to fuel over ZnO/g-C_3N_4 photocatalyst. Appl. Catal. B 168, 1–8.
He, K. et al, 2016. Treatment of alkaline stripped effluent in aerated constructed wetlands: feasibility evaluation and performance enhancement. Water 8 (9), 386.
Hernández-Alonso, M. et al, 2009. Development of alternative photocatalysts to TiO_2. Challeng. Opport. 2 (12), 1231.
Herron, J.A. et al, 2015. A general framework for the assessment of solar fuel technologies. Energy Environ. Sci. 8 (1), 126–157.
Ho, W. et al, 2018. Carbon vacancy-induced enhancement of the visible light-driven photocatalytic oxidation of NO over g-C_3N_4 nanosheets. Appl. Surf. Sci.
Hong, J. et al, 2014. Porous carbon nitride nanosheets for enhanced photocatalytic activities. Nanoscale 6 (24), 14984–14990.
Hou, Y. et al, 2013. Layered nanojunctions for hydrogen-evolution catalysis. Angew. Chem. Int. Ed. 52 (13), 3621–3625.
Hou, Y. et al, 2013. Layered nanojunctions for hydrogen-evolution catalysis. Angew. Chem. 125 (13), 3709–3713.
Hou, Y. et al, 2014. N-doped graphene/porous g-C_3N_4 nanosheets supported layered-MoS_2 hybrid as robust anode materials for lithium-ion batteries. Nano Energy 8, 157–164.
Hsini, A. et al, 2020. Synthesis and characterization of arginine-doped polyaniline/walnut shell hybrid composite with superior clean-up ability for chromium (VI) from aqueous media: equilibrium, reusability and process optimization. J. Mol. Liq. 316, 113832.
Hsini, A. et al, 2021. Facile synthesis and characterization of a novel 1,2,4,5-benzene tetracarboxylic acid doped polyaniline@zinc phosphate nanocomposite for highly efficient removal of hazardous hexavalent chromium ions from water. J. Colloid. Interf. Sci. 585, 560–573.
Hu, S. et al, 2016. Construction of a 2D/2D g-C_3N_4/rGO hybrid heterojunction catalyst with outstanding charge separation ability and nitrogen photofixation performance via a surface protonation process. RSC Adv. 6 (31), 25695–25702.
Hu, Z. et al, 2019. Construction of carbon-doped supramolecule-based g-C_3N_4/TiO_2 composites for removal of diclofenac and carbamazepine: a comparative study of operating parameters, mechanisms, degradation pathways. J. Hazard. Mater. 380, 120812.
Hu, L., Peng, Q., Li, Y., 2008. Selective synthesis of Co_3O_4 nanocrystal with different shape and crystal plane effect on catalytic property for methane combustion. J. Am. Chem. Soc. 130 (48), 16136–16137.
Huang, Y. et al, 2015. Preparation of 2D hydroxyl-rich carbon nitride nanosheets for photocatalytic reduction of CO_2. RSC Adv. 5 (42), 33254–33261.
Huang, Q. et al, 2015. Efficient photocatalytic reduction of CO_2 by amine-functionalized g-C_3N_4. Appl. Surf. Sci. 358, 350–355.
Huang, Z.-F. et al, 2015. Carbon nitride with simultaneous porous network and O-doping for efficient solar-energy-driven hydrogen evolution. Nano Energy 12, 646–656.
Huang, Q. et al, 2021. Ultralight biodegradable 3D-g-C_3N_4 aerogel for advanced oxidation water treatment driven by oxygen delivery channels and triphase interfaces. J. Cleaner Prod. 288, 125091.
Huang, J., Ho, W., Wang, X., 2014. Metal-free disinfection effects induced by graphitic carbon nitride polymers under visible light illumination. Chem. Commun. 50 (33), 4338–4340.
Inoue, T. et al, 1979. Photoelectrocatalytic reduction of carbon dioxide in aqueous suspensions of semiconductor powders. Nature.
Inoue, T. et al, 1979. Photoelectrocatalytic reduction of carbon dioxide in aqueous suspensions of semiconductor powders. Nature 277 (5698), 637–638.
Jariwala, D. et al, 2013. Carbon nanomaterials for electronics, optoelectronics, photovoltaics, and sensing. Chem. Soc. Rev. 42 (7), 2824–2860.
Jh, A. et al, 2020. Ultrathin Ag2WO4-coated P-doped g-C3N4 nanosheets with remarkable photocatalytic performance for indomethacin degradation-Science Direct. J. Hazardous Mater. 392.
Ji et al, 2017. Large scale synthesis of porous carbon-nitride microsphere for visible light harvesting. Mater. Sci. Forum.
Jiang, D. et al, 2015. Two-dimensional $CaIn_2S_4$/g-C_3N_4 heterojunction nanocomposite with enhanced visible-light photocatalytic activities: interfacial engineering and mechanism insight. ACS Appl. Mater. Interf. 7 (34), 19234–19242.
Jiang, W. et al, 2016. Polyaniline/carbon nitride nanosheets composite hydrogel: a separation-free and high-efficient photocatalyst with 3D hierarchical structure. Small 12 (32), 4370–4378.
Jin, A. et al, 2017. Efficient photocatalytic hydrogen evolution on band structure tuned polytriazine/heptazine based carbon nitride heterojunctions with ordered needle-like morphology achieved by an in situ molten salt method. J. Phys. Chem. C 121 (39), 21497–21509.

Jing, D., Guo, L., 2006. A novel method for the preparation of a highly stable and active CdS photocatalyst with a special surface nanostructure. J. Phys. Chem. B 110 (23), 11139.
Jo, W.-K. et al, 2017. Cobalt promoted TiO_2/GO for the photocatalytic degradation of oxytetracycline and Congo Red. Appl. Catal. B 201, 159–168.
Jun, Y.S. et al, 2013. From melamine-cyanuric acid supramolecular aggregates to carbon nitride hollow spheres. Adv. Funct. Mater. 23 (29), 3661–3667.
Kamat, P.V., 2007. Meeting the clean energy demand: nanostructure architectures for solar energy conversion. J. Phys. Chem. C 111 (7), 2834–2860.
Karamian, E., Sharifnia, S., 2016. On the general mechanism of photocatalytic reduction of CO2. J. CO_2 Utiliz. 16, 194–203.
Kato, H., Kudo, A., 2001. Water splitting into H_2 and O_2 on alkali tantalate photocatalysts $ATaO_3$ (A = Li, Na, and K). J. Phys. Chem. B.
Kato, H., Kudo, A., 2001. Water splitting into H_2 and O_2 on alkali tantalate photocatalysts $ATaO_3$ (A= Li, Na, and K). J. Phys. Chem. B 105 (19), 4285–4292.
Khan, M. et al, 2018. Comparative study of the ball milling and acid treatment of functionalized nanodiamond composites. Int. J. Refract Metal Hard Mater. 73, 46–52.
Khan, J. et al, 2019. Multi-dimensional anatase TiO_2 materials: synthesis and their application as efficient charge transporter in perovskite solar cells. Sol. Energy 184, 323–330.
Khan, M. et al, 2020. Functionalized nano diamond composites for photocatalytic hydrogen evolution and effective pollutant degradation. Int. J. Hydrogen Energy 45 (53), 29070–29081.
Khan, M. et al, 2020. Surface optimization of detonation nanodiamonds for the enhanced mechanical properties of polymer/nanodiamond composites. Diam. Relat. Mater. 107, 107897.
Khan, M. et al, 2021. A concise review on the elastomeric behavior of electroactive polymer materials. Int. J. Energy Res. 45 (10), 14306–14337.
Khan, M. et al, 2021. Synergistic effect of nanodiamond and titanium oxide nanoparticles on the mechanical, thermal and electrical properties of pitch-derived carbon foam composites. Polym. Int. 70 (12), 1733–1740.
Kizito, S. et al, 2017. Treatment of anaerobic digested effluent in biochar-packed vertical flow constructed wetland columns: Role of media and tidal operation. Sci. Total Environ. 592, 197–205.
Kizito, S. et al, 2017. Phosphate recovery from liquid fraction of anaerobic digestate using four slow pyrolyzed biochars: dynamics of adsorption, desorption and regeneration. J. Environ. Manage. 201, 260–267.
Kongto, P. et al, 2022. Intensive exploration of the fuel characteristics of biomass and biochar from oil palm trunk and oil palm fronds for supporting increasing demand of solid biofuels in Thailand. Energy Rep. 8, 5640–5652.
Kubacka, A., Fernandez-Garcia, M., Colon, G., 2012. Advanced nanoarchitectures for solar photocatalytic applications. Chem. Rev. 112 (3), 1555–1614.
Kubacka, A., Fernández-García, M., Colón, G., 2016. Advanced nanoarchitectures for solar photocatalytic applications. Chem. Rev. 112 (3), 1555–1614.
Kumar, B. et al, 2012. Photochemical and photoelectrochemical reduction of CO_2. Annu. Rev. Phys. Chem. 63, 541–569.
Kumar, S. et al, 2013. Synthesis of magnetically separable and recyclable g-C_3N_4–Fe_3O_4 hybrid nanocomposites with enhanced photocatalytic performance under visible-light irradiation. J. Phys. Chem. C 117 (49), 26135–26143.
Kumar, S. et al, 2014. Cost-effective and eco-friendly synthesis of novel and stable N-doped ZnO/g-C_3N_4 core–shell nanoplates with excellent visible-light responsive photocatalysis. Nanoscale 6 (9), 4830–4842.
Kumar, S. et al, 2016. Facile synthesis of hierarchical Cu_2O nanocubes as visible light photocatalysts. Appl. Catal. B 189, 226–232.
Kumar, S.G., Devi, L.G., 2011. Review on modified TiO_2 photocatalysis under UV/visible light: selected results and related mechanisms on interfacial charge carrier transfer dynamics. J. Phys. Chem. A 115 (46), 13211–13241.
Kuriki, R. et al, 2015. Visible-light-driven CO_2 reduction with carbon nitride: enhancing the activity of ruthenium catalysts. Angew. Chem. Int. Ed. Engl. 54 (8), 2406–2409.
Lamkhao, S., Randorn, C., 2017. Self-initiated photocatalytic polymerization of tough and flexible polyacrylamide hydrogel/polymeric semiconductor g-C_3N_4 composites. J. Photopolym. Sci. Technol. 30 (4), 425–429.
Lang, X., Chen, X., Zhao, J., 2014. Heterogeneous visible light photocatalysis for selective organic transformations. Chem. Soc. Rev. 43 (1), 473–486.
Lee, E.Z. et al, 2010. Cubic mesoporous graphitic carbon (IV) nitride: an all-in-one chemosensor for selective optical sensing of metal ions. Angew. Chem. 122 (50), 9900–9904.
Lee, K.M. et al, 2016. Recent developments of zinc oxide based photocatalyst in water treatment technology: a review. Water Res. 88 (JAN.1), 428–448.
Lee, K.M. et al, 2016. Recent developments of zinc oxide based photocatalyst in water treatment technology: a review. Water Res. 88, 428–448.
Lewis, N.S., Nocera, D.G., 2006. Powering the planet: Chemical challenges in solar energy utilization. Proc. Natl. Acad. Sci. 103 (43), 15729–15735.
Li, L. et al, 2007. Template-free synthesis and photocatalytic properties of novel Fe_2O_3 hollow spheres. J. Phys. Chem. C 111 (5), 2123–2127.
Li, Y. et al, 2009. A simple template-free synthesis of nanoporous ZnS–In_2S_3–Ag_2S solid solutions for highly efficient photocatalytic H_2 evolution under visible light. Chem. Commun. 15, 2020–2022.
Li, H. et al, 2015. Intercorrelated superhybrid of AgBr supported on g-C_3N_4 decorated nitrogen-doped graphene: high engineering photocatalytic activities for water purification and CO_2 reduction. Adv. Mater. 27 (43), 6906–6913.
Li, F.t. et al, 2015. Structure modification function of g-C3N4 for Al2O3 in the in situ hydrothermal process for enhanced photocatalytic activity. Chem. – A Eur. J. 21 (28), 10149–10159.
Li, X. et al, 2015. Hydrogenated defects in graphitic carbon nitride nanosheets for improved photocatalytic hydrogen evolution. J. Phys. Chem. C 119 (27), 14938–14946.
Li, M. et al, 2015. Highly selective CO_2 photoreduction to CO over g-C_3N_4/Bi_2WO6 composites under visible light. J. Mater. Chem. A 3 (9), 5189–5196.
Li, M. et al, 2016. Mesostructured CeO_2/g-C_3N_4 nanocomposites: remarkably enhanced photocatalytic activity for CO_2 reduction by mutual component activations. Nano Energy 19, 145–155.
Li, S. et al, 2016. Effective photocatalytic H_2O_2 production under visible light irradiation at g-C_3N_4 modulated by carbon vacancies. Appl. Catal. B 190, 26–35.
Li, K. et al, 2017. Carbon nitride nanodots decorated brookite TiO_2 quasi nanocubes for enhanced activity and selectivity of visible-light-driven CO_2 reduction. Appl. Catal. B 203, 910–916.
Li, M. et al, 2017. Core-shell $LaPO_4$/g-C_3N_4 nanowires for highly active and selective CO_2 reduction. Appl. Catal. B 201, 629–635.
Li, H. et al, 2017. Fabrication of heterostructured g-C_3N_4/Ag-TiO_2 hybrid photocatalyst with enhanced performance in photocatalytic conversion of CO_2 under simulated sunlight irradiation. Appl. Surf. Sci. 402, 198–207.
Li, J. et al, 2018. The spatially oriented charge flow and photocatalysis mechanism on internal van der Waals heterostructures enhanced g-C_3N_4. ACS Catal. 8 (9), 8376–8385.
Li, X. et al, 2018. Efficient photocatalytic fixation of N_2 by KOH-treated g-C_3N_4. J. Mater. Chem. A 6 (7), 3005–3011.
Li, Y. et al, 2020. 2D g-C_3N_4 for advancement of photo-generated carrier dynamics: status and challenges. Mater. Today 41, 270–303.

Li, Y. et al, 2020. C_3N_4 with engineered three coordinated (N_3C) nitrogen vacancy boosts the production of 1O2 for Efficient and stable NO photo-oxidation. Chem. Eng. J. 389, 124421.
Li, W. et al, 2022. Recent progress in g–C_3N_4–Based materials for remarkable photocatalytic sustainable energy. Int. J. Hydrogen Energy 47 (49), 21067–21118.
Li, Z., Kong, C., Lu, G., 2016. Visible photocatalytic water splitting and photocatalytic two-electron oxygen formation over Cu-and Fe-doped g-C_3N_4. J. Phys. Chem. C 120 (1), 56–63.
Li, Y.-F., Liu, Z.-P., 2011. Particle size, shape and activity for photocatalysis on titania anatase nanoparticles in aqueous surroundings. J. Am. Chem. Soc. 133 (39), 15743–15752.
Li, X., Masters, A.F., Maschmeyer, T., 2015. Photocatalytic hydrogen evolution from silica-templated polymeric graphitic carbon nitride–is the surface area important? ChemCatChem 7 (1), 121–126.
Li, X.-H., Wang, X., Antonietti, M., 2012. Mesoporous g-C_3N_4 nanorods as multifunctional supports of ultrafine metal nanoparticles: hydrogen generation from water and reduction of nitrophenol with tandem catalysis in one step. Chem. Sci. 3 (6), 2170–2174.
Liang, Q. et al, 2015. Macroscopic 3D porous graphitic carbon nitride monolith for enhanced photocatalytic hydrogen evolution. Adv. Mater. 27 (31), 4634–4639.
Liang, Q. et al, 2016. Holey graphitic carbon nitride nanosheets with carbon vacancies for highly improved photocatalytic hydrogen production. Adv. Funct. Mater. 25 (44), 6885–6892.
Liang, L. et al, 2019. Synthesis and photo-catalytic activity of porous g-C_3N_4: Promotion effect of nitrogen vacancy in H_2 evolution and pollutant degradation reactions. Int. J. Hydrogen Energy 44 (31).
Liang, Y. et al, 2019. A g-C_3N_4@ppy-rGO 3D structure hydrogel for efficient photocatalysis. Appl. Surf. Sci. 466, 666–672.
Liang, Q. et al, 2020. In situ growth of CdS quantum dots on phosphorus-doped carbon nitride hollow tubes as active 0D/1D heterostructures for photocatalytic hydrogen evolution. J. Colloid Interface Sci. 577, 1–11.
Liang, H., Zou, H., Hu, S., 2017. Preparation of the W 18 O 49/g-C_3N_4 heterojunction catalyst with full-spectrum-driven photocatalytic N $_2$ photofixation ability from the UV to near infrared region. New J. Chem. 41 (17), 8920–8926.
Liang, X., et al., 2018. Graphitic Carbon Nitride with Carbon Vacancies for Photocatalytic Degradation of Bisphenol A.
Lin, J., Pan, Z., Wang, X., 2014. Photochemical reduction of CO_2 by graphitic carbon nitride polymers. ACS Sustain. Chem. Eng. 2 (3), 353–358.
Listorti, A., Durrant, J., Barber, J., 2009. Solar to fuel. Nat. Mater. 8 (12), 929–930.
Liu, L. et al, 2015. Stable Cu_2O@ g-C_3N_4 core@ shell nanostructures: efficient visible-light photocatalytic hydrogen evolution. Mater. Lett. 158, 278–281.
Liu, Q. et al, 2016. Ultrathin g-C_3N_4 nanosheets coupled with carbon nanodots as 2D/0D composites for efficient photocatalytic H_2 evolution. Appl. Catal. B 193, 248–258.
Liu, G. et al, 2016. In situ bond modulation of graphitic carbon nitride to construct p–n homojunctions for enhanced photocatalytic hydrogen production. Adv. Funct. Mater. 26 (37), 6822–6829.
Liu, H. et al, 2017. Novel visible-light-driven $CdIn_2S_4$/mesoporous g-C_3N_4 hybrids for efficient photocatalytic reduction of CO_2 to methanol. Mole. Catal. 430, 9–19.
Liu, C. et al, 2017. Intermediate-mediated strategy to horn-like hollow mesoporous ultrathin g-C_3N_4 tube with spatial anisotropic charge separation for superior photocatalytic H_2 evolution. Nano Energy, 738–748.
Liu, W. et al, 2019. Visible-light-driven photocatalytic degradation of diclofenac by carbon quantum dots modified porous g-C_3N_4: Mechanisms, degradation pathway and DFT calculation. Water Res. 151, 8–19.
Liu, X., Liang, B., Li, W., 2020. In situ decoration of SnS quantum dots on the α-SnWO4 nanosheets for superior visible-light photocatalytic performance. Appl. Surf. Sci. 531, 147379.
Liu, X., Ma, R., Zhuang, L., Hu, B., Chen, J., Liu, X., Wang, X., 2021. Recent developments of doped g-C3N4 photocatalysts for the degradation of organic pollutants. Crit. Rev. Env. Sci. Technol. 51 (8), 751–790.
Lu, D. et al, 2017. Highly efficient visible-light-induced photoactivity of Z-scheme g-C_3N_4/Ag/MoS_2 ternary photocatalysts for organic pollutant degradation and production of hydrogen. ACS Sustain. Chem. Eng. 5 (2), 1436–1445.
Lu, Z. et al, 2018. Construction 0D/2D heterojunction by highly dispersed Ni_2P QDs loaded on the ultrathin g-C_3N_4 surface towards superhigh photocatalytic and photoelectric performance. Appl. Catal. B 237, 919–926.
Lu, X., Wang, C., Wei, Y., 2009. One-dimensional composite nanomaterials: synthesis by electrospinning and their applications. Small 5 (21), 2349–2370.
Ma, Y. et al, 2014. Titanium dioxide-based nanomaterials for photocatalytic fuel generations. Chem. Rev. 114 (19), 9987–10043.
Maeda, K., 2011. Photocatalytic water splitting using semiconductor particles: history and recent developments. J. Photochem. Photobiol., C 12 (4), 237–268.
Maeda, K. et al, 2014. The effect of the pore-wall structure of carbon nitride on photocatalytic CO_2 reduction under visible light. J. Mater. Chem. A 2 (36), 15146–15151.
Maeda, K., Sekizawa, K., Ishitani, O., 2013. A polymeric-semiconductor–metal-complex hybrid photocatalyst for visible-light CO_2 reduction. Chem. Commun. 49 (86), 10127–10129.
Majeed, S. et al, 2021. Chemical mismanagement and skin burns among hospitalized and outpatient department patients. Int. J. Occupat. Safe. Ergon. 27 (3), 817–830.
Malik, A. et al, 2021. Investigation of textile dyeing effluent using activated sludge system to assess the removal efficiency. Water Environ. Res. 93 (12), 2931–2940.
Mandal, G., Ganguly, T., 2011. Applications of nanomaterials in the different fields of photosciences. Indian J. Phys. 85 (8), 1229–1245.
Mao, J. et al, 2013. Effect of graphitic carbon nitride microstructures on the activity and selectivity of photocatalytic CO_2 reduction under visible light. Catal. Sci. Technol. 3 (5), 1253–1260.
Mao, Z. et al, 2017. Novel g-C_3N_4/CoO nanocomposites with significantly enhanced visible-light photocatalytic activity for H_2 evolution. ACS Appl. Mater. Interf. 9 (14), 12427–12435.
Mao, W. et al, 2018. In-situ construction of coral-like porous P-doped g-C_3N_4 tubes with hybrid 1D/2D architecture and high efficient photocatalytic hydrogen evolution. Appl. Catal. B. S0926337318308671.
Martin, D.J. et al, 2014. Highly efficient photocatalytic H2 evolution from water using visible light and structure-controlled graphitic carbon nitride. Angew. Chem. Int. Ed. 53 (35), 9240–9245.
Matsunaga, T. et al, 1985. Photoelectrochemical sterilization of microbial cells by semiconductor powders. FEMS Microbiol. Lett. 29 (1–2), 211–214.
Mclaren, A. et al, 2009. Shape and size effects of ZnO nanocrystals on photocatalytic activity. J. Am. Chem. Soc. 131 (35), 12540–12541.
Meng, Q. et al, 2018. Integrating both homojunction and heterojunction in QDs self-decorated Bi_2MoO_6/BCN composites to achieve an efficient photocatalyst for Cr (VI) reduction. Chem. Eng. J. 334, 334–343.
Mills, A., Davies, R.H., Worsley, D., 1993. Water purification by semiconductor photocatalysis. Chem. Soc. Rev. 22 (6), 417–425.
Mo, Z., She, X., Li, Y., Liu, L., Huang, L., Chen, Z., Zhang, Q., Xu, H., Li, H., 2015. Synthesis of g-C3N4 at different temperatures for superior visible/UV photocatalytic performance and photoelectrochemical sensing of MB solution. RSC Adv. 5.
Muellner, M.G. et al, 2007. Haloacetonitriles vs. regulated haloacetic acids: are nitrogen-containing DBPs more toxic? Environ. Sci. Technol. 41 (2), 645–651.

Naciri, Y. et al, 2020. Influence of Sr-doping on structural, optical and photocatalytic properties of synthesized $Ca_3(PO_4)_2$. J. Colloid. Interf. Sci. 572, 269–280.

Naciri, Y. et al, 2020. Recent progress on the enhancement of photocatalytic properties of $BiPO_4$ using π–conjugated materials. Adv. Colloid. Interf. Sci. 280, 102160.

Naciri, Y. et al, 2021. Photocatalytic oxidation of pollutants in gas-phase via Ag_3PO_4-based semiconductor photocatalysts: recent progress, new trends, and future perspectives. Criti. Rev. Environ. Sci. Technol., 1–44

Naciri, Y. et al, 2022. Recent advances of bismuth titanate based photocatalysts engineering for enhanced organic contaminates oxidation in water: a review. Chemosphere 300, 134622.

Naseri, A. et al, 2017. Graphitic carbon nitride (g-C_3N_4)-based photocatalysts for solar hydrogen generation: recent advances and future development directions. J. Mater. Chem. A 5 (45), 23406–23433.

Naseri, A. et al, 2017. Graphitic carbon nitride (g-C_3N_4)-based photocatalysts for solar hydrogen generation: recent advances and future development directions. J. Mater. Chem. A 5.

Nguyen, C.C., Vu, N.N., Do, T.-O., 2015. Recent advances in the development of sunlight-driven hollow structure photocatalysts and their applications. J. Mater. Chem. A 3 (36), 18345–18359.

Ni, Z. et al, 2016. New insights into how Pd nanoparticles influence the photocatalytic oxidation and reduction ability of g-C_3N_4 nanosheets. Catal. Sci. Technol. 6 (16), 6448–6458.

Niu, P. et al, 2012. Graphene-like carbon nitride nanosheets for improved photocatalytic activities. Adv. Funct. Mater. 22 (22), 4763–4770.

Niu, P. et al, 2014. Switching the selectivity of the photoreduction reaction of carbon dioxide by controlling the band structure of a g-C_3N_4 photocatalyst. Chem. Commun. 50 (74), 10837–10840.

Nor, N. et al, 2019. Effects of hydrophilic surface macromolecule modifier loading on PES/O-g-C_3N_4 hybrid photocatalytic membrane for phenol removal. Appl. Surf. Sci.

Nosaka, Y., Nosaka, A.Y., 2017. Generation and detection of reactive oxygen species in photocatalysis. Chem. Rev. acs.chemrev.7b00161.

Nosaka, Y., Nosaka, A.Y., 2017. Generation and detection of reactive oxygen species in photocatalysis. Chem. Rev. 117 (17), 11302–11336.

Ohno, T. et al, 2014. Photocatalytic reduction of CO_2 over a hybrid photocatalyst composed of WO_3 and graphitic carbon nitride (g-C_3N_4) under visible light. J. CO_2 Utiliz. 6, 17–25.

Ong, W.J. et al, 2014. Heterojunction engineering of graphitic carbon nitride (g-C_3N_4) via Pt loading with improved daylight-induced photocatalytic reduction of carbon dioxide to methane. Dalton Trans. 44 (3), 1249–1257.

Ong, W.-J. et al, 2015. Graphene oxide as a structure-directing agent for the two-dimensional interface engineering of sandwich-like graphene–g-C_3N_4 hybrid nanostructures with enhanced visible-light photoreduction of CO_2 to methane. Chem. Commun. 51 (5), 858–861.

Ong, W.-J. et al, 2015. Heterojunction engineering of graphitic carbon nitride (g-C_3N_4) via Pt loading with improved daylight-induced photocatalytic reduction of carbon dioxide to methane. Dalton Trans. 44 (3), 1249–1257.

Ong, W.-J. et al, 2016. Heterostructured AgX/g-C_3N_4 (X = Cl and Br) nanocomposites via a sonication-assisted deposition-precipitation approach: emerging role of halide ions in the synergistic photocatalytic reduction of carbon dioxide. Appl. Catal. B 180, 530–543.

Ong, W.-J. et al, 2016. Graphitic carbon nitride (g-C_3N_4)-based photocatalysts for artificial photosynthesis and environmental remediation: are we a step closer to achieving sustainability? Chem. Rev. 116 (12), 7159–7329.

Ong, W.J., Tan, L.L., Ng, Y.H., Yong, S.T., Chai, S.P., 2016. Graphitic carbon nitride (g-C3N4)-based photocatalysts for artificial photosynthesis and environmental remediation: are we a step closer to achieving sustainability? Chem. Rev.

Ou, M. et al, 2017. Single Pt atoms deposition on g-C_3N_4 nanosheets for photocatalytic H2 evolution or NO oxidation under visible light. Int. J. Hydrogen Energy 42 (44), 27043–27054.

Ou, M. et al, 2018. Amino-assisted anchoring of CsPbBr 3 perovskite quantum dots on porous g-$_C3_N4$ for enhanced photocatalytic C_O2 reduction. Angew. Chem. 130 (41), 13758–13762.

Pallavi, A. et al, 2010. A comparative study of photocatalytic activity of some coloured semiconducting oxides. Iran. J. Chem. Chem. Eng.-Int. Engl. Ed. 29 (2), 43–48.

Pan, C. et al, 2012. Dramatic activity of C3N4/BiPO4 photocatalyst with core/shell structure formed by self-assembly. Adv. Funct. Mater. 22 (7), 1518–1524.

Pan, F. et al, 2022. A facile molecular aggregation of isoquinoline based g-C_3N_4 for high photocatalytic performance under visible light illumination. Mater. Res. Bull. 152, 111865.

Pan, C., Zhu, Y., 2010. New type of BiPO(4) oxy-acid salt photocatalyst with high photocatalytic activity on degradation of dye. Environ. Sci. Technol. 44 (14), 5570–5574.

Panneri, S. et al, 2017. Photoregenerable, bifunctional granules of carbon-doped g-C_3N_4 as adsorptive photocatalyst for the efficient removal of tetracycline antibiotic. ACS Sustain. Chem. Eng. 5 (2), 1610–1618.

Pany, S., Parida, K., 2015. A facile in situ approach to fabricate N, S-TiO_2/g-C_3N_4 nanocomposite with excellent activity for visible light induced water splitting for hydrogen evolution. PCCP 17 (12), 8070–8077.

Park, J.H., Park, O.O., Kim, S., 2006. Photoelectrochemical water splitting at titanium dioxide nanotubes coated with tungsten trioxide. Appl. Phys. Lett. 89 (16), 735.

Pramoda, K. et al, 2017. Nanocomposites of C_3N_4 with layers of MoS_2 and nitrogenated RGO, obtained by covalent cross-linking: synthesis, characterization, and HER activity. ACS Appl. Mater. Interf. 9 (12), 10664–10672.

Qadeer, A. et al, 2019. Historically linked residues profile of OCPs and PCBs in surface sediments of typical urban river networks, Shanghai: ecotoxicological state and sources. J. Clean. Prod. 231, 1070–1078.

Qadeer, A. et al, 2020. Concentrations, pollution indices and health risk assessment of heavy metals in road dust from two urbanized cities of Pakistan: comparing two sampling methods for heavy metals concentration. Sustain. Cities. Soc. 53, 101959.

Qadeer, A. et al, 2021. Agricultural plastic mulching as a potential key source of microplastic pollution in the terrestrial ecosystem and consequences. Resour. Conserv. Recycl. 175, 105855.

Qadeer, A. et al, 2022. Rebuttal to comment on "alternative plasticizers as emerging global environmental and health threat: another regrettable substitution?" Focus on DINCH as an example. Environ. Sci. Technol. 56 (8), 5294–5297.

Qadeer, A. et al, 2022. Sustainable development goals under threat? Multidimensional impact of COVID-19 on our planet and society outweigh short term global pollution reduction. Sustain. Cities. Soc., 103962

Qadeer, A. et al, 2022. Alternative plasticizers as emerging global environmental and health threat: another regrettable substitution? Environ. Sci. Technol. 56 (3), 1482–1488.

Qin, J. et al, 2015. Photocatalytic reduction of CO_2 by graphitic carbon nitride polymers derived from urea and barbituric acid. Appl. Catal. B 179, 1–8.

Qin, H. et al, 2020. 0D NiS_2 quantum dots modified 2D g-C_3N_4 for efficient photocatalytic CO_2 reduction. Colloids Surf., A 600, 124912.

Qin, J., Zeng, H., 2017. Photocatalysts fabricated by depositing plasmonic Ag nanoparticles on carbon quantum dots/graphitic carbon nitride for broad spectrum photocatalytic hydrogen generation. Appl. Catal. B 209, 161–173.

QingáLu, G., 2009. Enhanced photocatalytic hydrogen evolution by prolonging the lifetime of carriers in ZnO/CdS heterostructures. Chem. Commun. 23, 3452–3454.
Rahman, M.U., Hayat, A., 2019. Green synthesis, properties, and catalytic application of zeolite (P) in production of biofuels from bagasse. Int. J. Energy Res. 43 (9), 4820–4827.
Ran, J. et al, 2015. Porous P-doped graphitic carbon nitride nanosheets for synergistically enhanced visible-light photocatalytic H_2 production. Energy Environ. Sci. 8 (12), 3708–3717.
Raziq, F. et al, 2017. Synthesis of SnO2/BP codoped g-C_3N_4 nanocomposites as efficient cocatalyst-free visible-light photocatalysts for CO_2 conversion and pollutant degradation. Appl. Catal. B 201, 486–494.
Raziq, F. et al, 2020. Promoting visible-light photocatalytic activities for carbon nitride based 0D/2D/2D hybrid system: beyond the conventional 4-electron mechanism. Appl. Catal. B 270, 118870.
Raziq, F. et al, 2020. Photocatalytic solar fuel production and environmental remediation through experimental and DFT based research on CdSe-QDs-coupled P-doped-g-C_3N_4 composites. Appl. Catal. B 270, 118867.
Rehman, A.U. et al, 2019. Characterisation of magnesium, zinc and iron sulfates for thermochemical storage. Proc. Inst. Civil Eng. – Energy 173 (2), 60–67.
Rehman, A.U. et al, 2021. Thermochemical heat storage ability of $ZnSO_4{\cdot}7H_2O$ as potential long-term heat storage material. Int. J. Energy Res. 45 (3), 4746–4754.
Rehman, A.U. et al, 2021. Paper title: thermochemical heat storage behavior of $ZnSO_4.7H_2O$ under low-temperature. Heat Mass Transf. 57 (5), 765–775.
Reli, M. et al, 2016. Novel TiO_2/g-C_3N_4 photocatalysts for photocatalytic reduction of CO2 and for photocatalytic decomposition of N_2O. J. Phys. Chem. A 120 (43), 8564–8573.
Rhind, S., 2009. Anthropogenic pollutants: a threat to ecosystem sustainability? Philos. Trans. Royal Soc. B: Biol. Sci. 364 (1534), 3391–3401.
Richardson, S.D., Ternes, T.A., 2014. Water analysis: emerging contaminants and current issues. Anal. Chem. 86 (6), 2813–2848.
Rochkind, M. et al, 2014. Using dyes for evaluating photocatalytic properties: a critical review. Molecules 20, 88–110.
Rochkind, M., Pasternak, S., Paz, Y., 2015. Using dyes for evaluating photocatalytic properties: a critical review. Molecules 20 (1), 88–110.
Sakata, T., Kawai, T., 1983. Photosynthesis and photocatalysis with semiconductor powders. Energy Resour. Photochem. Catal., 331–358
Sano, T. et al, 2013. Activation of graphitic carbon nitride (g-C_3N_4) by alkaline hydrothermal treatment for photocatalytic NO oxidation in gas phase. J. Mater. Chem. A 1 (21), 6489–6496.
Santosh et al, 2013. Synthesis of a novel and stable g-C3N4-Ag3PO4 hybrid nanocomposite photocatalyst and study of the photocatalytic activity under visible light irradiation. J. Mater. Chem. A Mater. Energy Sustain.
Schneider, J. et al, 2014. Understanding TiO_2 photocatalysis: mechanisms and materials. Chem. Rev. 114 (19), 9919–9986.
Shaishta, N. et al, 2020. Red-emitting $CaSc_2O_4$:Eu_3^+ phosphor for NUV-based warm white LEDs: structural elucidation and Hirshfeld surface analysis. Int. J. Energy Res. 44 (11), 8328–8339.
Shen, L. et al, 2017. Black TiO_2 nanobelts/g-C_3N_4 nanosheets laminated heterojunctions with efficient visible-light-driven photocatalytic performance. Sci. Rep. 7 (1), 1–11.
Shi, H. et al, 2014. Polymeric g-C_3N_4 coupled with $NaNbO_3$ nanowires toward enhanced photocatalytic reduction of CO_2 into renewable fuel. ACS Catal. 4 (10), 3637–3643.
Shi, H. et al, 2015. Conversion of CO_2 into renewable fuel over Pt–g-C_3N_4/$KNbO_3$ composite photocatalyst. RSC Adv.
Shi, A. et al, 2018. Photocatalytic NH_3 versus H_2 evolution over g-C_3N_4/CsxWO$_3$: O_2 and methanol tipping the scale. Appl. Catal. B 235, 197–206.
Sohail, M. et al, 2017. Synthesis of well-dispersed TiO_2@ reduced graphene oxide (rGO) nanocomposites and their photocatalytic properties. Mater. Res. Bull. 90, 125–130.
Sohail, M. et al, 2018. Synthesis of well-dispersed TiO_2/CNTs@ $CoFe_2O_4$ nanocomposites and their photocatalytic properties. Mater. Res. Bull. 101, 83–89.
Sohail, M. et al, 2020. Synthesis of flower-like Co_9S_8/reduced graphene oxide nanocomposites and their photocatalytic performance. J. Inorg. Organomet. Polym Mater. 30 (12), 5168–5179.
Sohail, M. et al, 2021. Nanostructure engineering via intramolecular construction of carbon nitride as efficient photocatalyst for CO_2 reduction. Nanomaterials 11 (12), 3245.
Sridharan, K. et al, 2015. Silver quantum cluster (Ag9)-grafted graphitic carbon nitride nanosheets for photocatalytic hydrogen generation and dye degradation. Chem. – A Eur. J. 21 (25), 9126–9132.
Styring, S., 2012. Artificial photosynthesis for solar fuels. Faraday Discuss. 155, 357–376.
Styring, S., 2012. Artificial photosynthesis for solar fuels. Faraday Discuss. 155.
Su, S. et al, 2012. Nanomaterials-based sensors for applications in environmental monitoring. J. Mater. Chem. 22 (35), 18101–18110.
Sui, Y. et al, 2013. Dispersed conductive polymer nanoparticles on graphitic carbon nitride for enhanced solar-driven hydrogen evolution from pure water. Nanoscale 5 (19), 9150–9155.
Sun, J. et al, 2012. Bioinspired hollow semiconductor nanospheres as photosynthetic nanoparticles. Nat. Commun. 3 (1), 1139.
Sun, J. et al, 2012. Bioinspired hollow semiconductor nanospheres as photosynthetic nanoparticles. Nat. Commun. 3 (1), 1–7.
Sun, J. et al, 2017. Self-standing carbon nitride-based hydrogels with high photocatalytic activity. ACS Appl. Mater. Interf. 9 (3), 2029–2034.
Sun, Z. et al, 2017. Phase effect of Ni_xP_y hybridized with g-C_3N_4 for photocatalytic hydrogen generation. ACS Appl. Mater. Interf. 9 (36), 30583–30590.
Sun, C. et al, 2021. Synthesis of 0D SnO_2 nanoparticles/2D g-C_3N_4 nanosheets heterojunction: improved charge transfer and separation for visible-light photocatalytic performance. J. Alloys Compd. 871, 159561.
Swelm, W. et al, 2018. Facile synthesis of ternary alloy of CdSe(1–x)S (x) quantum dots with tunable absorption and emission of visible light. Nanomaterials (Basel, Switzerland) 8 (12), 979.
Tada, H. et al, 2006. All-solid-state Z-scheme in CdS–Au–TiO_2 three-component nanojunction system. Nat. Mater. 5 (10), 782–786.
Taha, T.A., Mahmoud, M.H., Hayat, A., 2021. Dielectric relaxation studies on PVC-Pb_3O_4 polymer nanocomposites. J. Mater. Sci.: Mater. Electron. 32 (23), 27666–27675.
Tahir, M. et al, 2013. Tubular graphitic-C_3N_4: a prospective material for energy storage and green photocatalysis. J. Mater. Chem. A 1 (44), 13949–13955.
Tahir, M. et al, 2014. Multifunctional g-C_3N_4 nanofibers: a template-free fabrication and enhanced optical, electrochemical, and photocatalyst properties. ACS Appl. Mater. Interf. 6 (2), 1258–1265.
Tan, K.B. et al, 2015. Adsorption of dyes by nanomaterials: recent developments and adsorption mechanisms. Sep. Purif. Technol. 150, 229–242.
Tang, L. et al, 2017. Fabrication of compressible and recyclable macroscopic g-C_3N_4/GO aerogel hybrids for visible-light harvesting: a promising strategy for water remediation. Appl. Catal. B 219, 241–248.
Tian, J. et al, 2014. Recent progress in design, synthesis, and applications of one-dimensional TiO_2 nanostructured surface heterostructures: a review. Chem. Soc. Rev. 43 (20), 6920–6937.
Tian, N. et al, 2017. Precursor-reforming protocol to 3D mesoporous g-C_3N_4 established by ultrathin self-doped nanosheets for superior hydrogen evolution. Nano Energy 38, 72–81.

Tian, N. et al, 2019. Rational nanostructure design of graphitic carbon nitride for photocatalytic applications. J. Mater. Chem. A 7 (19), 11584–11612.

Tonda, S. et al, 2014. Fe-doped and-mediated graphitic carbon nitride nanosheets for enhanced photocatalytic performance under natural sunlight. J. Mater. Chem. A 2 (19), 6772–6780.

Tong, Z. et al, 2015. Three-dimensional porous aerogel constructed by g-C_3N_4 and graphene oxide nanosheets with excellent visible-light photocatalytic performance. ACS Appl. Mater. Interf. 7 (46), 25693–25701.

Tong, J. et al, 2015. An efficient top-down approach for the fabrication of large-aspect-ratio g-C_3N_4 nanosheets with enhanced photocatalytic activities. PCCP 17 (36), 23532–23537.

Tyborski, T. et al, 2012. Tunable optical transition in polymeric carbon nitrides synthesized via bulk thermal condensation. J. Phys.: Condens. Matter 24 (16), 162201.

Tyborski, T. et al, 2013. Crystal structure of polymeric carbon nitride and the determination of its process-temperature-induced modifications. J. Phys.: Condens. Matter 25 (39), 395402.

Uddin, I. et al, 2021. Conventional and cement-catalyzed co-pyrolysis of rice straw and waste polyethylene into liquid and gaseous fuels by using a fixed bed reactor. Biomass Convers. Biorefin.

Ullah, H. et al, 2016. Preparation, characterization and optoelectronic properties of nanodiamonds doped zinc oxide nanomaterials by a ball milling technique. Mater. Res. Express 3 (7), 075016.

Ullah, A. et al, 2020. Fabrication of polymer carbon nitride with organic monomer for effective photocatalytic hydrogen evolution. J. Photochem. Photobiol., A 401, 112764.

Ullah, I. et al, 2021. Platinum-alumina modified SO_42−-ZrO_2/Al_2O_3 based bifunctional catalyst for significantly improved n-butane isomerization performance. Surf. Interf. 25, 101227.

Venkatathri, N., Kumar, A.A., 2017. Development of porous titanosilicate-based hybrid nanocomposites for photocatalytic applications under UV and solar light irradiation.

Vhna, B. et al, 2021. Corrigendum to "Synthesis, characterization, and photocatalytic performance of Ag/$AgFeO_2$ decorated on g-C_3N_4-nanosheet under the visible light irradiation" [Journal of the Taiwan Institute of Chemical Engineers 115 (2020) 279–292] - ScienceDirect. J. Taiwan Inst. Chem. Eng.

Wageh, S., 2007. Raman and photoluminescence study of CdSe nanoparticles capped with a bifunctional molecule. Physica E 39 (1), 8–14.

Wageh, S. et al, 2013. Preparation and characterization of a novel system of CdS nanoparticles embedded in borophosphate glass matrix. J. Alloys Compd. 555, 161–168.

Wageh, S. et al, 2014. Nano silver-anchored reduced graphene oxide sheets for enhanced dielectric performance of polymer nanocomposites. RSC Adv. 4 (54), 28426–28431.

Wageh, S. et al, 2015. Synthesis and characterization of mercaptoacetic acid capped cadmium sulphide quantum dots. J. Nanosci. Nanotechnol. 15 (12), 9861–9867.

Wageh, S., 2016. Ternary ZnS: Te nanoparticles capped with 3-mercaptopropionic acid prepared in aqueous media. J. Mater. Sci.: Mater. Electron. 27 (10), 10877–10887.

Wageh, S. et al, 2018. Photodiode based on Pb0.9Cd0.1S ternary alloy semiconductor for solar tracking systems. J. Mater. Sci.: Mater. Electron. 29 (19), 16880–16893.

Wageh, S. et al, 2021. Digital printing of a novel electrode for stable flexible organic solar cells with a power conversion efficiency of 8.5%. Sci. Rep. 11 (1), 14212.

Wageh, S. et al, 2021. Silver nanowires digital printing for inverted flexible semi-transparent solar cells. Adv. Eng. Mater. 23 (4), 2001305.

Wageh, S., Higazy, A.A., Hassouna, A.S., 2013. Optical properties and thermal degradation of CdSe capped with 3-mercaptopropionic acid. J. Mater. Sci.: Mater. Electron. 24 (8), 3049–3057.

Wageh, S., Al-Ghamdi, A.A., Yakuphanoglu, F., 2013. Band edge emission of ZnS nanoparticles prepared by excess of thiourea as a source of sulfur. J. Sol-Gel Sci. Technol. 66 (3), 443–451.

Wageh, S., Zhao, S.L., 2019. Ultra-violet electroluminescence of ZnO nanorods/MEH-PPV heterojunctions by optimizing their thickness and using AZO as a transparent conductive electrode. Materials 12, 18.

Wageh, S., Al-Amri, A.M.A., Al-Ghamdi, A., 2016. Effect of adding reducing agent on the structure and optical properties of one-pot preparation method of CdTe quantum dots. J. Mater. Sci.: Mater. Electron. 27 (8), 8384–8393.

Walsh, J.J. et al, 2016. Photochemical CO_2 reduction using structurally controlled gC 3 N 4. PCCP 18 (36), 24825–24829.

Wang, W. et al, 2012. Visible-light photocatalytic activity and deactivation mechanism of Ag_3PO_4 spherical particles. Chem. – Asian J. 7 (8), 1902–1908.

Wang, Y. et al, 2013. Carbon nitride nanosheets for photocatalytic hydrogen evolution: remarkably enhanced activity by dye sensitization. Catal. Sci. Technol. 3 (7), 1703–1711.

Wang, W. et al, 2013. Graphene and g-C_3N_4 nanosheets cowrapped elemental α-sulfur as a novel metal-free heterojunction photocatalyst for bacterial inactivation under visible-light. Environ. Sci. Technol. 47 (15), 8724–8732.

Wang, S. et al, 2014. Controllable synthesis of nanotube-type graphitic C3N4 and their visible-light photocatalytic and fluorescent properties. J. Mater. Chem. A 2 (9), 2885–2890.

Wang, W. et al, 2014. g-C_3N_4 quantum dots: direct synthesis, upconversion properties and photocatalytic application. Chem. Commun. 50 (70), 10148–10150.

Wang, K. et al, 2015. Sulfur-doped g-C3N4 with enhanced photocatalytic CO_2-reduction performance. Appl. Catal. B 176, 44–52.

Wang, Y. et al, 2016. Facile one-step synthesis of hybrid graphitic carbon nitride and carbon composites as high-performance catalysts for CO_2 photocatalytic conversion. ACS Appl. Mater. Interf. 8 (27), 17212–17219.

Wang, H. et al, 2016. Surprisingly advanced CO_2 photocatalytic conversion over thiourea derived g-C_3N_4 with water vapor while introducing 200–420 nm UV light. J. CO_2 Utiliz. 14, 143–151.

Wang, J.-C. et al, 2016. Indirect Z-scheme BiOI/g-C_3N_4 photocatalysts with enhanced photoreduction CO_2 activity under visible light irradiation. ACS Appl. Mater. Interf. 8 (6), 3765–3775.

Wang, K. et al, 2017. 0D/2D Z-scheme heterojunctions of bismuth tantalate quantum dots/ultrathin g-C_3N_4 nanosheets for highly efficient visible light photocatalytic degradation of antibiotics. ACS Appl. Mater. Interf., 43704–43715

Wang, M. et al, 2017. 2D–2D MnO_2/g-C_3N_4 heterojunction photocatalyst: in-situ synthesis and enhanced CO2 reduction activity. Carbon 120, 23–31.

Wang, H. et al, 2017. Boosting hot-electron generation: exciton dissociation at the order–disorder interfaces in polymeric photocatalysts. J. Am. Chem. Soc. 139 (6), 2468–2473.

Wang, Y. et al, 2017. In situ construction of Z-scheme g-C_3N_4/$Mg_{1.1}Al_{0.3}Fe_{0.2}O_{1.7}$ nanorod heterostructures with high N_2 photofixation ability under visible light. Rsc Adv. 7 (29), 18099–18107.

Wang, J. et al, 2017. Facile gel-based morphological control of Ag/g-C_3N_4 porous nanofibers for photocatalytic hydrogen generation. ACS Sustain. Chem. Eng. 5 (11), 10633–10639.

Wang, Y.-J. et al, 2018. Unlocking the door to highly active ORR catalysts for PEMFC applications: polyhedron-engineered Pt-based nanocrystals. Energy Environ. Sci. 11 (2), 258–275.

Wang, C. et al, 2018. 0D/2D $Au_{25}(Cys)_{18}$ nanoclusters/g-C_3N_4 nanosheets composites for enhanced photocatalytic hydrogen production under visible light. ACS Sustain. Chem. Eng. 6 (7).

Wang, W. et al, 2020. 1D porous tubular g-C_3N_4 capture black phosphorus quantum dots as 1D/0D metal-free photocatalysts for oxytetracycline hydrochloride degradation and hexavalent chromium reduction. Appl. Catal. B 273, 119051.

Wang, J. et al, 2021. Sulfur-doped g-C_3N_4/TiO_2 S-scheme heterojunction photocatalyst for Congo Red photodegradation. Chin. J. Catal. 42 (1), 56–68.
Wang, X. et al, 2021. Controllable approach to carbon-deficient and oxygen-doped graphitic carbon nitride: robust photocatalyst against recalcitrant organic pollutants and the mechanism insight. Adv. Funct. Mater. 31 (20), 2010763.
Wang, X., Maeda, K., Thomas, A., Takanabe, K., Xin, G., Carlsson, J.M., Domen, K., Antonietti, M., 2009. A metal-free polymeric photocatalyst for hydrogen production from water under visible light. Nat. mater. 8 (1), 76–80.
Wang, X., Blechert, S., Antonietti, M., 2012. Polymeric graphitic carbon nitride for heterogeneous photocatalysis. ACS Catal. 2 (8), 1596–1606.
Wang, Q., Domen, K., 2019. Particulate photocatalysts for light-driven water splitting: mechanisms, challenges, and design strategies. Chem. Rev. 120 (2).
Wang, W., Xu, P., Chen, M., Zeng, G., Zhang, C., Zhou, C., Yang, Y., Huang, D., Lai, C., Cheng, M., Hu, L., 2018. Alkali metal-assisted synthesis of graphite carbon nitride with tunable band-gap for enhanced visible-light-driven photocatalytic performance. ACS Sustain. Chem. Eng. 6 (11), 15503–15516.
Watanabe, Y., 2014. Atomically precise cluster catalysis towards quantum controlled catalysts. Sci. Technol. Adv. Mater.
Wei, Z. et al, 2018. Efficient visible-light-driven selective oxygen reduction to hydrogen peroxide by oxygen-enriched graphitic carbon nitride polymers. Energy Environ. Sci. 11 (9), 2581–2589.
Weiss, E.A., 2017. Designing the surfaces of semiconductor quantum dots for colloidal photocatalysis. ACS Energy Lett. 2 (5), 1005–1013.
Wen, J. et al, 2015. Enhanced visible-light H_2 evolution of g-C_3N_4 photocatalysts via the synergetic effect of amorphous NiS and cheap metal-free carbon black nanoparticles as co-catalysts. Appl. Surf. Sci. 358, 204–212.
Wen, J. et al, 2017. Constructing multifunctional metallic Ni interface layers in the g-C_3N_4 nanosheets/amorphous NiS heterojunctions for efficient photocatalytic H_2 generation. ACS Appl. Mater. Interf. 9 (16), 14031–14042.
Weng, B. et al, 2014. One-dimensional nanostructure based materials for versatile photocatalytic applications. RSC Adv. 4 (25), 12685–12700.
White, J.L. et al, 2015. Light-driven heterogeneous reduction of carbon dioxide: photocatalysts and photoelectrodes. Chem. Rev.
Wu, H. et al, 2011. Design and fabrication of an albedo insensitive analog sun sensor. Procedia Eng. 25, 527–530.
Wu, M. et al, 2014. Synthesis of potassium-modified graphitic carbon nitride with high photocatalytic activity for hydrogen evolution. ChemSusChem 7 (9), 2654–2658.
Wu, Z. et al, 2014. Synthesis of carbon black/carbon nitride intercalation compound composite for efficient hydrogen production. Dalton Trans. 43 (31), 12013–12017.
Wu, P. et al, 2014. High alkalinity boosts visible light driven H_2 evolution activity of g-C_3N_4 in aqueous methanol. Chem. Commun. 50 (98), 15521–15524.
Wu, S. et al, 2017. Treatment of anaerobic digestate supernatant in microbial fuel cell coupled constructed wetlands: evaluation of nitrogen removal, electricity generation, and bacterial community response. Sci. Total Environ. 580, 339–346.
Xia, P. et al, 2017. Ultra-thin nanosheet assemblies of graphitic carbon nitride for enhanced photocatalytic CO_2 reduction. J. Mater. Chem. A 5 (7), 3230–3238.
Xiang, Q., Yu, J., Jaroniec, M., 2011. Preparation and enhanced visible-light photocatalytic H_2-production activity of graphene/C_3N_4 composites. J. Phys. Chem. C 115 (15), 7355–7363.
Xiao et al, 2015. Engineering heterogeneous semiconductors for solar water splitting. J. Mater. Chem. A. Mater. Energy Sustain. 3 (6), 2485–2534.
Xu, J. et al, 2013. Chemical exfoliation of graphitic carbon nitride for efficient heterogeneous photocatalysis. J. Mater. Chem. A 1 (46), 14766–14772.
Xu, L. et al, 2015. Insights into enhanced visible-light photocatalytic hydrogen evolution of g-C_3N_4 and highly reduced graphene oxide composite: the role of oxygen. Chem. Mater. 27 (5), 1612–1621.
Xu, D. et al, 2017. Bi_2O_3 cocatalyst improving photocatalytic hydrogen evolution performance of TiO_2. Appl. Surf. Sci. 400, 530–536.
Xu, Y. et al, 2019. Toward efficient preconcentrating photocatalysis: 3D g-C_3N_4 monolith with isotype heterojunctions assembled from hybrid 1D and 2D nanoblocks. ACS Appl. Mater. Interf. 11 (35), 31934–31942.
Yan, X. et al, 2017. Enhanced photocatalytic activity of Cu_2O/g-C_3N_4 heterojunction coupled with reduced graphene oxide three-dimensional aerogel photocatalysis. Mater. Res. Bull. 96, 18–27.
Yan, S., Li, Z., Zou, Z., 2010. Photodegradation of rhodamine B and methyl orange over boron-doped g-C_3N_4 under visible light irradiation. Langmuir 26 (6), 3894–3901.
Yan, W., Yan, L., Jing, C., 2018. Impact of doped metals on urea-derived g-C_3N_4 for photocatalytic degradation of antibiotics: structure, photoactivity and degradation mechanisms. Environ. Appl. Catal. B.
Yang, S. et al, 2013. Exfoliated graphitic carbon nitride nanosheets as efficient catalysts for hydrogen evolution under visible light. Adv. Mater. 25 (17), 2452–2456.
Yang, P. et al, 2017. A facile steam reforming strategy to delaminate layered carbon nitride semiconductors for photoredox catalysis. Angew. Chem. Int. Ed. 56 (14), 3992–3996.
Yang, H. et al, 2019. Constructing highly dispersed 0D Co_3S_4 quantum dots/2D g-C_3N_4 nanosheets nanocomposites for excellent photocatalytic performance. Sci. Bullet. 64 (20), 1510–1517.
Yang, Y. et al, 2019. In-situ growth of Zn–$AgIn_5S_8$ quantum dots on g-C_3N_4 towards 0D/2D heterostructured photocatalysts with enhanced hydrogen production. Int. J. Hydrogen Energy 44 (30), 15882–15891.
Yang, J. et al, 2019. One-step low-temperature synthesis of 0D CeO2 quantum dots/2D BiOX (X = Cl, Br) nanoplates heterojunctions for highly boosting photo-oxidation and reduction ability. Appl. Catal. B 250, 17–30.
Ye, S. et al, 2015. A review on g-C_3N_4 for photocatalytic water splitting and CO_2 reduction. Appl. Surf. Sci. 358, 15–27.
Ye, L. et al, 2016. Phosphorylation of g-C_3N_4 for enhanced photocatalytic CO_2 reduction. Chem. Eng. J. 304, 376–383.
Ye, R. et al, 2016. Fabrication of $CoTiO_3$/g-C_3N_4 hybrid photocatalysts with enhanced H2 evolution: Z-scheme photocatalytic mechanism insight. ACS Appl. Mater. Interf. 8 (22), 13879–13889.
Yi, M. et al, 2014. Titanium dioxide-based nanomaterials for photocatalytic fuel generations. Chem. Rev. 114 (19), 9987–10043.
You, R. et al, 2017. Graphitic carbon nitride with S and O codoping for enhanced visible light photocatalytic performance. RSC Adv. 7 (26), 15842–15850.
Yu, J. et al, 2014. Photocatalytic reduction of CO_2 into hydrocarbon solar fuels over g-C_3N_4–Pt nanocomposite photocatalysts. PCCP 16 (23), 11492–11501.
Yu, J. et al, 2014. Photocatalytic reduction of CO2 into hydrocarbon solar fuels over g-C3N4-Pt nanocomposite photocatalysts. PCCP 16 (23), 11492–11501.
Yu, X. et al, 2017. Ternary-component reduced graphene oxide aerogel constructed by g-C_3N_4/BiOBr heterojunction and graphene oxide with enhanced photocatalytic performance. J. Alloys Compd. 729, 162–170.
Yu, W. et al, 2017. Direct Z-scheme g-C_3N_4/WO_3 photocatalyst with atomically defined junction for H_2 production. Appl. Catal. B 219, 693–704.
Yu, H. et al, 2020. Enhanced photocatalytic degradation of tetracycline under visible light by using a ternary photocatalyst of Ag_3-

PO_4/AgBr/g-C_3N_4 with dual Z-scheme heterojunction. Sep. Purif. Technol. 237, 116365.
Yu, W., Xu, D., Peng, T., 2015. Enhanced photocatalytic activity of g-C_3N_4 for selective CO_2 reduction to CH_3OH via facile coupling of ZnO: a direct Z-scheme mechanism. J. Mater. Chem. A 3 (39), 19936–19947.
Yu, H., Zhu, Y., Wu, N., 2004. Synthesis of nanosized $NaTaO_3$ in low temperature and its photocatalytic performance. J. Solid State Chem. 177 (11), 3868–3872.
Yuan, Y.-P. et al, 2013. Large impact of heating time on physical properties and photocatalytic H_2 production of g-C_3N_4 nanosheets synthesized through urea polymerization in Ar atmosphere. Int. J. Hydrogen Energy 38 (30), 13159–13163.
Yuan, B. et al, 2014. Water-soluble ribbon-like graphitic carbon nitride (g-C_3N_4): green synthesis, self-assembly and unique optical properties. J. Mater. Chem. C 2 (39), 8212–8215.
Yuan, J. et al, 2015. Enhanced photocatalytic H_2 evolution over noble-metal-free NiS cocatalyst modified CdS nanorods/g-C_3N_4 heterojunctions. J. Mater. Chem. A 3 (35), 18244–18255.
Yuan, J., et al., 2014. Novel 3-D nanoporous graphitic-C_3N_4 nanosheets with heterostructured modification for efficient visible-light photocatalytic hydrogen production.
Yuejie et al, 2019. Enhanced photodegradation of toxic organic pollutants using dual-oxygen-doped porous g-C3N4: Mechanism exploration from both experimental and DFT studies. Appl. Catal. B: Environ. 248, 1–10.
Yw, A. et al, 2020. Synthesis of nitrogen vacancies g-C3N4 with increased crystallinity under the controlling of oxalyl dihydrazide: visible-light-driven photocatalytic activity – ScienceDirect. Appl. Surf. Sci. 505.
Zeng, Z. et al, 2014. Fabrication of carbon nitride nanotubes by a simple water-induced morphological transformation process and their efficient visible-light photocatalytic activity. RSC Adv. 4 (103), 59513–59518.
Zeng, D. et al, 2017. $Ni_{12}P_5$ nanoparticles embedded into porous g-C_3N_4 nanosheets as a noble-metal-free hetero-structure photocatalyst for efficient H $_2$ production under visible light. J. Mater. Chem. A 5 (31), 16171–16178.
Zeng, Y. et al, 2018. Scalable one-step production of porous oxygen-doped g-C_3N_4 nanorods with effective electron separation for excellent visible-light photocatalytic activity. Appl. Catal. B 224, 1–9.
Zhang, Z. et al, 2001. High-pressure bulk synthesis of crystalline $C_6N_9H_3\odot$ HCl: a novel C_3N_4 graphitic derivative. J. Am. Chem. Soc. 123 (32), 7788–7796.
Zhang, J. et al, 2012. Co-monomer control of carbon nitride semiconductors to optimize hydrogen evolution with visible light. Angew. Chem. Int. Ed. 51 (13), 3183–3187.
Zhang, J. et al, 2013. Efficient visible-light photocatalytic hydrogen evolution and enhanced photostability of core/shell CdS/g-C_3N_4 nanowires. ACS Appl. Mater. Interf. 5 (20), 10317–10324.
Zhang, X. et al, 2013. Enhanced photoresponsive ultrathin graphitic-phase C_3N_4 nanosheets for bioimaging. J. Am. Chem. Soc. 135 (1), 18–21.
Zhang, Y. et al, 2013. Biopolymer-activated graphitic carbon nitride towards a sustainable photocathode material. Sci. Rep. 3 (1), 1–5.
Zhang, Y. et al, 2013. Synthesis and luminescence mechanism of multicolor-emitting g-C_3N_4 nanopowders by low temperature thermal condensation of melamine. Sci. Rep. 3 (1), 1943.
Zhang, J. et al, 2014. Nanospherical carbon nitride frameworks with sharp edges accelerating charge collection and separation at a soft photocatalytic interface. Adv. Mater. 26 (24), 4121–4126.
Zhang, Y. et al, 2015. A polymer–metal–polymer–metal heterostructure for enhanced photocatalytic hydrogen production. J. Mater. Chem. A 3 (1), 109–115.
Zhang, X. et al, 2016. Photocatalytic CO_2 reduction over B4C/C_3N_4 with internal electric field under visible light irradiation. J. Colloid Interface Sci. 464, 89–95.
Zhang, Y. et al, 2016. Reversible assembly of graphitic carbon nitride 3D network for highly selective dyes absorption and regeneration. ACS Nano 10 (9), 9036–9043.
Zhang, M. et al, 2016. Photodegradation of phenol via C3N4-agar hybrid hydrogel 3D photocatalysts with free separation. Appl. Catal. B 183, 263–268.
Zhang, M. et al, 2016. Separation free g-C_3N_4/SiO_2 hybrid hydrogels as high active photocatalysts for TOC removal. Appl. Catal. B 194, 105–110.
Zhang, Q. et al, 2017. High-efficiency broadband C_3N_4 photocatalysts: synergistic effects from upconversion and plasmons. ACS Catal. 7 (9), 6225–6234.
Zhang, S. et al, 2018. Individual high-quality N-doped carbon nanotubes embedded with nonprecious metal nanoparticles toward electrochemical reaction. ACS Appl. Mater. Interf. 10 (46), 39757–39767.
Zhang, Y. et al, 2021. Research progress on g–C_3N_4–based photocatalysts for organic pollutants degradation in wastewater: from exciton and carrier perspectives. Ceram. Int. 47 (22), 31005–31030.
Zhang, J., Chen, Y., Wang, X., 2015. Two-dimensional covalent carbon nitride nanosheets: synthesis, functionalization, and applications. Energy Environ. Sci. 8 (11), 3092–3108.
Zhang, G., Li, G., Wang, X., 2015. Surface modification of carbon nitride polymers by core–shell nickel/nickel oxide cocatalysts for hydrogen evolution photocatalysis. ChemCatChem 7 (18), 2864–2870.
Zhao, H. et al, 2014. Fabrication of atomic single layer g-C_3N_4 and its high performance of photocatalytic disinfection under visible light irradiation. Appl. Catal. B 152–153, 46–50.
Zhao, H. et al, 2015. In situ light-assisted preparation of MoS_2 on g-C_3N_4 nanosheets for enhanced photocatalytic H_2 production from water. J. Mater. Chem. A 3 (14), 7375–7381.
Zhao, H. et al, 2017. Noble-metal-free iron phosphide cocatalyst loaded graphitic carbon nitride as an efficient and robust photocatalyst for hydrogen evolution under visible light irradiation. ACS Sustain. Chem. Eng. 5 (9), 8053–8060.
Zhao, G. et al, 2017. Co-porphyrin/carbon nitride hybrids for improved photocatalytic CO_2 reduction under visible light. Appl. Catal. B 200, 141–149.
Zhao, C. et al, 2018. Nitrogen defects-rich 0D/2D α-Fe_2O_3/g-C_3N_4 Z-scheme photocatalyst for enhanced photooxidation and H2 evolution efficiencies. Nano brief reports and reviews. Nano 13 (7).
Zheng, Y. et al, 2012. Graphitic carbon nitride materials: controllable synthesis and applications in fuel cells and photocatalysis. Energy Environ. Sci. 5 (5), 6717–6731.
Zheng, D. et al, 2015. Shell-engineering of hollow g-C_3N_4 nanospheres via copolymerization for photocatalytic hydrogen evolution. Chem. Commun. 51 (47), 9706–9709.
Zheng, D. et al, 2016. Layering MoS_2 on soft hollow g-C_3N_4 nanostructures for photocatalytic hydrogen evolution. Appl. Catal. A 521, 2–8.
Zhou, S. et al, 2014. Facile in situ synthesis of graphitic carbon nitride (g-C_3N_4)-N-TiO_2 heterojunction as an efficient photocatalyst for the selective photoreduction of CO_2 to CO. Appl. Catal. B 158, 20–29.
Zhou, Y. et al, 2015. Brand new P-doped g-C_3N_4: enhanced photocatalytic activity for H2 evolution and Rhodamine B degradation under visible light. J. Mater. Chem. A 3 (7), 3862–3867.
Zhou, M. et al, 2017. n/n junctioned g-C_3N_4 for enhanced photocatalytic H 2 generation. Sustain. Energy Fuels 1 (2), 317–323.
Zhou, M. et al, 2018. Boron carbon nitride semiconductors decorated with CdS nanoparticles for photocatalytic reduction of CO_2. ACS Catal. 8 (6), 4928–4936.
Zhou, W. et al, 2020. Metal-free hydrophilic DA conjugated polyelectrolyte dots/g-C_3N_4 nanosheets heterojunction for efficient and irradiation-stable water-splitting photocatalysis. Appl. Catal. B 270, 118852.

Zhou, Z. et al, 2020. Nitrogen vacancy mediated exciton dissociation in carbon nitride nanosheets: Enhanced hydroxyl radicals generation for efficient photocatalytic degradation of organic pollutants. J. Hazard. Mater. 387, p. 122023-.

Zhu, J. et al, 2014. Graphitic carbon nitride: synthesis, properties, and applications in catalysis. ACS Appl. Mater. Interf. 6 (19), 16449–16465.

Zhu, Y.-P., Ren, T.-Z., Yuan, Z.-Y., 2015. Mesoporous phosphorus-doped g-C_3N_4 nanostructured flowers with superior photocatalytic hydrogen evolution performance. ACS Appl. Mater. Interf. 7 (30), 16850–16856.

Zou, Z. et al, 2001. Direct splitting of water under visible light irradiation with an oxide semiconductor photocatalyst. Nature 414 (6864), 625–627.

Zubair, M. et al, 2021. Heavy metals occurrence, seasonal variation and enrichment in urban soils augmented with industrial waste. Polish J. Environ. Stud. 30 (5), 4871–4886.